ABSTRACT

Title of Dissertation: THE EFFECTS OF SURFACE GRAVITY WAVES ON AIR-SEA MOMENTUM TRANSFER AND VERTICAL MIXING IN A FETCH-LIMITED, ESTUARINE ENVIRONMENT

Alexander William Fisher, Doctor of Philosophy, 2017

Dissertation directed by: Lawrence P. Sanford, Professor
Marine, Estuarine, and Environmental Science

Surface gravity waves are the principal pathway through which momentum and energy are transferred from the atmosphere to the ocean. Recent studies have contributed to a growing recognition that wind events can be of leading-order importance for mixing and circulation in estuaries, yet the specific nature of air-sea momentum transfer in coastal environments remains relatively understudied. As part of a collaborative investigation of wind-driven estuarine physics, this dissertation addresses the role that surface gravity waves play in the transfer of momentum from the air to the oceanic surface boundary layer in a fetch-limited, estuarine environment. Using a combination of direct field observations and numerical simulations, the role of surface gravity waves in structuring momentum transfer and vertical mixing were examined for a range of wind, wave, and stratification conditions. Results indicate that inclusion of surface gravity waves in bulk parameterizations of wind stress reduced bias to below 5% for nearly all observed wind speeds and that up to 20% of wind stress variability within Chesapeake Bay was directly attributable to surface wave variability. Furthermore, the 10-meter neutral drag coefficient was shown to vary spatially by more than a factor of two over the extent of Chesapeake Bay as a result of combined wind and wave variability. Anisotropic fetch-limitation resulted in dominant wind-waves that were commonly and persistently misaligned with local wind forcing. Direct observations of stress above and below the water surface demonstrated that, within the oceanic surface layer, stress was more aligned with wave forcing than wind forcing. Accounting for the surface wave field was needed to close the local momentum budget between the atmosphere and the mean flow. Directly observed turbulent profiles showed that breaking waves dominated the transfer of momentum and energy and resulted in a three-layer turbulent response consisting of a wave transport layer, surface log layer, and stratified bottom boundary layer. Comparisons to commonly employed second-moment turbulence closures suggest that the presence of breaking waves homogenized the surface layer to a greater extent than predicted by present parameterizations of turbulent kinetic energy transport away from a source at the surface.

THE EFFECTS OF SURFACE GRAVITY WAVES ON AIR-SEA MOMENTUM TRANSFER AND VERTICAL MIXING IN A FETCH-LIMITED, ESTUARINE ENVIRONMENT

by

ALEXANDER WILLIAM FISHER

Dissertation submitted to the Faculty of the Graduate School of the
University of Maryland, College Park in partial fulfillment
of the requirements for the degree of
Doctorate of Philosophy
2017

ADVISORY COMMITTEE:

PROFESSOR LAWRENCE P. SANFORD, CHAIR
University of Maryland Center for Environmental Science

PROFESSOR WILLIAM C. BOICOURT
University of Maryland Center for Environmental Science

ASSOCIATE PROFESSOR KAYO IDE
University of Maryland, College Park

PROFESSOR MING LI
University of Maryland Center for Environmental Science

ASSISTANT PROFESSOR NICHOLAS J. NIDZIEKO
University of California, Santa Barbara

ASSOCIATE SCIENTIST MALCOLM E. SCULLY
Woods Hole Oceanographic Institution

For my parents and Michelle,
thank you for all of your love and support.

ACKNOWLEDGEMENTS

I doubt that I will ever be able to repay my advisor, Larry Sanford, for his guidance and support throughout my time at Horn Point Laboratory. Every idea and interest was met with encouragement and thoughtful discussion, giving me the confidence and drive to delve deeper into the subject matter and explore new directions. From examining the finer points of mud while at North Bay to watching for windrows on the water surface, Larry was always a source of new interest and renewed passion in coastal physics. In addition to work aboard the R/V Sharp, I am thankful to have been part of many other field projects with Larry including snorkeling on a SAV bed in the Susquehanna flats and cruises aboard the R/V Rachel Carson.

Similarly, I have had the good fortune to have a committee that included Bill Boicourt, Ming Li, Malcolm Scully, Nick Nidzieko, and Kayo Ide. Each encouraged me to pursue my research with care and enthusiasm, while sharing a wealth of knowledge and experience to help make it happen. I'd like to thank Malcolm for introducing me to the fascinating (and sometimes frustrating) world of estuarine turbulence: it became a cornerstone of my dissertation and a topic I now hold in esteem. My conversations with Ming and Bill were always a source of inspiration, often illuminating the nuanced nature of estuarine physics and deepening my appreciation of these amazing ecosystems. Kayo Ide offered guidance and encouragement in learning new modeling techniques, including the opportunity to enroll in a data assimilation program at College Park. I'd also like to acknowledge Evamaria Koch, who sat on my comprehensive exams committee – Eva's near-constant smile every time I saw her was always warmly appreciated.

I'd like to thank Nick Nidzieko for encouraging me to think outside of the box. Nick was always available and excited to discuss any of my science questions, offering advice on topics spanning experimental design to career guidance. From developing a course for stratified turbulence to chasing schools of Menhaden with a REMUS, Nick was a constant supporter of my ideas and willing participant in developing them further.

Steve Suttles was my oceanographic instrumentation and field deployment guru, teaching me the value of Super 33+ vinyl tape and the importance of wiring schematics. I owe Steve a huge debt of gratitude for sharing his experience and knowledge with me over the many days we spent in the Physical Oceanography lab and in the field. I am also indebted to Carole Derry for all of her help during field deployments and data processing.

The VIMS team of Carl Friedrichs, Grace Cartwright, and Kelsey Fall were all valued collaborators and field crewmates. I also owe a big "thank you" to the captain and crew of the R/V Sharp for their assistance in field data collection.

Before I arrived at HPL, there were several people that helped guide me along my path to becoming a coastal physical oceanographer. Faculty and students of the EFML at Stanford University and faculty within the CEE department at the University of Washington were the first ones who introduced me to coastal oceanography and inspired me to make it my career.

Finally, I'd like to thank the students, faculty, and staff of Horn Point Laboratory. During the four-plus years I've spent at HPL, I've gained many friends and colleagues who truly made the graduate experience one I'll always remember.

TABLE OF CONTENTS

LIST OF TABLES

Chapter 2

LIST OF FIGURES

Chapter 2

Chapter 3

Chapter 4

Appendix A

CHAPTER 1

INTRODUCTION

Waves are a ubiquitous feature of wind blowing over a water surface and provide a dynamic link between the atmosphere and the world's oceans. Because the surface wave field is the primary pathway though which momentum and energy are transferred between the atmosphere and the sea, surface waves play a pivotal role in the structuring the response of an ocean to wind blowing over its surface. In the shallow coastal ocean, increased complexity of wind-wave interactions and wind-forced coastal hydrodynamics stems from the presence of energetic tidal currents, bottom friction, strong density stratification setup by riverine freshwater input, and the proximity to shore.

This dissertation aims to address the role that surface gravity waves play in the transfer of momentum from the air to the oceanic surface layer in a fetch-limited, partially stratified estuary.

§1.1 Research Overview

Chesapeake Bay is the nation's largest estuary, spanning over 300km from its head to the Atlantic Ocean, and, like many coastal plain estuaries, formed when sea level rise drowned the alluvial valley of the Susquehanna River 10,000 years ago. The Bay has an average depth of 7m with a bathymetry characterized by broad shallow shoals flanking a deep central channel. Overfishing and anthropogenic nutrient pollution has resulted in significant ecosystem degradation, which has prompted a multi-billion dollar effort to improve Bay water quality (USEPA 2010). Perhaps most significantly, the central channel of Chesapeake Bay experiences chronic summertime hypoxia that extends

throughout most of the main-stem Bay during summer months (Hagy et al 2004, Kemp et al 2005, Murphy et al 2011, Zhou et al 2014).

In light of recent work that has shown that wind can exert leading order control of material exchange in estuaries (Chen & Sanford 2009, Chen et al 2009, Scully 2010a, Scully 2010b, Scully 2013), this study was undertaken to investigate the dynamics of air-sea momentum transfer in an estuarine environment. Using a combination of direct observations and numerical simulations, the interaction between the atmosphere, surface wave field, and the mean flow was examined. The dissertation is organized into five chapters as follows:

INTRODUCTION

In Chapter 1 (this chapter), an introduction to the project and motivation for this research is presented in the context of wind-driven estuarine flows.

WIND STRESS DYNAMICS IN CHESAPEAKE BAY

In Chapter 2, wind and wave effects on wind stress development at the water surface are examined through direct observation and simulations from a third generation numerical wave model, Simulating Waves Nearshore (SWAN). Results are presented that demonstrate the significant influence of fetch-limited wave growth on wind stress developed under variable wind forcing.

Surface Wave Effects on the Translation of Wind Stress Across the Air-Sea Interface

In Chapter 3, the role of surface gravity waves in the local air-sea momentum budget is quantified using cospectral stress estimates, collected above and below the air-sea interface, and numerical modeling results. Fetch-limited wave growth results in a surface wave field that is commonly and persistently misaligned with wind forcing creating a capacity for significant momentum storage within the surface wave field.

Wind-Wave Effects on Estuarine Turbulence

In Chapter 4, direct observations of turbulent quantities beneath breaking waves are compared to second moment turbulence closure predictions often employed in coastal circulation models. Results indicate that stability functions often used in closure schemes result in a dramatic underprediction of the turbulent eddy viscosity within the wave-affected surface layer, suggesting that a combination of wave breaking and coherent wave-driven vortices homogenize the surface mixed layer beyond that expected for free shear turbulence.

Conclusions

In the final chapter, the results of chapters 2-4 are synthesized and directions for future research are discussed.

§1.2 Motivation

Estuaries are complex systems in which buoyancy alters the density field of an embayment relative to that of the adjoining coastal ocean. The subtidal circulation within estuaries is dominated by the horizontal density gradient induced by buoyant forcing (e.g. riverine freshwater input), resulting in a complex exchange circulation comprised of a two-layered flow in which a seaward-flowing surface layer is balanced by a landward flowing bottom layer. This is known as the exchange flow, gravitational circulation, or estuarine circulation.

Despite typically being an order of magnitude weaker than the tidal flow, the exchange flow is volumetrically much larger than the river flow and of disproportionate importance for exchange within the estuary. The bidirectional nature of estuarine circulation enhances the longitudinal dispersion of passive scalars, an important phenomenon when considering residence time and how it relates to ecosystem function. The exchange flow can trap sinking particles, such as sediments and particulate organic matter and is a significant contributor to the high sediment accumulation rates (Traykovski et al 2004), high nutrient recycling rates, and frequent hypoxia (Kemp et al 2005, Murphy et al 2011) typically observed in estuaries.

1.2.1 Spatiotemporal Variability of Atmospheric Fluxes

Before proceeding to a discussion of wind-driven estuarine responses, it is important to highlight the manner in which most of these analyses have accounted for atmospheric forcing. While the spatiotemporal variability of surface fluxes has received

considerable attention at the global ocean scale, it has represented a significantly smaller portion of estuarine and coastal literature where other processes (e.g. tides) are often assumed to dominate vertical flux profiles.

Despite recognition that processes like sea breezes, topographical steering, and shadow zones (Markfort et al 2010) may result in significant fine scale structure in a coastal wind field, a common practice has been to model wind stress as a simplified field derived from a limited number of stations (often one). It is expected that winds over water may be significantly stronger than winds over land due to reduced surface roughness – as such, empirical conversions are often used to adjust overland wind observations to expected over-water conditions in order to match model predictions to observations (Li et al 2005).

Furthermore, wind-driven flow in estuaries has been predominantly described through analyses of along-channel wind forcing (Geyer 1997, Scully et al 2005, Chen & Sanford 2009, Li & Li 2011). Although recent studies have suggested that wind direction may have important implications for scalar exchange within an estuary at synoptic and seasonal timescales (Scully 2010a, Scully 2010b), the response of an estuary to directionally variable wind forcing has received far less attention than axial forcing. The sensitivity of wind-driven responses to variable surface atmospheric fields has not been adequately explored and represents a significant gap in our understanding of wind-driven coastal flows.

1.2.2 The Estuarine Response to Wind Forcing

Wind can drive an exchange flow that may dominate circulation in estuaries at weather-band frequencies, but recent literature has suggested that winds can be of first order importance in regulating estuarine circulation in shallow estuaries through modifications to the estuarine density field and vertical mixing.

The primary response of an estuary to along-channel wind forcing is two-layered: the wind stress drives the surface layer in the direction of the wind, which sets up a barotropic pressure gradient in the opposite direction that drives a bottom return flow. In larger estuaries, like Chesapeake Bay, the barotropic response is typically expressed as a quarter-wave seiche (Wang 1979, Chuang & Boicourt 1989). The nature of this response is generally well-understood, but its dependence on estuarine geometry and temporal evolution are less clear.

In their classical derivation of estuarine circulation, Hansen and Rattray (1965) accounted for the influence of along-channel wind stress on the gravitational circulation within an idealized estuary. While limited by number of assumptions (e.g. MacCready & Geyer 2014), the classical analysis provides a qualitative starting point in the discussion of the wind-forced axial estuarine response. In the up-estuary case, an axial wind stress acts in opposition to gravitational circulation and reduces the along channel salinity gradient thereby reducing or even reversing the exchange flow (Geyer 1997). In contrast, a down-estuary wind acts in concert with gravitational circulation and can enhance the exchange flow.

This classical approach, however, does not account for the changes in vertical mixing due to the advection of salt by wind-forced vertical shear (isopycnal straining),

which has been shown to be of leading order consequence in determining the strength of the estuarine exchange flow (Scully et al 2005, Chen & Sanford 2009, Li & Li et al 2011a, Burchard & Hetland 2011). While direct shear mixing works to erode density stratification regardless of wind direction, isopycnal straining can either enhance or suppress vertical mixing. During up-estuary winds, isopycnals are tilted towards vertical, reducing the exchange flow and increasing the effective eddy viscosity (Scully et al 2005, Chen & Sanford 2009, Scully 2010b, Li & Li 2011a, Burchard and Hetland 2011). In contrast, down-estuary winds tilt isopycnals towards horizontal, which decreases the eddy viscosity and increases the exchange flow.

The competing effects of isopycnal straining and direct wind mixing can be expressed as a function of the Wedderburn number (Monismith 1986), which is a measure of the relative influence of wind-driven and buoyancy-driven circulations on estuarine residual flows (Monismith 1986, Geyer 1997, Chen & Sanford 2009). During up-estuary winds, direct wind mixing and iopycnal straining both act to reduce vertical density stratification. However, the competing effects of direct mixing and straining result in a threshold behavior during down-estuary winds. Under low to moderate wind speeds, straining dominates and results in an intensification of gravitational circulation, but the shear-driven mixing under high winds is energetic enough to overwhelm the straining-induced stratification (Chen & Sanford 2009). Additionally, the recovery of an estuarine salt field to steady state conditions is heavily influenced by wind direction, with stratification recovery following up-estuary winds taking much longer than that following a down-estuary wind (Li and Li 2011a).

Lateral (cross-channel) advection of along-channel momentum can be of first-order importance to the subtidal along-channel momentum balance and a significant contributor to residual estuarine circulation (Lerzcak & Geyer 2004, Huijts et al 2008, Scully et al 2009). Lateral variations in wind-driven axial flows are primarily the result of the depth-dependence in the along-channel momentum balance between pressure gradients, friction, and wind stress in lakes (Csanady 1972) and wide estuaries (Friedrichs & Hamrick 1996). In an idealized estuary which has a triangular channel cross section, the wind-driven circulation is generally characterized by downwind flow over the shoals and an upwind flow over the channel with maximum velocity in the lower half of the water column (Csanady 1972, Sanay & Valle-Levinson 2005).

Wind-driven lateral circulation in estuaries is a function of wind speed, direction, bathymetry, shear in the along-channel velocity, and vertical and lateral density stratification. In addition to the coastal upwelling/downwelling response, other modes of lateral circulation have been observed in the estuarine environment including lateral internal seiching (Sanford et al 1990). In estuaries where the effects of the Earth's rotation can be considered negligible, the steady state balance reduces to a lateral pressure gradient force opposing a vertical stress divergence – implying that lateral flows are generated mainly by lateral baroclinicity.

Examining the lateral salinity balance under these conditions, it becomes clear that lateral circulation induced by along-channel wind forcing is primarily-driven by the differential advection of the axial salinity gradient by laterally-sheared axial flow (Nunes & Simpson 1985, Chen & Sanford 2008). It should be noted that the temporal evolution of wind-driven lateral flows can be complex resulting from the fact that lateral circulation

is driven not only by wind-forcing, but also by the lateral density gradient and vertical stratification. While wind-forcing may dominate during the first half of a wind event, baroclinicity and vertical stratification may exert greater influence during the relaxation of a wind event (Li & Li 2011).

For estuaries whose width exceeds their internal Rossby radius, Ekman flows become a dominant factor in driving lateral flows. While it is difficult to generalize the strength of estuarine circulation based on estuary width due to complex dependencies on vertical mixing rates and lateral structure (Valle-Levinson 2008), a few generalizations can be made. In shallow estuaries, the Ekman response is dependent on vertical stratification. As the estuary becomes well-mixed and the surface and bottom Ekman layers merge, the rotational effect diminishes and the boundary layer aligns with the wind forcing (Chen & Sanford 2009). Therefore, the differences between rotational and nonrotational lateral circulation regimes decrease as vertical stratification decreases (Chen & Sanford 2008, Li and Li 2011b). Furthermore, Chen & Sanford (2008) suggest that wind-driven and tidal lateral flows are largely additive – larger lateral salinity gradients occur when tides and winds act in concert.

Recent studies have shown that lateral flows can have a profound effect on the subtidal residual circulation in estuaries (Scully et al 2009) and sediment transport patterns (Chen et al 2009). Additionally, Scully (2010b) determined that lateral flows may play a key role in the vertical exchange of oxygen through the advection of oxygen-rich waters from shallow-shoals to below the pycnocline – ventilating the hypoxic waters deep in a central channel at times more effectively than direct vertical mixing. The

efficiency of wind-driven lateral flows in regulating oxygen exchange within an estuary is highly dependent on wind direction and bathymetry (Scully 2010b).

1.2.3 Energy And Momentum Transfer Through The Surface Wave Field

The transfer of momentum and mechanical energy from the atmospheric boundary layer to the oceanic surface boundary layer takes place primarily through the surface wave field (Melville et al 1996). Wind stress develops at the water surface as a result of frictional resistance and form drag due to the presence of surface gravity waves. This wave-enhancement of atmospheric surface boundary turbulence is often parameterized in bulk formulations of wind stress using empirical, wave-dependent roughness parameters that relate wave growth to turbulent boundary layer dynamics (Donelan 1990, Smith et al. 1992, Johnson and Vested 1992, Dobson et al 1994, Martin 1998, Johnson et al. 1998, Oost et al. 2002, Edson et al 2013). As wave energy dissipates, principally through wave breaking, energy imparted to the surface wave field by wind forcing is transferred to the mean flow of the underlying water column.

As wind seas develop, nonlinear wave-wave interactions transfer energy from short waves to long waves. Although hypothesized that a wind sea will eventually come into equilibrium with wind forcing (Pierson & Moskowitz 1964), such that wave energy dissipation balances wind input, field observations have shown that nonlinear interactions continue to transfer energy to lower frequencies resulting in wind seas that never fully develop (Hasselmann et al 1973, Komen et al 1994). However, an equilibrium subrange (Phillips 1985) is expected within the high frequency portion of wave power spectra where short gravity waves support the majority of the atmospheric wind stress (Janssen

1989). It is often common practice to assume that the surface wave field is in structural equilibrium with wind forcing in coastal circulation modeling.

In fetch-limited environments, wave energy and peak frequency are directly related to the distance over which wind blows (Hasselmann et al 1973, Komen et al 1994, Babanin & Soloviev 1998, Badulin et al 2007). Fetch-limitation represents an important caveat of wind-forced coastal dynamics due to a capacity for transient wind energy input and an upper bound on wave growth that can result in enhanced wave nonlinearity relative to open ocean conditions. This, in turn, alters wind stress development at the water surface (Mahrt et al 1996, Vickers & Mahrt 1997) and wave breaking dynamics (e.g. Rapp & Melville 1990), which transfer momentum and energy from the air to the sea.

1.2.4 Waves and the Oceanic Surface Boundary Layer

Because direct observations of turbulent fluxes requires cospectral estimates of velocity and scalars, observational constraints have restricted direct measurement of the vertical fluxes of momentum and energy beneath breaking waves. Estimates of the dissipation of turbulent kinetic energy beneath breaking waves have shown that within the wave-transport layer dissipation rates are balanced by a divergence of turbulent kinetic energy transport and are orders of magnitude larger than that expected near a rigid boundary (Kitaigorodskii et al 1983, Agrawal et al 1992, Anis & Moum 1995, Terray et al 1996, Drennan et al 1996, Soloviev et al 2005, Fedderson et al 2007, Jones & Monismith 2008a, Gerbi et al 2009, Gemmrich 2010). In an analysis of the same dataset presented in this dissertation, Scully et al (2016) found that plunging deep-water breaking

waves dominated the transfer of energy and momentum in the surface layer of Chesapeake Bay.

Wave breaking also provides a seed of vertical vorticity that can lead to the generation of coherent turbulent structures beneath breaking waves through vortex straining (Craik & Leibovich 1976, Leibovich 1983, Sullivan et al 2007). In 1938, Irving Langmuir noticed windrows of Sargassum and sought to explain the physical mechanisms responsible for the phenomenon – leading to the first description of Langmuir circulation (Langmuir 1938). It has since been established that vertical shear in the Lagrangain velocity can modify a turbulent surface boundary layer to produce coherent cells, which form and dissipate episodically resulting in "Langmuir turbulence" (McWilliams et al 1997).

Turbulent transport within the oceanic surface boundary layer is often enhanced by the presence of Langmuir turbulence due to the large vertical velocities and length-scales of Langmuir cells (Li et al 2005, Grant & Belcher 2009, Harcourt & D'Asaro 2008, Kukulka et al 2009). Variable wind and wave conditions (Churchill et al 2006), depth-effects (Gargett et al 2004), and strong tidal currents (Kukulka et al 2012) complicate the dynamics of Langmuir turbulence in coastal environments compared to the open ocean.

Observations of Langmuir cells are challenging due to the episodic nature of cells and the coupling between wave breaking and Langmuir turbulence. While Langmuir turbulence has been documented in the coastal ocean (Gargett et al 2004, Gerbi et al 2009, Scully et al 2015), field characterizations of Langmuir turbulence remain sparse in coastal literature. During one of the field deployments analyzed in this dissertation,

observations of coherent cells consistent with Langmuir turbulence were documented in the middle reaches of Chesapeake Bay (Scully et al 2015).

1.2.5 Motivating Conclusions

The preceding literature review provides an overview of research on the estuarine response to wind forcing including modifications to the residual gravitational circulation, development of axial and lateral flows, the transfer of momentum from air to sea, and vertical mixing within an estuary. Winds have been shown to be of first order importance in modulating circulation and oxygen exchange in estuaries, such that deepening our understanding of how these flows evolve and their dependence on variable air-sea processes may have important implications for long-term prediction and management strategies.

While recognized as a simplification of atmospheric conditions, a common practice in the coastal community has been to apply a uniform surface stress to assess the impact of wind forcing on estuarine dynamics. The spatiotemporal variability of directional air-sea fluxes in a coastal, fetch-limited environment remains an open question that has important implications for many estuarine processes including the generation of waves, currents, and turbulence. There is a clear need to characterize the variability of these processes at a basin-scale and quantify its impact on momentum transfer in an estuarine system.

Traditionally, wind has been viewed as a direct driver of vertical mixing in estuaries through the development of shear. Recent work has suggested that the wind-driven response is more complex due to the straining of salinity fields and significant

lateral advection that develops under axial wind forcing. Furthermore, wind-driven turbulence may evolve in different forms: shear-layer production, wave breaking, and/or Langmuir turbulence. Wind-driven flows, which have been shown to be important regulators of scalar transport in estuaries, are dependent on the vertical profiles of eddy viscosity and density stratification suggesting that they are sensitive to the variability of near-surface processes.

The effects of surface gravity waves on vertical mixing and the circulatory response represents a significant gap in our understanding of wind-driven flows in estuaries and coastal seas. Numerical circulation models are common and robust tools used in describing the physical response of an estuary to wind forcing, yet very few numerical studies of estuarine flows have included surface gravity waves. Inclusion of wave effects in numerical circulation models requires wave-dependent parameterizations of wind stress, surface energy fluxes, and vertical mixing. A comparative analysis of observations and empirical predictions can inform the development and validation of wave-dependent parameterizations used within the framework of numerical circulation modeling.

CHAPTER 2

WIND STRESS DYNAMICS IN CHESAPEAKE BAY

Preface

This chapter is a reproduction of work published in the Journal of Physical Oceanography with coauthors Larry Sanford and Steve Suttles. The right to reuse this work was retained by the authors when publication rights and nonexclusive copyright were granted to the American Meteorological Society.

Fisher, A. W., L. P. Sanford, and S. E. Suttles, (2015): Wind stress dynamics in Chesapeake Bay: Spatiotemporal variability and wave dependence in a fetch-limited environment. J. Phys. Oceanogr., 45, 2679-2696.

§2.1 Introduction

While significant attention has been paid to tidal dynamics, recent studies have contributed to a growing recognition that wind can be of first order importance for wave generation, vertical mixing, and circulation in estuaries. Investigations of wind-driven estuarine flows (Scully et al 2005, Geyer et al 2007, Chen & Sanford 2009, Scully 2010a, Li & Li 2011, Scully 2013) have revealed that wind speed and direction often play important roles in determining how gravitational circulation is modified by wind forcing. This has prompted further investigation into the variability of wind-driven flows and their effect on oxygen exchange in chronically hypoxic systems (Scully 2010b), sediment transport (Chen et al 2009), and planktonic interactions. However, despite advances in wind-driven estuarine dynamics the spatiotemporal variability of wind stress in the coastal environment remains poorly understood.

While processes like sea breezes, topographical steering, and shadow zones (Markfort et al 2010) may result in significant fine scale structure in a coastal wind field, a common practice has been to model wind stress as a simplified field derived from a limited number of stations. It is expected that winds over water may be significantly stronger than winds over land due to reduced surface roughness – as such, empirical conversions are often used to adjust overland wind observations to expected over-water conditions in order to match model predictions to observations (Li et al 2005).

Variable wind forcing can influence the development of wind stress directly and indirectly through the generation of surface waves - suggesting that wind stress dynamics in a coastal embayment may exhibit additional variability stemming from the mutual

interdependence between air-sea fluxes and the surface wave field. As part of a collaborative investigation of wind-driven estuarine physics in Chesapeake Bay, we investigated the spatiotemporal variability of wind stress through a combination of direct observations and numerical modeling.

2.1.1 Background

Direct measurement of air-sea fluxes requires sampling of turbulent fluctuations of the wind velocity field, air temperature, sea temperature, and humidity. In the marine environment, such measurements are challenging and have resulted in records of air-sea fluxes that are sparse in both space and time. Because of this, methods have been developed which use bulk formulae to relate more easily measured averaged quantities (wind speed, temperature, and humidity) to turbulent fluxes through empirical transfer coefficients (Large & Pond 1981, Fairall et al 1996, Edson et al 2013). These bulk parameterizations rely heavily on Monin-Obukhov similarity theory (Monin & Obukhov 1954, Obukhov 1971), which states that constant flux profiles exist in a stationary, horizontally homogeneous atmospheric boundary layer such that the wind velocity profile can be expressed as:

$$\frac{U_{zN}}{u_*} = \frac{1}{\kappa}\left[\ln\left(\frac{z}{z_0}\right) - \psi\left(\frac{z}{L}\right)\right] \qquad (2.1)$$

Where U_{zN} is the neutral wind speed at z meters above sea level, u_* is the shear velocity, z_0 is the roughness height, κ is von Karman's constant (0.41), and L is the

Monin-Obukhov stability length. Equation (2.1) describes the well-known "law of the wall" scaling with the addition of a stability function $\psi\left(\frac{z}{L}\right)$ based on a normalized Monin-Obukhov stability length, which adjusts the neutral boundary layer profile for stratified conditions. The Monin-Obukhov stability length describes the theoretical height above reference level at which shear-produced turbulence is equal to the buoyant production of turbulence and can be estimated by:

$$L = \frac{\rho c_p u_*^3 \theta}{\kappa g\left(H_s - H_L/14\right)} \tag{2.2}$$

where θ is the mean potential temperature within the boundary layer, g is gravitational acceleration, c_p is the specific heat of air at constant pressure, H_S is the sensible heat flux, and H_L is the latent heat flux (Monin & Obukhov 1954). Numerous formulations of the stability function $\psi_{z/L}$ have been determined empirically (Liu et al 1979, Large & Pond 1981, Panofsky and Dutton 1984, Erickson 1993, Atakturk and Katsaros 1999). We chose to follow the COARE 3.0 formulation outlined in Fairall (2003).

The Monin-Obukhov similarity theory was developed for terrestrial atmospheric boundary layers, where roughness elements (e.g. vegetation) can be treated as slowly varying relative to atmospheric forcing. In marine environments, roughness is determined by the surface wave field, which is in turn driven by the wind. This suggests that additional parameters are likely needed to account for the effect of dynamic roughness elements present in marine environments.

The velocity field above surface gravity waves can be decomposed into a mean flow, turbulent fluctuations, and a wave-coherent component (Phillips 1977). Near the ocean surface, O(1m) for pure wind seas (Janssen 1989, Makin & Mastenbroek 1996, Drennan et al 1999), momentum exchange is largely governed by the wave-coherent velocity component in what is known as the wave boundary layer (WBL). Turbulence statistics taken above the WBL, where turbulent flow is generated by wind shear/buoyancy and suppressed by stratification, are expected to obey Monin-Obukhov similarity theory (Drennan et al 2003). Drennan et al 1999 showed that for pure wind seas, turbulent velocity spectra and co-spectra measured between 2m and 12m above MSL obeyed Monin-Obukhov similarity theory for a variety of sea states (Drennan et al 1999, Drennan et al 2003). The validity of the Monin-Obukhov theory breaks down in the presence of significant swell when wave-coherent stress dynamics become more dominant.

The bulk parameterization of wind stress is defined as follows:

$$\tau = \rho C_{zN} U_{zN}^2 \qquad (2.3)$$

where τ is wind stress, ρ is density and C_{zN} is the neutral drag coefficient defined as $C_{zN} \equiv (\frac{u_*}{U_{zN}})^2$. Typically, the reference height at which the drag coefficient and neutral velocity are evaluated is 10 meters. Similar to the surface velocity field described previously, wind stress can be partitioned into turbulent τ_t, wave-coherent τ_w, and viscous τ_v components (Phillips 1977, Drennan et al 2003).

The partitioning of wind stress into viscous and rough components utilizes the following formulation of surface roughness (Liu et al 1976, Smith et al 1988, Fairall et al 1996):

$$z_0 = z_{0\ \text{smooth}} + z_{0\ \text{rough}} \tag{2.4}$$

where $z_{0\ \text{smooth}}$ is a term used to account for surface stress supported by viscous shear during aerodynamically smooth conditions and $z_{0\ \text{rough}}$ accounts for wind-driven waves acting as roughness elements under hydraulically rough conditions. We adopt a Reynolds roughness parameterization of the smooth component of surface roughness that is typically applied in the following way:

$$z_{0\ \text{smooth}} = \gamma \frac{\nu}{u_*} \tag{2.5}$$

where γ is an empirical constant determined through laboratory experiments to be 0.11 (Edson et al 2013) and ν is the kinematic viscosity of air. In what is now the well-known Charnock's relation, Charnock (1955) used dimensional analysis to derive a parameterization of $z_{0\ \text{rough}}$ using an empirical parameter, $\propto$ (known as the Charnock parameter), and the shear velocity.

$$z_{0\ \text{rough}} = \propto \frac{u_*^2}{g} \tag{2.6}$$

Charnock took alpha to be a constant value of 0.012 (Charnock 1955), suggesting that $C_{zN} = fn(z, U_{zN})$. While numerous studies have developed bulk relations using this solely wind speed dependent formulation, there are significant differences between the proposed curves (Drennan et al 2003, Geernaert 1990, Banner et al 1999) which has prompted investigation of alpha as a wave-dependent function. It is now common to use a constant alpha (e.g. Wu 1980) value or alpha that is a function of wind speed (Fairall 2003, Edson et al 2013) to estimate wind stress from bulk measurements. It has been shown that at high wind speeds, the Charnock parameter tends to approach a constant value of ~0.028 (Edson et al 2013), as such alpha values are typically constrained to asymptote at high wind speeds but are allowed to vary linearly with wind speed at lower wind speeds.

Studies have shown that alpha is correlated with wave age, defined as the phase velocity of the waves (C_p) divided by either u_* or U_{N10} (Smith et al. 1992, Johnson and Vested 1992, Johnson et al. 1998, Oost et al. 2002, and Edson et al 2013) and with wave slope (Donelan 1990, Smith et al 1992, Dobson et al 1994, Martin 1998, Edson et al 2013). The Charnock parameter has been shown to decrease with increasing wave age (e.g. Komen et al 1998), which agrees with the notion that sea surface roughness decreases as seas mature. Fully developed seas typically occur by $C_P / u_* \sim 33$ (Donelan 1990). For fully developed seas in the open ocean, direct measurements have shown that the Charnock parameter is typically on the order of 0.011 (Smith 1980, Large & Pond 1981, Smith 1988) with significantly less scatter between datasets than for those collected in fetch-limited environments where the Charnock parameter has been measured to reach

much higher values – 0.0145 (Garratt 1977), 0.018 (Wu 1980), 0.0288 (Geernaert et al 1986).

§2.2 Observational Methods & Data Analysis

2.2.2 Study Site

Field observations were conducted in the middle reaches of Chesapeake Bay, where fetch-limited wind seas dominate (Sanford 1994; Lin et al. 1998; Lin 2000). Chesapeake Bay is a semi-enclosed coastal embayment on the mid-Atlantic coast of the United States and is the largest estuary in the USA spanning 320 km from the mouth of the Susquehanna River to the Atlantic Ocean with a width that ranges from 5km to over 20km (Figure 2.1). Swell generated in the Atlantic Ocean can result in mixed seas in the southern Bay (Boon 1998, Lin et al 2002), but swell dissipates to undetectable levels by the time it reaches the mid-Bay.

2.2.3 Bulk Atmospheric Measurements

Ten instrumented surface buoys were deployed during the spring of 2012 (March 16 to June 29, 2012) which provided bulk measurements of air temperature, wind speed and direction, relative humidity, sea surface temperature, and salinity at 30 minute resolution. Atmospheric measurements were collected at 3m above the water surface and temperature and conductivity sensors mounted 1m below the water surface provided

temperature and salinity data. The field array was composed of three lateral transects in the mid-Bay and is shown in Figure 2.1.

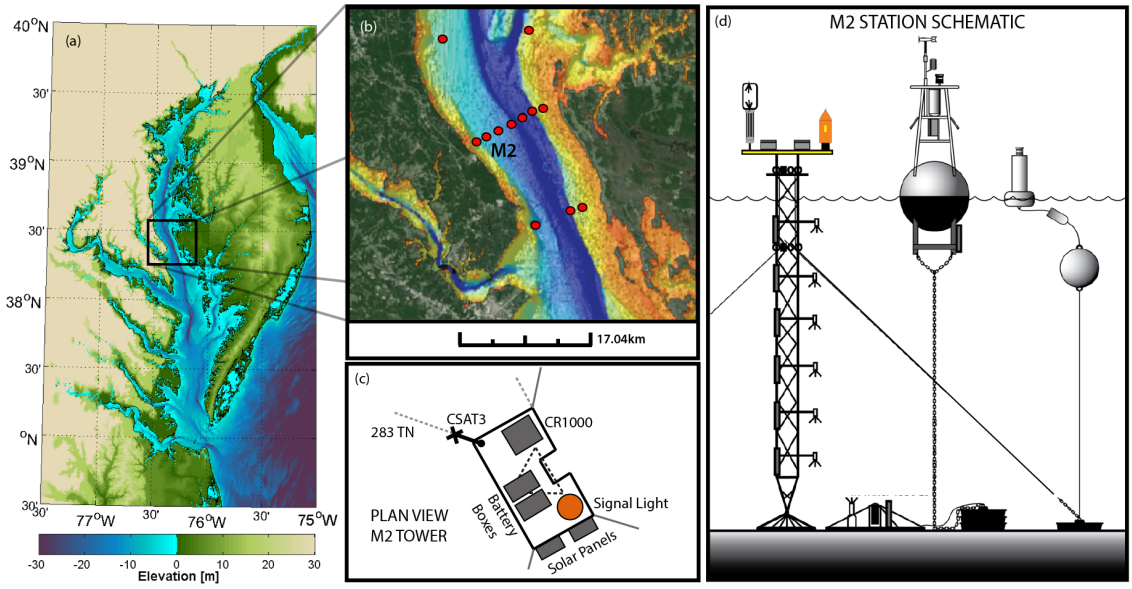

Figure 2.1 Study array. (a) Overview panel showing Chesapeake Bay with area of intensive observation shown as a black box. (b) Field array - red dots mark the locations of instrumented surface buoys with the M2 station noted (image created using Google Earth). (c) Plan view of the tower as it was oriented in the field. (d) Schematic of station M2 showing instrumentation on tower, surface buoy, and bottom lander.

2.2.4 Air-Sea Flux Measurements

Air-sea flux measurements were collected using a Campbell Scientific CSAT3 ultrasonic anemometer system mounted atop a stationary tower temporarily deployed in the mid-Bay. The 15 meter tower was deployed at M2 (38° 27' 17.28" N, 76° 25' 39.36" W) on March 16, 2012 and the anemometer recorded continuously until April 28, 2012. The MSL water depth at the tower was 12.8m and the average tidal range was ~0.5 meters. The sonic anemometer was mounted ~2.6m above MSL and the anemometer height was corrected for tidal elevation using the pressure record of a Nortek 6MHz Acoustic Doppler Velocimeter (ADV) mounted 2.46m below MSL on the tower. A schematic of the tower configuration is shown in Figure 2.1.

The sonic anemometer sampled the three dimensional velocity field at 10Hz and included a fine wire thermocouple which sampled air temperature at 10Hz. The open-path eddy covariance (OPEC) technique was used to calculate surface fluxes from high frequency velocity and temperature measurements. Due to the sensitivity of vertical flux measurements to small variations in vertical velocity, the orientation of the sonic anemometer was tested and corrected for axial tilt using the planar fit method (Wilczak et al 2001) prior to flux calculations. Tilt correction was performed on daily subranges of the data to account for the possibility of nonstationarity at longer time scales.

Air-sea fluxes were calculated using a 30 minute averaging window, which should provide a sufficient range of sampling scales to properly represent near surface turbulence (Lin et al 2002, Drennan et al 2003). Wind stress was calculated as the turbulent Reynolds stress defined as the average covariance between turbulent horizontal (u') and vertical (w') velocities multiplied by the density of air (ρ_{air}):

$$\tau = \rho_a \overline{u'w'} \tag{2.7}$$

Sensible and latent heat fluxes can be calculated using the following equations:

$$H_s = \rho_a c_a \overline{w'T'} \tag{2.8}$$

$$H_L = \frac{PL_{vap}}{0.51R\bar{T}^2}\left(\overline{w'T'_s} - \overline{w'T'}\left(\frac{\bar{T}_s}{\bar{T}}\right)\right) \tag{2.9}$$

where P is atmospheric pressure, L_{vap} is the latent heat of vaporization, R is the gas constant for dry air (287.04 J K^{-1} kg^{-1}), T is air temperature, and T_s is the sonic temperature defined as:

$$T_s = T(1 + 0.51q) \tag{2.10}$$

where q is the specific humidity. Overbars denote Reynold's averaged quantities. Average air temperature and humidity were also measured at the tower using a HMP45AC probe deployed as part of the CSAT3 system. The derivation of the above equations follows Kaimal and Businger (1963), Wallace and Hobbs (1977), Fleagle & Businger (1980), Schotanus et al 1983), Kaimal and Gaynor (1991), and Mortensen (1994).

2.2.5 Surface Wave Measurements

The uppermost tower ADV also provided wave information co-located with direct flux measurements. Pressure records for each burst were resampled from 32Hz to 8 Hz and were used to calculate wave spectra using the DIrectional WAve SPectra (DIWASP) Matlab toolkit after the data had been corrected for atmospheric conditions. Corrupted velocity data limited the analysis to nondirectional wave spectra. Autospectra were calculated using a Hamming window with 0% overlap and 256 NFFTS. The cutoff point for power spectral estimates was set at K_Z<=0.1, where K_Z is the pressure response function based on linear wave theory, which was approximately equal to 0.6Hz for the dataset. Spectral power estimates above this threshold were replaced with an f^{-4} tail and truncated at 2Hz. Significant wave height (H_{mo}), mean wave period (T_m), and peak period (T_p) estimates were calculated using spectral moments and the spectral peak, respectively.

2.2.6 Data Selection

A summary of wind, wave, and flux observations recorded at the tower is shown in Figure 2.2. Wind stress values ranging from near zero to greater than 0.7 Pa were recorded during the experiment under a variety of fetch conditions. Surface winds were dominated by frontal passages, which generally flowed along the estuary in successive, opposing pulses. Wave observations were dominated by pure wind seas with wave heights ranging from 0.2m to 1.2m with peak periods between 2-6 seconds. Wave heights less than 10cm were omitted from the analysis due to noise contamination in the pressure record of the ADV. To avoid turbulent wakes from the tower influencing flux

measurements collected by the sonic anemometer, periods when the wind blew from between 110° and 170° TN were omitted from the analysis.

Data used in the calculation of wave-dependent stress estimates were restricted to periods when U_{N10} was greater than 5m/s and at least $1.2C_p$ to limit the analysis to fully rough conditions during which spectral growth was occurring (Donelan 1990, Komen et al 1994, Lin et al 2002). This resulted in 672 usable data points.

2.2.7 Equilibrium State of Wind Waves

Under equilibrium conditions, a strong correlation is expected between the mean square slope (mss) of the sea surface and surface wind forcing (Phillips 1985, Thomson et al 2013). The mss can be estimated from the wave spectrum as:

$$\text{mss} = \int \frac{(2\pi f)^4 E(f)}{g^2} df \qquad (2.11)$$

To assess the frequency of equilibrium conditions in the mid-Bay, a time series of Pearson's correlation coefficient (R) between mss and u* measured by the sonic anemometer was calculated using a sliding 34 hour window (N=68 data points). During approximately 70% of the analysis period, R^2 values were greater than or equal to 0.65 indicating that waves were typically in equilibrium with local wind forcing. Abrupt changes in wind conditions associated with frontal passage or the relaxation period of a wind event likely caused temporary departures from equilibrium, but the majority of wave conditions observed in this study can be considered in fetch-limited equilibrium.

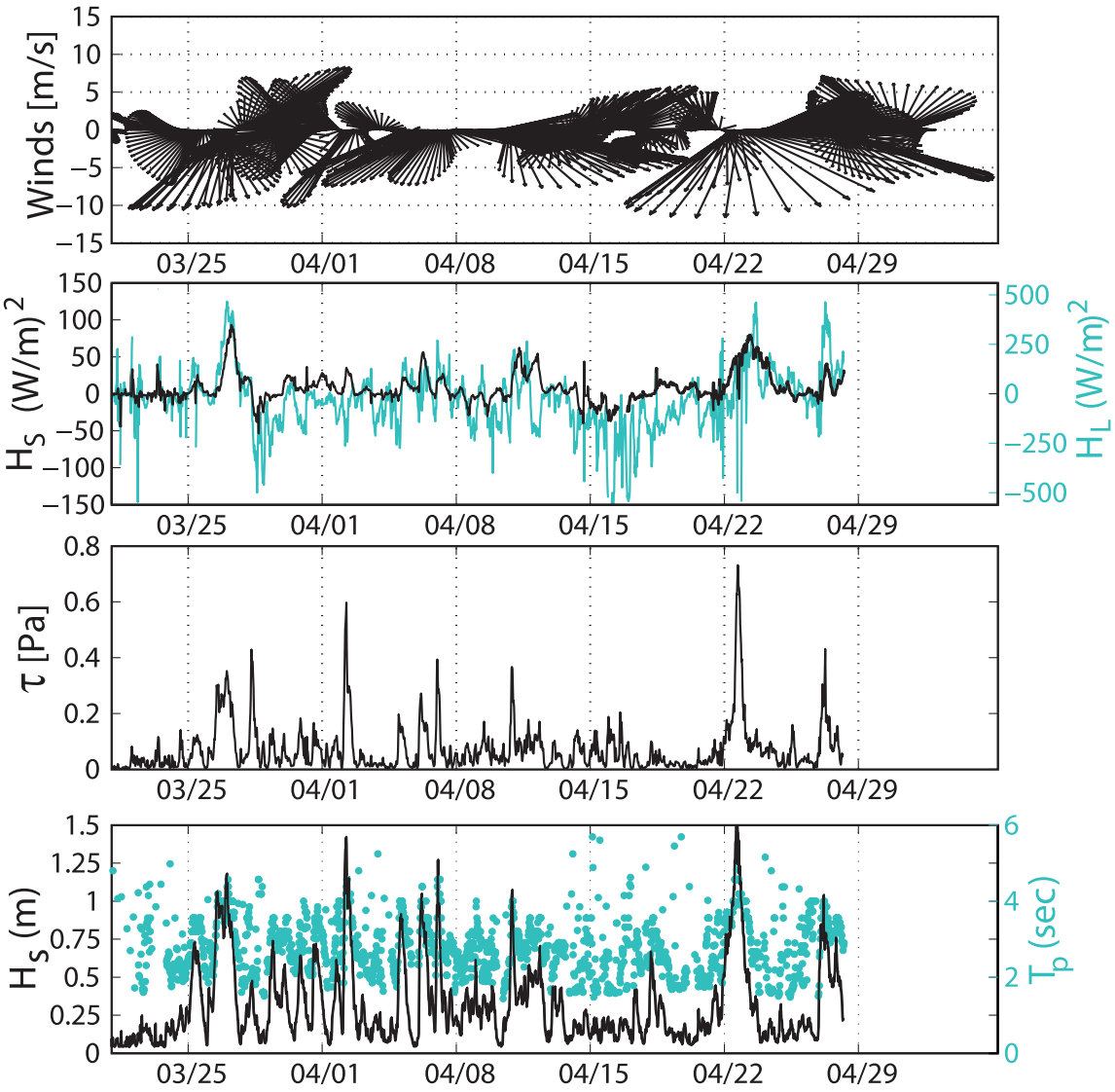

Figure 2.2 Observational summary for M2 during spring 2012 deployment. (a) 34 hour low-pass 10-meter neutral winds at M2 (b) heat fluxes [W/m^2] calculated from CSAT3 ultrasonic anemometer data (c) Stress [Pa] calculated from CSAT3 ultrasonic anemometer data (d) Significant wave height [m] and peak period [sec] calculated from uppermost tower ADV.

§2.3 Observed Wave Dependence of Wind Stress

In this section, we examine the variability of stress relationships described by the 10 meter neutral wind speed and surface wave characteristics. By comparing bulk wind stress calculations using a constant Charnock parameter to those made with a wave-dependent Charnock parameter, we explore the implications of coupled wind and wave dependent stress dynamics in a coastal embayment and factors influencing their variability.

In the absence of modeled or observed wave conditions, numerical models typically use a constant Charnock parameter in the bulk calculation of wind stress, which implies that the 10 meter drag coefficient is approximately a linear function of U_{N10} at moderate wind speeds (Drennan et al 2003, Edson et al 2013):

$$C_{D\,N10} = \left[A\left(U_{N10}\right) + B \right] \times 10^{-3} \qquad (2.12)$$

Results from the Riso Air-Sea Experiment, RASEX (Mahrt et al 1996, Vickers & Mahrt 1997), suggested that A=6.7 x 10^{-2} and B = 0.75. Data collected during the Marine Remote Sensing Program, MARSEN (Geernaert et al 1987), yielded A and B values of 8.47x10^{-2} and 0.577, respectively. Our experimental design closely resembles that of Lin et al 2002, whose results were that A = 6.49 x 10^{-2} and B = 0.699. Figure 2.3 shows $C_{D\,N10}$ vs. U_{N10} with curves suggested by RASEX, MARSEN, and Lin et al 2002. A best fit curve to our bin-averaged observations, using a bin size of 0.5m/s, gives A and B values of 7.52 x 10^{-2} and 0.667 (R^2=0.33), respectively.

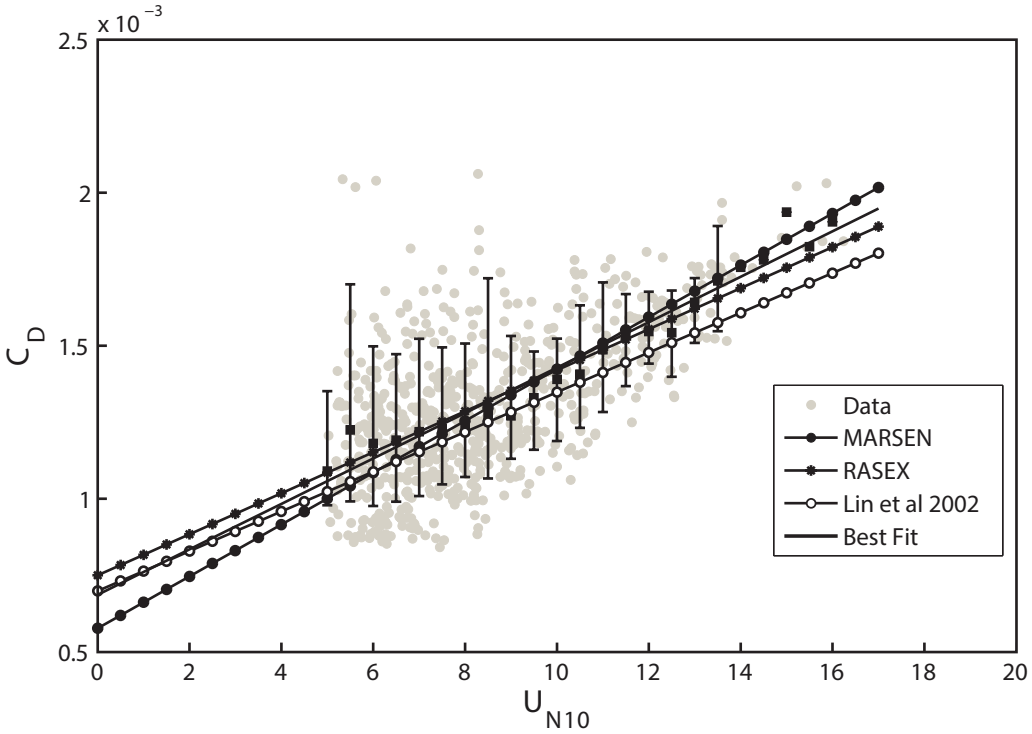

Figure 2.3 Comparison of $C_{D\,N10}$ vs U_{N10} calculated from ultrasonic anemometer data and curves suggested by MARSEN, RASEX, and Lin et al 2002. Raw data is shown in addition to bin-averaged data (0.5 m/s bins) with 2σ error bars.

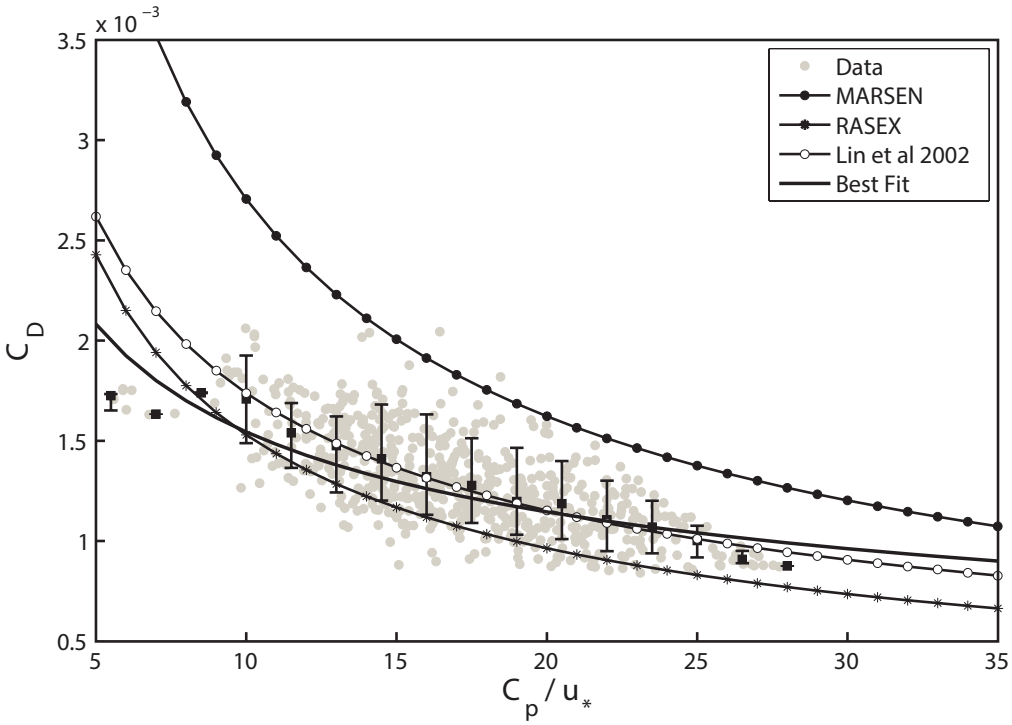

Figure 2.4 Comparison of $C_{D\,N10}$ vs wave age and curves suggested by Geernaert et al 1986, RASEX, and Lin et al 2002. Raw data is shown in addition to bin-averaged data (1.5 bins) with 2σ error bars.

It is clear that the while U_{N10} can be used to describe the general trend in $C_{D\,N10}$, significant scatter suggests that other parameters may be needed to accurately model variations in $C_{D\,N10}$. One of the most common wave-based parameterizations of $C_{D\,N10}$ is a wave age formulation, in which wave age is defined as the phase speed of the waves C_p normalized by either u_* or U_{N10}:

$$C_{D\,N10} = A\left(\frac{C_p}{u_*}\right)^B \qquad (2.13)$$

in which A and B are empirical constants . RASEX results are that A and B are equal to $7.1\text{x}10^{-3}$ and -0.667, respectively. Geernaert et al 1986 found A and B to be $1.48\text{x}10^{-2}$ and -0.738, respectively. Lin et al 2002 found A and B to be $6.79\text{x}10^{-3}$ and -0.592, respectively. The 10 meter neutral drag coefficient is plotted against wave age in Figure 2.4 with curves suggested by RASEX, Geernaert et al 1986, and Lin et al 2002. There is significantly less scatter than shown in the U_{N10} formulation of $C_{D\,N10}$ shown previously, which may be due in part to autocorrelation. However, our observations agree very well with the curve suggested by Lin et al 2002, which is expected given that Lin et al 2002's results were also calculated from measurements collected in the mid-Bay using similar field techniques. A best fit curve to our bin-averaged data gives $A=4.1 \times 10^{-3}$ and B= -0.431 (R^2=0.40).

In the bulk theory, the dependence of wind stress on surface waves is communicated primarily through Charnock's parameter prompting a need for wave-based

formulations of alpha. In the following section, we compare two wave-dependent formulations of alpha that account for the wave age either explicitly or implicitly.

2.3.1 Wave Age Formulations of the Charnock Parameter

Kitaigorodskii (1973) proposed that wave age should be used to model alpha. This wave age-dependent form of the Charnock parameter has since been adopted by numerous studies in the general form (Edson et al 2013, Smith et al. 1992, Johnson and Vested 1992, Johnson et al. 1998, and Oost et al. 2002):

$$\frac{z_0^{rough} g}{u_*^2} = A\left(\frac{u_*}{C_p}\right)^B \qquad (2.14)$$

where A and B are empirical constants. Wind speed parameterizations of Charnock's alpha usually contain significant scatter which is often attributed to wind event duration, fetch, and water depth – wave age accounts for these variables and as such may provide a better estimate than wind speed alone. For measurements taken over the open ocean (unlimited fetch, deep-water), Edson et al (2013) found that A=0.114 and B=0.622. A curve fit to our binned data (binned using a 0.0125 bin size) resulted in A and B being equal to 0.137 and 0.928, respectively (Figure 2.5). The fitted curve had R^2 and RMSE values of 0.73 and 5.2 x 10^{-3} respectively. Depth-effects likely became a dominant factor influencing wave age during large wind events - ~10% of the data considered in this comparison consisted of waves at intermediate water depth ($1/20 < h/\lambda < 1/2$). Bin-averaged observed alpha values ranged from 0.0035 for relatively mature waves and asymptoted to approximately 0.02 for relatively young seas. It should also be noted that

few data points were available for bin-averaging alpha at very young wave ages, which is a potential source of error in the curve parameters.

It has been suggested that a cubic dependency between inverse wave age and wind speed can be used to express alpha as a function of wind speed using a wave age dependency of the form of Equation (2.14) (Edson et al 2013). While our data do exhibit an approximately linear relationship between inverse wave age and wind speed, there is significant scatter when alpha is plotted versus U_{N10}. Additionally, the observed inverse wave ages are consistently higher for a given wind speed than reported by Edson et al (2013). This is likely due to younger, steeper waves being more typical in the fetch-limited environment of Chesapeake Bay than waves observed in the open ocean.

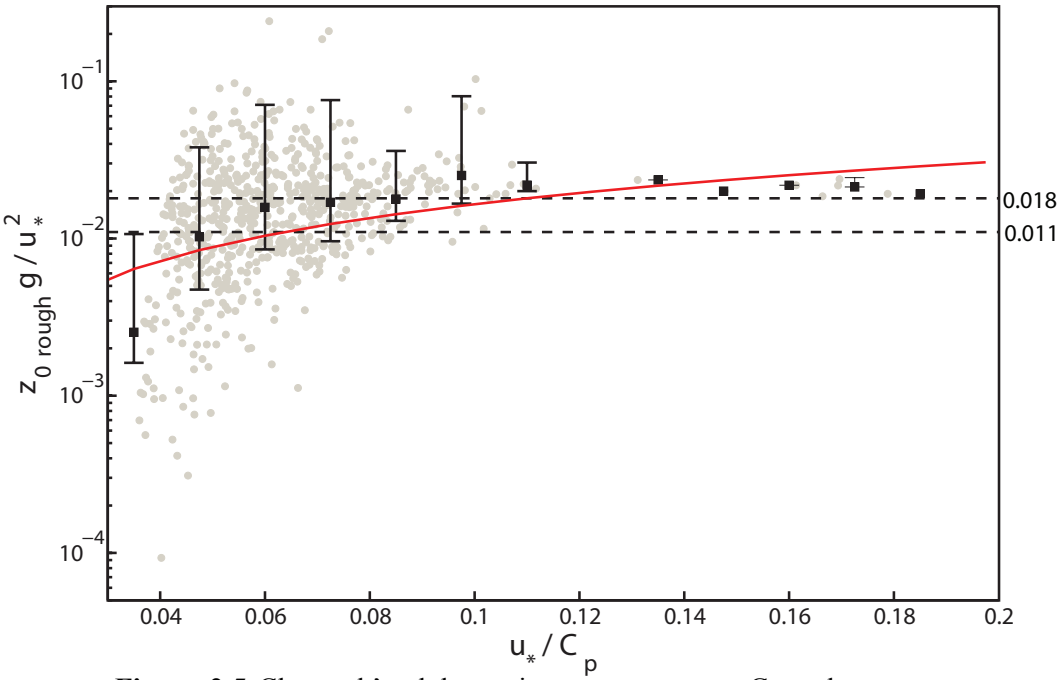

Figure 2.5 Charnock's alpha vs inverse wave age. Grey dots represent raw data, box plots represent bin-averaged data using a 0.0125 bin size, and the solid red line is a best fit curve of the form of Equation (2.14). Note that alpha values observed in Chesapeake Bay display a range (dashed lines) that spans constant alpha values typically prescribed to coastal fetch-limited (0.018) and open ocean environments (0.011).

2.3.2 Wave Slope Formulations of the Charnock Parameter

The Charnock parameter is a ratio of gravitational forces to inertial forces and is therefore analogous to an inverse Froude number (Edson et al 2013). As such, Charnock's parameter can be expressed as a linear function of wave slope (using the definition outlined by Kraus & Businger 1994):

$$\frac{z_{0rough}g}{u_*^2} = D\left(H_s k_p\right) \tag{2.15}$$

where D is an empirical constant, H_s is significant wave height, and k_p is the peak wavenumber. This scaling approach accounts for sea state, wave age, and aerodynamic roughness and may enable the development of a universal parameterization of alpha (Edson et al 2013). Several studies have used the deep water dispersion relation to express Equation (2.15) in terms of a scaled roughness as a function of inverse wave age with reasonable agreement (Donelan 1990, Smith et al 1992, Dobson 1994, Martin 1998, Drennan et al 2003):

$$\frac{z_{0\,rough}}{H_S} = D\left(\frac{u_*}{C_p}\right)^2 \tag{2.16}$$

where H_S is the significant wave height. Edson et al (2013) show that a value of D=0.09 produces stress estimates which are comparable over the open ocean to those given by the wave age relationship discussed previously. Using the same averaging method discussed

previously, a best fit curve of the form of (Equation 2.16) to our bin-averaged data (Figure 2.6) suggests that D=0.0547 (R^2=0.95, RMSE=1.8 x 10^{-4}).

2.3.3 Quantifying Spurious Auto-Correlation in Wave-Dependent α Formulations

Spurious autocorrelation is likely to affect the results of both the wave age and wave slope formulations of alpha (Eqn 2.14 and Eqn 2.16, respectively). To quantify the impact of autocorrelation on the relations found in this observational dataset, we perform a randomization test to estimate the relative degree of autocorrelation expected for the two formulations following a method similar to that outlined in Andreas (2009) and Hwang (2010).

The test was performed on raw data by randomizing observed wave phase speeds, while wave height, u_*, and $z_{0\,rough}$ were held in position. Correlations were calculated for 10,000 trials based on Equations (2.14) and (2.16). Taking the mean of these trials gives an estimate of the autocorrelation inherent in each functional form of wave-dependent alpha. Results indicate that spurious autocorrelation comprises only 27.5% and 38.7% of the correlation observed in the wave age and wave slope formulations of alpha, respectively, indicating that the formulations indeed represent real physical dependencies.

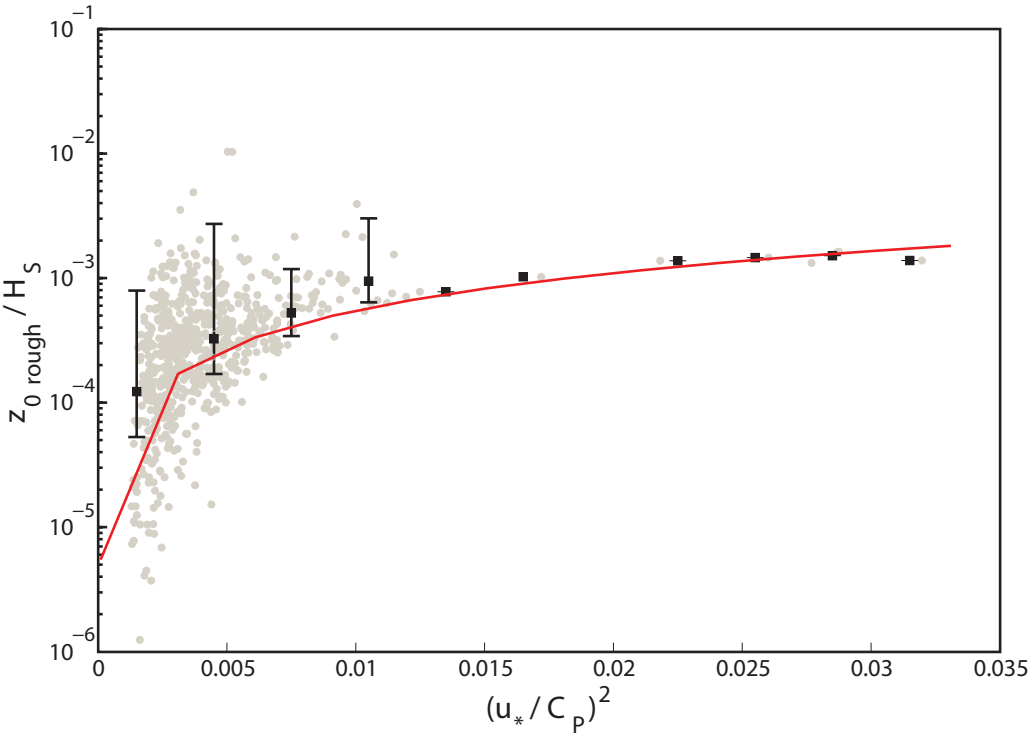

Figure 2.6 Scaled roughness vs inverse wave age squared. Grey dots represent raw data, box plots represent bin-averaged data using a 0.003 bin size, and the solid red line is a best fit curve of the form of Equation (2.16).

2.3.4 Observations vs. Bulk Theory Predictions

Calculations of u_* using the wave age (Eqn 2.15) and wave slope (Eqn 2.16) formulations and a calculation of u_* using a constant alpha=0.018 (Wu 1980) are compared to measured shear velocities in Figure 2.7. Both the wave age and wave slope formulations produce very similar estimates of u_* and outperform the constant alpha parameterization with higher R^2 values and lower RMSE values. This being said, all three parameterizations predicted observed u_* velocities very well with low RMSE values and linear regression curves which had high R^2 values and slopes near unity. A full summary of fit statistics is given in Table 2.1. While bulk stress estimates based on a constant alpha are a good mean estimate of observed wind stress, the wave-dependent formulations better represent the transition to fetch-limitation which occurs for a variety of wind conditions in coastal environments. As shown in Figure 2.7, accounting for surface waves in the estimates of stress reduced the bias of predicted values to below 5% for all but the highest stress events.

2.3.5 Near Surface Stability Effects

We also explored the effects of ignoring atmospheric stability corrections, as might be required if, for example, there was no information available on air-sea temperature differences. We compared the 10 meter neutral drag coefficient estimated using COARE 3.0 scalar stability profiles to a 10 meter drag coefficient expected under assumed neutral conditions. This was done by omitting the $\psi\left(\frac{z}{L}\right)$ term from Equation

(2.1). Results indicate that under stable conditions, near surface stratification may reduce wind stress by approximately 10%. Under unstable conditions, wind stress may be up to approximately 5% higher than estimates calculated assuming neutral conditions. These errors are likely to be in the same sense as the errors due to ignoring surface wave effects on drag coefficients, because stable (unstable) conditions should lead to higher (lower) wave age, leading to a decrease (increase) in the wave-affected drag coefficient.

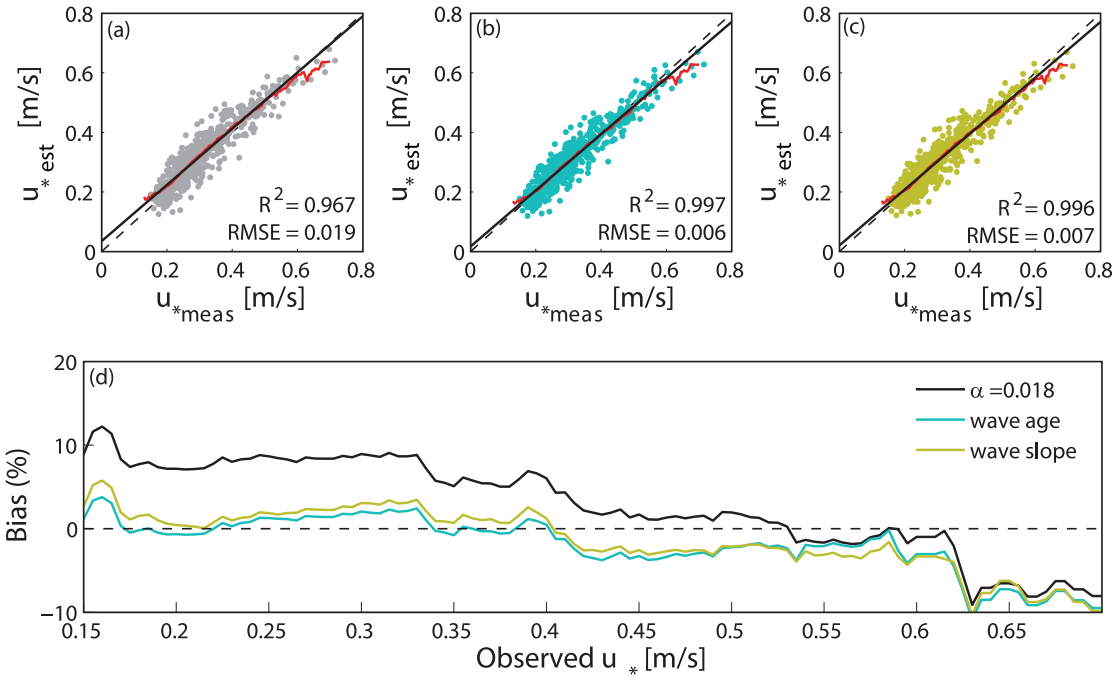

Figure 2.7 Comparison of bulk estimates of u_* to observations using three parameterizations of alpha: (a) a constant alpha=0.018, (b) wave age formulation, and (c) wave slope formulation. A linear regression (solid black line) of u_* estimates calculated using a constant alpha of 0.018 vs measured values yielded a slope of 0.944 and intercept of 0.035. The wave age and wave slope formulations yielded regression curves with slopes of 0.943 and 0.939 and intercepts of 0.017 and 0.020, respectively. Bin-averaged data, using a bin size of 0.05 m/s, are shown as a solid red curve. (d) Bias, defined as the normalized difference between bin-averaged bulk estimates and observations, as a function of observed u_* values. Both the wave age and wave slope formulations reduced the bias to below 5% for all but the highest observed stress events.

Table 2.1: Fit summary for bulk u* estimates using a constant alpha and wave-dependent formulations

	Slope	Intercept [m/s]	R^2	RMSE [m/s]	Bias [m/s]
$\alpha = 0.018$	0.944	0.035	0.967	0.019	0.018
$\alpha = 0.137\left(\frac{u_*}{C_p}\right)^{0.928}$	0.943	0.017	0.997	0.006	-8.87×10^{-4}
$\frac{z_0^{rough}}{H_s} = 0.0547\left(\frac{u_*}{C_P}\right)^2$ – or – $\alpha = 0.0547 H_s k_p$	0.939	0.020	0.996	0.007	0.002

§2.4 Modeling Basin-Scale Variability

Direct observations of wind stress and surface wave dependence presented in the previous section have contributed to a growing body of literature on wave dependent bulk transfer functions, however a major question that still exists is how these transfer functions vary in the coastal ocean where fetch-limitation varies spatially. In this section, we present an analysis of wave-dependent stress estimates modeled over the extent of Chesapeake Bay using wave dependencies determined from our observations. It is reasonable to expect that modeled alpha values would exhibit a transition from open ocean conditions (alpha = 0.011) to fetch-limited conditions (alpha >=0.018), depending on wind direction and the geometry of Chesapeake Bay.

Our objective is to illustrate the potential importance of fetch limited surface waves in structuring wind stress variability in coastal environments. The model results do

not account for wind stress variability stemming from surface boundary layer adjustment, shadow zones, or wave-current interaction, all of which are likely to increase the spatiotemporal variability of stress dynamics in a realistic environment.

2.4.1 Model Description

To explore the spatial variability of wind stress dynamics in Chesapeake Bay, we employ a third-generation numerical wave model, Simulating WAves Nearshore (SWAN version 40.91). The nonstationary model solves the spectral action density equation on a 5 minute computational timestep and accounts for tidal elevation and bottom friction through the default, empirical JONSWAP model (Hasselman et al 1973). Wind wave growth is parameterized using the Zijlema et al (2012) formulation of the drag coefficient in combination with the Komen et al (1984) expression for exponential wave growth.

The simulation period was from March 25, 2012 to April 1, 2012. The curvilinear computational grid has 39204 grid points and an average grid resolution of 0.9 km x 1.3km over the main stem of Chesapeake Bay. NOAA buoy 44014 outside the mouth of Chesapeake Bay was used as the oceanic wave boundary condition. Records from NOAA tidal stations listed in Table 2.2 were interpolated to provide water level information for the simulation period.

Wind-wave generation was forced using an optimally interpolated wind field that was calculated from a combination of surface buoys deployed as part of this study, 10 Chesapeake Bay Interpretative Buoy System (CBIBS) buoys, 34 National Climate Data Center (NCDC) stations, and 14 WeatherFlow stations (65 total stations). Stations were

selected based on data availability and site elevation. Stations located at elevations greater than 15m above the surface were excluded from the analysis.

Table 2.2: Tide stations used in interpolation of water level for SWAN input

Baltimore, MD	8574680	39° 16’ N	76° 34.7’ W
Chesapeake City, MD	8573927	39° 31.6’ N	75° 48.6’ W
Annapolis, MD	8575512	38° 59’ N	76° 28.8’ W
Tolchester Beach, MD	8573364	39° 12.8’ N	76° 14.7’ W
Cambridge, MD	8571892	38° 34.4’ N	76° 4.1’ W
Solomons Island, MD	8577330	38° 19 ‘ N	76° 27.1’ W
Bishops Head, MD	8571421	38° 13.2’ N	76° 2.3’ W
Lewisetta, VA	8635750	37° 59.7’ N	76° 27.8’ W
Windmill Point, VA	8636580	37° 36.9’ N	76° 17.4’ W
Yorktown, VA	8637689	37° 13.6’ N	76° 28.7’ W
Kiptopeke, VA	8632200	37° 9.9’ N	75° 59.3’ W
Chesapeake Bay Bridge Tunnel, VA	8638863	36° 58’ N	76° 6.8’ W

Wind, atmospheric temperature, and water temperature observations were used to adjust over-water wind observations to uniform 10 meter neutral conditions prior to interpolation. Over-land stations were corrected using a standard log profile. A universal kriging scheme was used with an algorithmically-fit exponential variogram model to interpolate u (E-W) and v (N-S) wind components independently for each 30 minute timestep. A rectilinear grid with uniform 5km grid spacing was used for interpolation. More information on the kriging analysis can be found in Appendix A.

An iterative procedure was used to evaluate wave-dependent wind stress development in the estuary. The wave model was initialized with the kriged 10 meter neutral wind field where overwater stations were adjusted using the bulk formulae with a constant Charnock alpha of 0.018 (Wu 1980). Modeled wave parameters were then used to calculate new Charnock alpha values using Equation (2.14) with A=0.137 and B=0.928. These new Charnock alpha values were used to readjust wind observations to neutral conditions, which were then kriged and used to force the wave model. Results were considered steady when modeled u_* values converged to within a 0.001 threshold for all timesteps, which occurred in less than 3 iterations per time-step for all grid points.

2.4.2 Model Validation

The model was validated using wave measurements from the M2 ADV and observations from 5 CBIBS stations, which provided greater spatial coverage of the bay (Figure 2.8). Wave spectra were compared for M2 and a comparison of significant wave height and peak period are shown in Figure 2.9. Wave observations collected at CBIBS stations were reported as significant wave height and mean period; a comparison of these two parameters to SWAN model output is shown in Figure 2.10. Modeled wave parameters agree very well with observations at M2 and generally agree with CBIBS observations collected over a broader range of Chesapeake Bay.

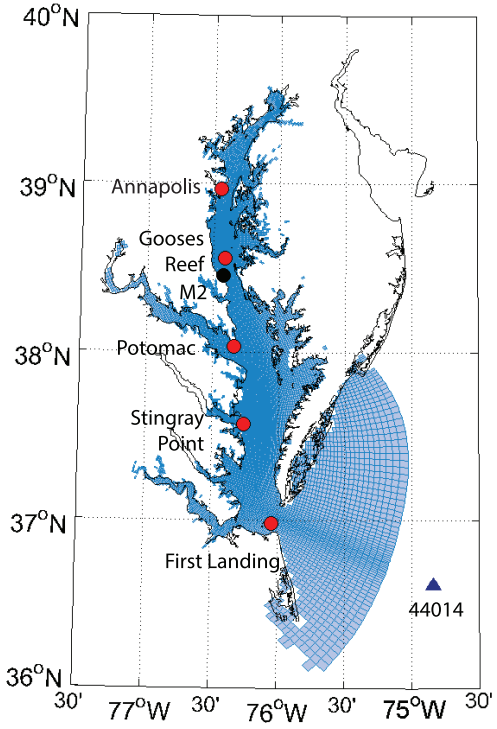

Figure 2.8 Model Domain with CBIBS stations used in model validation (red dots), M2 (black dot), and buoy 44014 (blue triangle) used as the oceanic wave boundary condition.

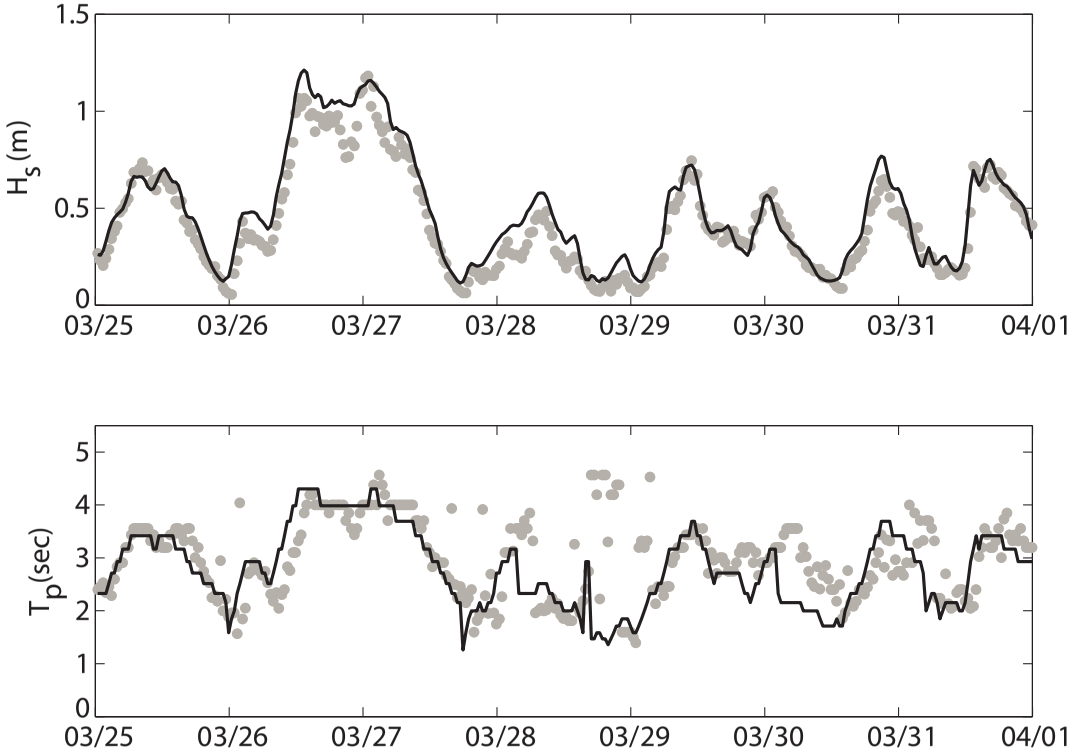

Figure 2.9 Model comparison to observations at M2. Grey dots represent observations, black lines represent model output.

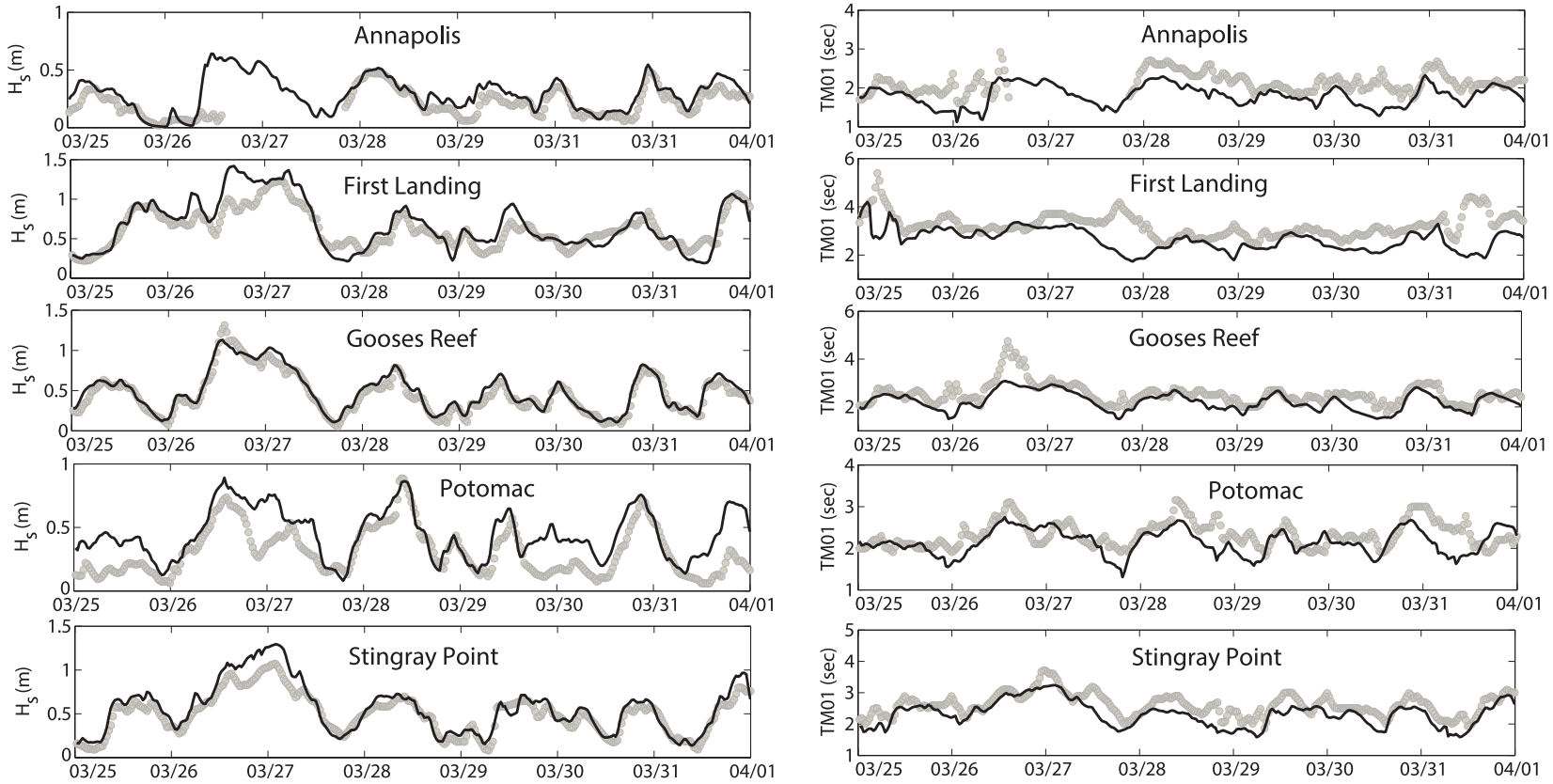

Figure 2.10 Model comparison to wave parameters measured at CBIBS buoys. Grey dots represent observations, black lines represent model output.

2.4.3 Spatiotemporal Variability

Model results suggest that wind stress dynamics in Chesapeake Bay may exhibit significant spatiotemporal variability stemming from variable wind forcing patterns and surface wave fields. During the simulation period, the spatial mean wind speed ranged from 2-12 m/s, but the significant spatial spread in both wind speed ($\pm$ 2 m/s) and wind direction ($\pm$ 10°) shows that the wind field over Chesapeake Bay is at times complex and nonuniform (Figure 2.11). As wind speeds increased, the directional spread in the wind field typically decreased. At times of low wind speed, wind direction often spanned ranges greater than 60 degrees. The physical processes that contribute to this spatial variability are still poorly resolved, but may include sea breezes, varying surface roughness, frontal passages and other mesoscale processes.

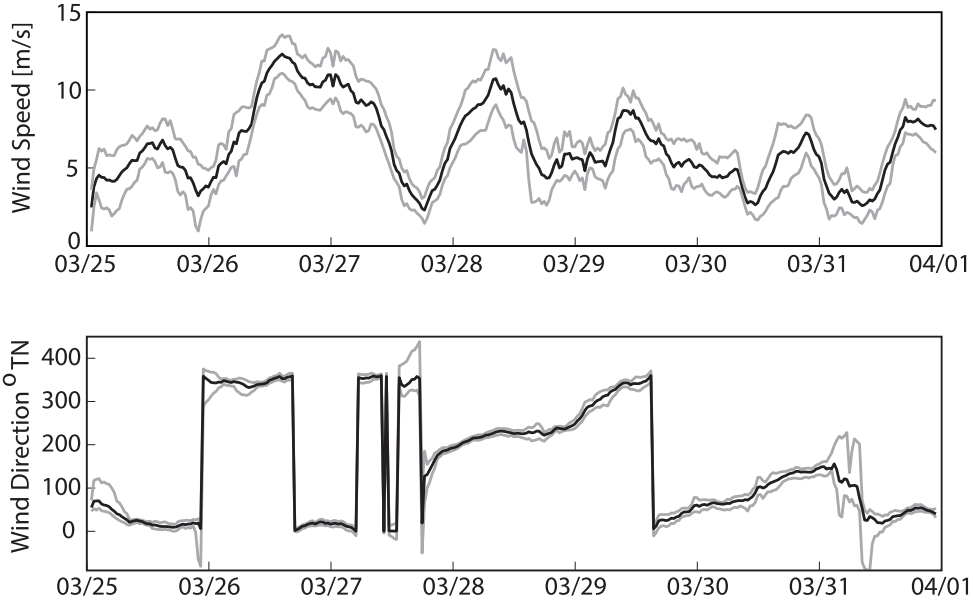

Figure 2.11 Wind speed and direction during model simulation period: black line is the spatial average of the kriged wind field; grey lines represent the interquartile range (IQR). Note that significant spread can exist around the average wind speed, suggesting that winds over Chesapeake Bay can be complex and nonuniform even at moderate to high wind speeds.

Figure 2.12 shows the spatial mean and interquartile range of alpha values simulated in the model domain. While the spatiotemporal mean alpha value during the simulation period was calculated as 0.012, alpha values range from less than 0.005 to greater than 0.02 during the simulation period and display significant spread in their spatial distributions. Interestingly, a modeled mean value of 0.012 agrees well with the constant suggested by Charnock (1955). Alpha values increase with increasing wind speed, a trend that is in agreement with Edson et al (2013). Additionally, the general increase in the interquartile range of modeled alpha values with increasing mean wind speed highlights the importance of fetch-limitation in modeling wind stress in the coastal environment. As wind speed increases over Chesapeake Bay, spatially variable fetch-limitation increases the range of sea states within the model domain and increases the variability of alpha values, which under certain conditions can span the entire range of typical open-ocean to fetch-limited values at the same time. This may have important implications for wind-induced modifications to estuarine circulation and vertical mixing generated by moderate to large wind events; the spatial structure of these responses may exhibit increased variability stemming from surface wave effects.

A similar analysis was performed for $C_{D\ N10}$, shown in Figure 2.13. Modeled values of $C_{D\ N10}$ are shown to increase linearly with increasing wind speed and a linear regression (of the form of Eqn 2.14) of bin-averaged $C_{D\ N10}$ yielded A= 9.60×10^{-2} and an B=0.539. As expected the spread of $C_{D\ N10}$ is less than that of alpha, but a positive correlation between the range in $C_{D\ N10}$ and wind speed similar to that observed for alpha reflects the potential importance of fetch-limited wave growth in determining the development of stress within the estuary. The modeled trends of $C_{D\ N10}$ combined with

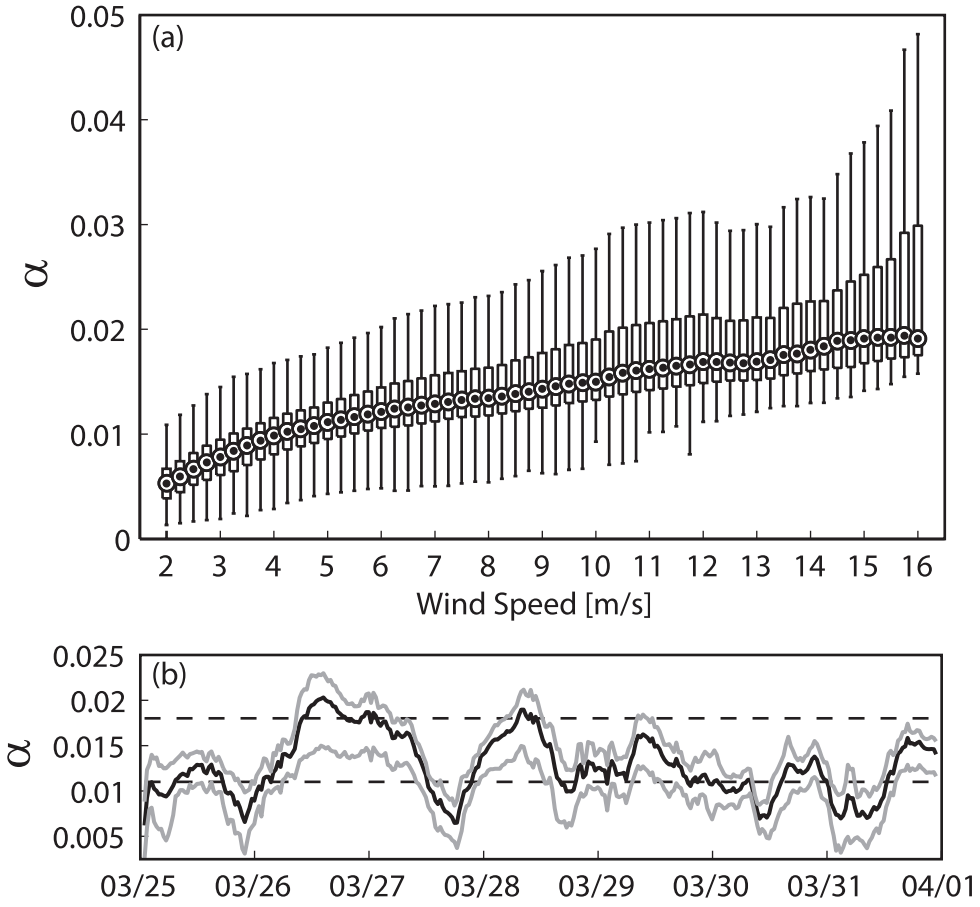

Figure 2.12 Modeled alpha values during the simulation period. (a) Tukey boxplot of simulated alpha values versus U_{N10} using a 0.25m/s bin size (b) Time series of spatial mean alpha values (black line) and their interquartile range (grey lines). At times, alpha values may range from values typically prescribed to the unlimited fetch (0.011) and fetch-limited (0.018) conditions.

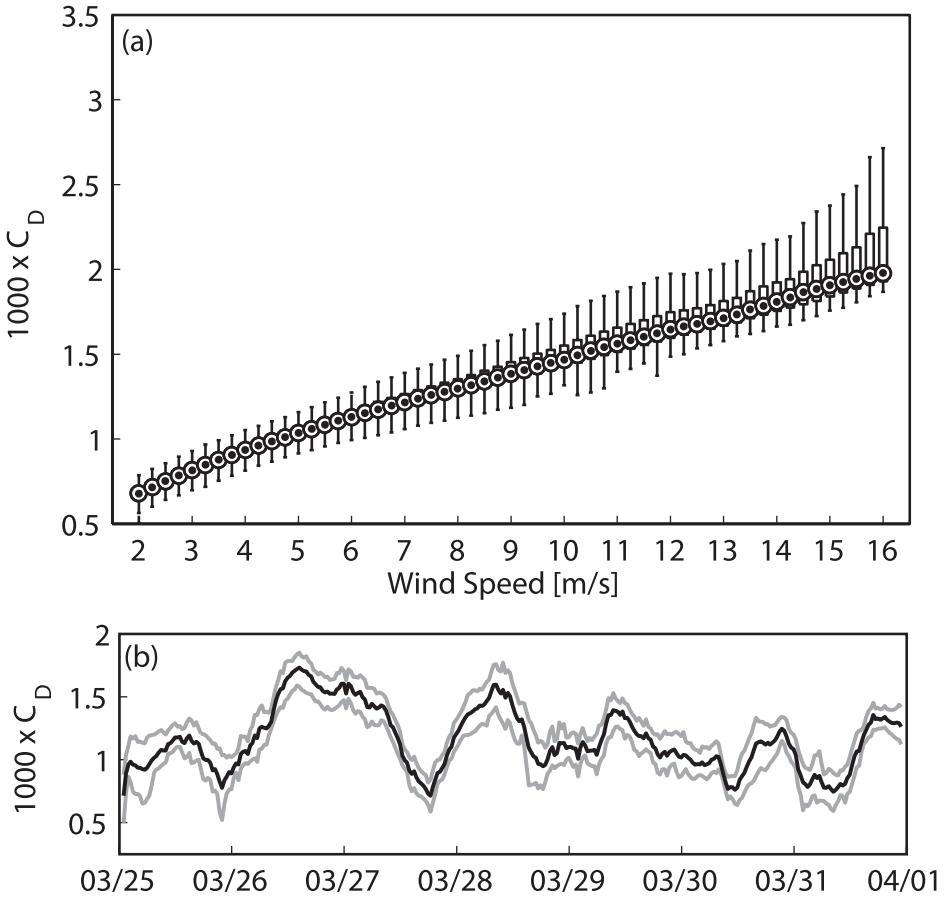

Figure 2.13 Modeled $C_{D\,N10}$ values during the simulation period. (a) Tukey boxplot of simulated $C_{D\,N10}$ versus U_{N10} using a 0.25m/s bin size (b) Time series of spatial mean $C_{D\,N10}$ values (black line) and their interquartile range (grey lines).

variability present in the wind field (Figure 2.11) used to force the wave model suggest that wind stress magnitude likely varies significantly over the estuary during the simulation period and is a strong function of wind speed and wave age. A closer examination of the wave-dependent alpha term used in estimates of stress and $C_{D\ N10}$ provides a means of exploring the structure of wave-dependent stress variation in Chesapeake Bay.

A map of modeled alpha values is shown in Figure 2.14 for March 28, 2012 1430 UTC when the measured wind stress at M2 was 0.385 Pa. The wind was directed primarily from the southwest with a mean wind speed of 9.89 m/s, but displayed significant variability in both magnitude and direction over the bay. The largest waves occurred near Rappahannock Shoals (37° 38' 24" N, 76° 0' 0''W) with significant wave heights of 1.5m and 5 second peak periods. Interestingly, this location did not correspond to the highest alpha values, which instead occurred in the lee of the land in the middle and lower Bay. The spatial distribution of alpha within Chesapeake Bay ranges from values of ~0.01 to ~0.02, while alpha values over the shelf are more tightly distributed around 0.01. In the upper Bay, where wind speeds are low, alpha values (~0.01) correspond to those typically observed in open ocean conditions while in the lower Bay alpha values are higher reflecting fetch-limited wave growth under higher wind speeds. Figure 2.13 indicates that the wave age formulation for alpha can account smoothly for variations associated with the transition from unlimited fetches in the open ocean to fetch-limited conditions within a coastal embayment.

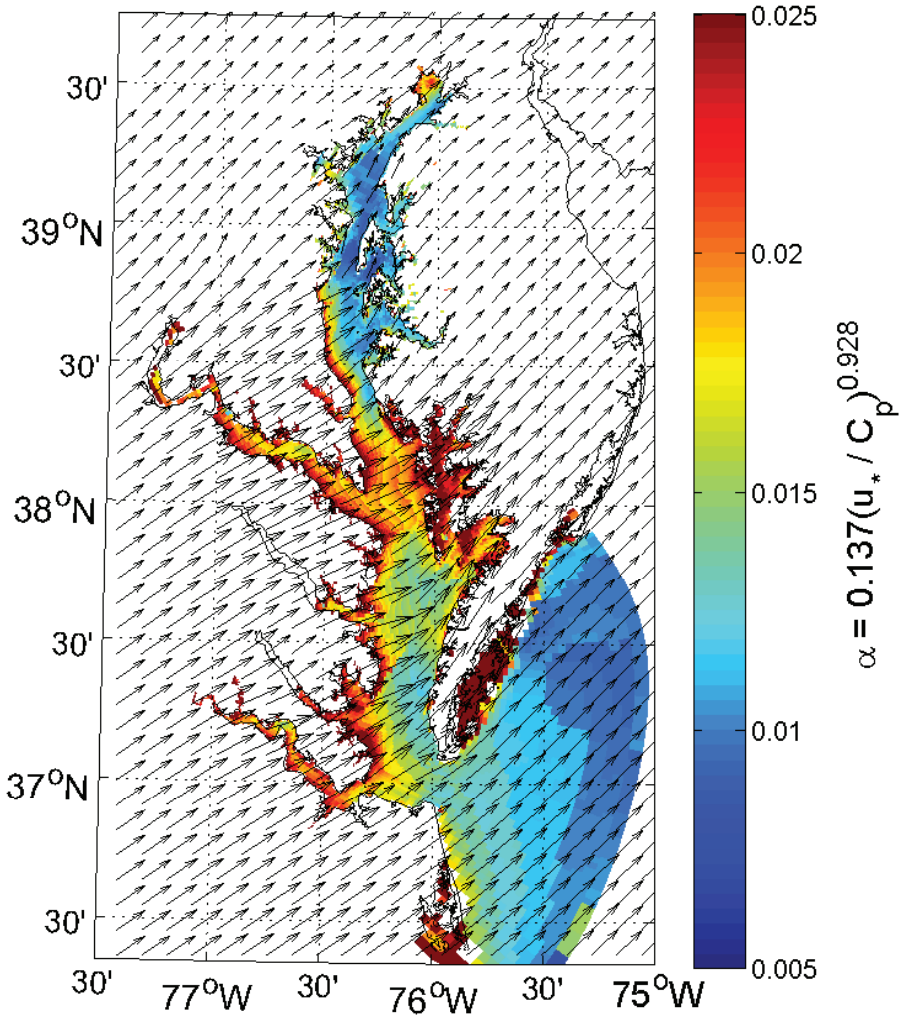

Figure 2.14 Modeled Charnock's alpha values for March 28, 2012 at 14:30 UTC when the observed stress at M2 was 0.385 Pa. Wind vectors also shown for 10 meter neutral conditions interpolated from observations as described in Appendix A.

Using the wave age formulation for alpha, we examined the variability of $C_{D\,N10}$ across the estuary for the same period shown in Figure 2.14. Figure 2.15 shows that the drag coefficient can vary by nearly a factor of 2 across the estuary with values between 0.9 and 1.75 x 10^{-3}. Over the shelf, $C_{D\,N10}$ is relatively uniform with a mean value of ~1.3 x 10^{-3}. $C_{D\,N10}$ exhibits significant spatial structure in Chesapeake Bay because of a combination of complex surface winds and varying degrees of fetch-limitation. In the upper Bay where wind speed was equal to 3.40 $\pm$ 1.74 m/s, wind stress was equal to 0.017 $\pm$ 0.019Pa while in the lower Bay wind speed was equal to 8.90 $\pm$ 1.74 m/s and stress was equal to 0.15 $\pm$ 0.08Pa. Comparing the drag coefficients calculated using a constant alpha of 0.018 against $C_{D\,N10}$ calculated using the wave age formulation, suggests that wave age dependence can result in up to an additional 20% variability in wind stress estimates.

2.4.4 Additional Sources of Variability

The modeling results discussed above illustrate that surface gravity waves can produce up to a 20% change in wind stress estimates resulting from fetch-limited wave growth, relative to standard bulk formulations. Additional sources of variability in coastal environments include the effects of tides and boundary layer adjustment resulting from reductions in surface roughness that occur as wind blows from land to sea (Perrie & Toulany 1990, Markfort et al 2010). We have partially accounted for changing surface roughness by correcting terrestrial wind stations using a standard power law in the interpolation scheme used to generation wind forcing files (Appendix A), but this procedure does not account for internal boundary layer adjustment.

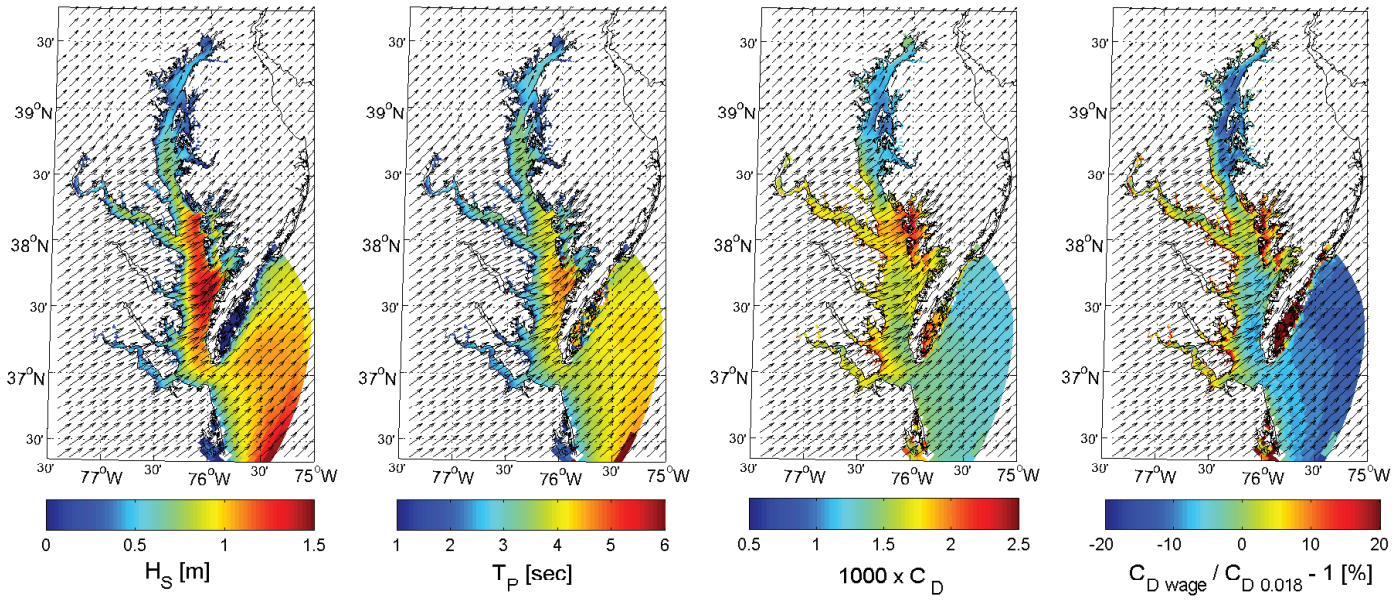

Figure 2.15 Sample model output for the same time period shown in Figure 14. (a) Significant wave height [m]. (b) Peak period [sec]. (c) $C_{D\,N10}$ calculated using the wave age formulation of alpha (Eqn 2.14). Note that the drag coefficient may vary by as much as a factor of two across the estuary, but is more uniform over the shelf. (d) Normalized difference between $C_{D\,N10}$ calculated using a wave age formulation of alpha and a $C_{D\,N10}$ calculated using a constant alpha of 0.018. Model results suggest that surface waves can produce up to 20% change in stress estimates.

The development of internal boundary layers in the lee of bluffs and forested shorelines can result in reduced stress on the water surface in the nearshore. In a study of wind sheltering over small lakes, Markfort et al (2010) found that tree canopies and bluff topography which have an effective height, h_c, can produce "shear deficit" zones which may extend 40-60h_c in the lee of these features on the lake surface. The effective canopy height is dependent on leaf area index with typical values for woodland forests of 8-15m (Garratt 1992, Markfort et al 2010). For nonporous features like coastal bluffs, the effective height is simply the elevation above the water surface (Cassiani et al 2008). A prominent feature in the middle reaches of Chesapeake Bay is Calvert Cliffs, a 30m bluff on the western shore of Chesapeake Bay north of Cove Point. Assuming the cliffs support a woodland canopy that has an effective canopy height of 10m, a 2km shadow zone can be expected in the lee of the cliffs. During our deployment and simulation periods, the shadow zone would have been most prominent during southwesterly winds and likely would have been west of our tower site. This example illustrates a source of variability in the nearshore environment that was not explicitly accounted for in the modeling results presented in this study and would benefit from further research.

The presence of relatively strong tidal currents in the coastal environment represents another potential source of wind stress variability through wave-current interaction. Assuming typical wave and tide conditions in Chesapeake Bay (barotropic tidal current=50 cm/s, H_s=1m, T_p=4 sec, depth=14m), Equation (2.15) suggests that wave steepening in the presence of an opposing tidal current (through wavelength reduction) can produce up to a 5% increase in stress estimates. Tidal shear may also modulate the wave field through refraction and focusing. However, the additional complications added

by wave-current interaction in structuring wind stress variations in Chesapeake Bay are beyond the scope of this paper.

§2.5 Conclusions

Wind stress dynamics in coastal environments may exhibit significant variability stemming from variable surface winds and wave-dependent stress development. As part of a collaborative investigation of wind-driven estuarine physics, air-sea flux measurements were collected in the middle reaches of Chesapeake Bay where the wave climate is dominated by pure wind seas. These observations were compared to co-located wave measurements to assess wave-dependent formulations of Charnock's alpha and the 10 meter neutral drag coefficient. Results indicate that standard bulk estimates of wind stress reasonably represent measured values, but the inclusion of surface wave variability effects in estimates of wind stress can improve predictions across a range of measured stress values. Estimates calculated using wave age and wave slope formulations of alpha produce similar improvements in bulk estimates.

Using a wave age relationship calculated from direct flux measurements and an optimally interpolated surface wind field, a third-generation numerical wave model was used to assess the spatiotemporal variability of modeled stress dynamics in Chesapeake Bay. Model results suggest that winds over Chesapeake Bay can at times be complex and nonuniform and generate a surface wave field that exhibits varying degrees of fetch-limitation. The combined effect of variable surface winds and fetch-limited wave growth results in estimates of $C_{D\,N10}$ varying by a factor of 2 across the estuary and spatial

distributions of alpha ranging between values typically prescribed to open ocean (0.011) and coastal fetch-limited conditions (0.018). Modeled $C_{D\ N10}$ values increase approximately linearly with increasing wind speed and also have a spread which increases as a function of wind speed. This suggests that while coastal modeling efforts will benefit from using a standard wind speed dependent formulation of the drag coefficient, the wave-dependence of wind stress may result in increased variability stemming from fetch-limitation. Furthermore, results suggest that the explicit inclusion of surface waves in wind stress formulations may produce up to a 20% change in wind stress estimates in a fetch-limited environment.

Further research is needed on the influences of physical processes that might contribute to additional variability in the surface wind field and wind stress field over Chesapeake Bay including nearshore shadow zones, wave-current interactions, and air-sea interactions. Additionally, the extent to which the spatial variability of wind stress affects coastal wind-driven circulation and vertical mixing regimes remains poorly understood and would benefit from further research.

§2.6 Acknowledgements

We'd like to acknowledge our collaborators: Bill Boicourt, Carl Friedrichs, Ming Li, and Malcolm Scully. We'd also like to thank the crew of the R/V Hugh R. Sharp for their assistance with the deployment and recovery of oceanographic equipment during multiple cruises. This manuscript benefited greatly from the comments and suggestions of two

anonymous reviewers. This work is supported by National Science Foundation OCE Division of Ocean Sciences grant 1061609. UMCES contribution no. XXXX.

CHAPTER 3

SURFACE WAVE EFFECTS ON THE TRANSLATION OF WIND STRESS ACROSS THE AIR-SEA INTERFACE

Preface

This chapter is a reproduction of work that will appear in the Journal of Physical Oceanography with coauthors Larry Sanford, Malcolm Scully, and Steve Suttles. The right to reuse this work was retained by the authors when publication rights and nonexclusive copyright were granted to the American Meteorological Society.

Fisher A.W., L.P. Sanford, M.E. Scully, and S.E. Suttles (in review): Surface Wave Effects on the Translation of Wind Stress Across the Air-Sea Interface in a Fetch-limited, Coastal Embayment. J. Phys. Oceanogr.

§3.1 Introduction

Surface gravity waves act as dynamic roughness elements at the water surface and play an important role in regulating air-sea momentum and energy fluxes through increased drag at the air-sea interface associated with wave generation (Janssen 1989), energy transfer beneath breaking waves (Craig & Banner 1994, Terray et al 1996), and Langmuir turbulence (Craik & Leibovich 1976, Leibovich 1983). Growing recognition that material exchange in estuaries can be dominated by wind-driven circulation (Sanford & Boicourt 1990, Chen et al 2009, Scully 2010a, Scully 2013) has prompted numerous investigations into the momentum balances of wind-driven flows in estuaries (Geyer 1997, Chen and Sanford 2009, Scully 2010b, Li & Li 2011, Li & Li 2012). Very few of these studies; however, have accounted for surface gravity waves in the energy and momentum budgets of the mean flow. Fetch-limitation in coastal environments often results in wind seas that never reach full saturation, suggesting that the surface wave field may also play an important role in the local air-sea momentum budget in coastal environments.

We present an analysis of the air-sea momentum flux building on the observations of Langmuir turbulence and momentum transfer beneath breaking waves presented in Scully et al (2015) and Scully et al (2016), respectively. Specifically, the focus of this manuscript is to investigate the effects of surface gravity waves in the translation of stress across the air-sea interface. As Scully et al (2016) showed, using the same dataset presented here, direct measurements of the atmospheric surface wind stress and the momentum flux vector observed in the surface layer of the estuary suggest that the local

air-sea momentum budget is not closed. Furthermore, Scully et al (2016) hypothesized that a stress divergence occurs very near the air-sea interface. Using a combination of direct observations and numerical simulations, we investigate the effects of surface gravity waves on the translation of wind stress across the air-sea interface and into the surface layer of the estuary.

§3.2 Background

The evolution of wind stress at the water surface and its subsequent translation into the mixed surface layer is mediated by the presence of surface gravity waves and their interaction with mean and turbulent flows. These effects can be expressed as a modulation of stress at the water surface principally through wind-wave interactions and the modification of vertical mixing regimes through enhanced dissipation (e.g. wave breaking) and/or a restructuring of boundary layer transport through coherent wave-driven turbulence (e.g. Langmuir turbulence).

3.2.1 Wind-Wave Effects in the Atmospheric Surface Boundary Layer

Numerous studies have shown that wind stress measurements exhibit a strong wave dependency in which the aerodynamic drag of young seas is higher than that of mature seas (Kitaigorodskii 1973, Donelan 1982, Geernaert et al 1986, Smith et al 1992, Johnson and Vested 1992, Johnson et al 1998, Komen et al 1998, Oost et al 2002, Drennan et al 2003, Edson et al 2013). Even for old wind seas, the drag is larger than that expected for a smooth plate (Donelan 1982); however, long gravity waves support little

of this wave-induced stress because their phase speed is typically on the same order as the wind speed. Therefore, the aerodynamic drag must primarily be due to the momentum sink associated with the generation of high frequency, short gravity waves (Janssen 1989). The Charnock parameter is used to parameterize this effect by partitioning the roughness parameter into a smooth and rough component due to surface waves (Charnock 1955). This formulation yields an approximately linear relationship between the drag coefficient and wind speed when the Charnock parameter is taken as constant. Numerous studies have accounted for sea state within this parameter by using a wave age (C_p/u_* or C_p/U_{10}) formulation of the drag coefficient or the Charnock parameter (Greernaert et al 1986, Lin et al 2002, Edson et al 2013, Fisher et al 2015). In coastal environments, fetch-limitation can result in high degrees of spatial variability in surface wind stress due to a combination of variable surface winds and waves, which can result in significant spatial and temporal variations in the drag coefficient (Fisher et al 2015).

3.2.2 Stress Partitioning

Partitioning the air-sea momentum flux between the surface wave field and the mean flow may offer insights into the role surface gravity waves play in the local air-sea momentum budget. Independent of direct wind stress, waves can drive significant flows in nearshore environments through gradients in radiation stress (Longuet-Higgins 1970) and mass transport resulting from Stokes drift (Monismith & Fong 2004). The effects of surface gravity waves on the mean flow are commonly examined using radiation stress theory (Longuet-Higgins & Stewart 1960, 1964); however, because radiation stresses are formulated in the momentum balance of a total flow that includes the mean current and

the surface wave field, radiation stress does not describe the partitioning of momentum between the wave field and the mean flow. To investigate the momentum transfer between waves and the mean flow, we partition the air-sea momentum flux following the interaction stress theory developed by Hasselmann (1971).

A full derivation of the horizontal momentum equations that accounts for a complete flow including surface waves is described in Hasselmann (1971) for a nonrotating frame and Ardhuin et al (2004) for a rotating frame. By time-averaging these equations, the interactions of the mean flow with the surface wave field arise from the nonlinear terms and the pressure field. This "interaction stress" tensor is defined as the sum of the Reynolds stress and the wave-induced mean pressure (Hasselmann 1971):

$$\tau_{ij}^{int} = -\rho_w \left(\overline{u_i' u_j'} + p^w \delta_{ij} \right) \qquad (3.1)$$

where ρ_w is the density of seawater, u' is the fluctuating velocity, and p^w is the nonhydrostatic pressure associated with wave motion within a wavy surface layer that exists between the mean and fluctuating component of the free surface, $\zeta(x,y,t)$. Indices i,j refer to Eulerian coordinates x, y, and z. The derivation of Equation (3.1) does not make any assumptions regarding the dynamics of the fluctuating field u', ζ' other than an assumption of the analytical continuation of fields for $\zeta' < 0$ to the mean free surface (Hasselmann 1971). Therefore the interaction stress is a robust term that applies to interactions involving waves and turbulence that are modified by strongly nonlinear processes (Hasselmann 1971, Ardhuin et al 2004).

In the following equations, we adopt the notation of Hasselmann (1971) in which dummy indices α,β correspond to horizontal components. Separation of the momentum flux between waves and the mean flow can be examined by partitioning the vertically integrated momentum (*M*) balance between the mean flow (superscript m) and a wavy surface layer (superscript w) constrained between the mean free surface and the instantaneous free surface:

$$\overline{M_\alpha} = \rho_w \overline{\int_{-h}^{\zeta} u_\alpha \, dz} = \rho_w \overline{\int_{-h}^{\bar{\zeta}} u_\alpha \, dz} + \rho_w \overline{\int_{\bar{\zeta}}^{\bar{\zeta}+\zeta'} u_\alpha \, dz} = \overline{M_\alpha^m} + \overline{M_\alpha^w} \quad (3.2)$$

where h is depth and u is velocity. Overbars denote averages over several wave periods. Furthermore, we note that wave energy spectral density can be used in the formulation of wave momentum (Ardhuin et al 2004):

$$\overline{M^w} = \rho_w g \int \frac{kF(k)}{|k| C} dk \quad (3.3)$$

where F(k) is the wave energy spectral density as a function of the wavenumber vector (k) and C is the wave phase speed.

The evolution of the depth-integrated, time-averaged momentum of the horizontal α component of the total flow can be expressed as (Ardhuin et al 2004):

$$\frac{\partial \overline{M_\alpha}}{\partial t} = \left[\frac{\partial T^m_{\alpha\beta}}{\partial x_\beta} + \overline{p^a} \frac{\partial \bar{\zeta}}{\partial x_\alpha} + \left(p^m + gh \right)_{-h} \frac{\partial h}{\partial x_\alpha} + fM^m_\beta \left(1 - \delta_{\alpha\beta} \right) + \tau^{air}_\alpha - \tau^{bot}_\alpha \right] + \frac{\partial T^{rad}_{\alpha\beta}}{\partial x_\beta} + p^w_{-h} \frac{\partial h}{\partial x_\alpha} + fM^w_\beta \left(1 - \delta_{\alpha\beta} \right) \tag{3.4}$$

where the terms on the RHS are: (ii) horizontal divergence of depth-integrated total mean stress; (iii) pressure gradient force; (iv) mean bottom pressure including hydrostatic pressure; (v) coriolis force of mean flow; and the (vi) surface and (vii) bottom shear stresses. The eighth term (viii) is the horizontal divergence of radiation stress tensor and the nineth (ix) and tenth (x) terms are the wave-added pressure term and the wave-added coriolis force, respectively. Note that τ represents true stresses (N/m^2), whereas T terms represent depth-integrated stresses that have units of total force per unit width (N/m). The overall momentum equation is the result of depth-integrating the equations of motion and averaging over several wave periods, evoking appropriate boundary conditions.

Integrating the equations of motion from z = -h to $\bar{\zeta}$ yields the mean flow momentum equation (Ardhuin et al (2004) Eqn 15,16):

$$\frac{\partial \overline{M^m_\alpha}}{\partial t} = \left[\frac{\partial T^m_{\alpha\beta}}{\partial x_\beta} + \overline{p^a} \frac{\partial \bar{\zeta}}{\partial x_\alpha} + \left(p^m + gh \right)_{-h} \frac{\partial h}{\partial x_\alpha} + fM^m_\beta \left(1 - \delta_{\alpha\beta} \right) + \tau^{air}_\alpha - \tau^{bot}_\alpha \right] + \frac{\partial T^{int}_{\alpha\beta}}{\partial x_\beta} + \left(\tau^{int}_\alpha - \tau^{air}_\alpha \right) + p^w_{-h} \frac{\partial h}{\partial x_\alpha} + fM^w_\beta \left(1 - \delta_{\alpha\beta} \right) \tag{3.5}$$

The bracketed terms on the right hand side of the equation are the usual terms in the horizontal momentum equation of the mean flow including the effects of rotation. The seventh term is the horizontal divergence of the interaction force.

$$T_{\alpha\beta}^{int} = \int_{-h}^{\bar{\zeta}} \tau_{\alpha\beta}^{int} dz \qquad (3.6)$$

It is informative to explore the wave contributions to the depth-integrated interaction stress tensor in Equation (3.6) by assuming a quasi-linear wave field. Using this simplified approach, Ardhuin et al (2004) showed that the wave-component of the depth-integrated interaction stress can be expressed as:

$$T_{\alpha\beta}^{int} = \rho_w g \int F(k) \left[\left(1 - \frac{C_g(k)}{C(k)} \right) \delta_{\alpha\beta} - \frac{C_g(k)}{C(k)} \frac{k_\alpha k_\beta}{k^2} \right] dk \qquad (3.7)$$

where C_g is the group speed. Thus, the depth-integrated wave-component of the interaction stress is equal to the depth-integrated pressure added by surface waves (term 1 in brackets) and the nonisotropic wave momentum advected by waves (term 2 in brackets) (Ardhuin et al 2004).

The difference τ^{int} between and τ^{air} represents the portion of the air-sea momentum flux that is stored in (negative) or released by (positive) the surface wave field to the mean flow (Ardhuin et al 2004). For wind and waves that are aligned, this fraction decreases as a function of wave age from roughly 10% for very young seas to

near zero for a mature wind sea (Ardhuin et al 2004) consistent with the findings of Mitsuyasu (1985). Analysis of momentum storage in a misaligned wave field, however, has not been addressed in the literature to our knowledge.

The momentum evolution equation of the wave surface layer can be determined by subtracting Equation (3.5) from Equation (3.4):

$$\frac{\partial M_{\alpha}^{w}}{\partial t} - \nabla \bullet T_{\alpha\beta}^{sl} = \tau_{\alpha}^{air} - \tau_{\alpha}^{\text{int}} \tag{3.8}$$

where $T_{\alpha\beta}^{sl}$ is the depth-integrated stress acting on the wavy surface layer defined as:

$$T_{\alpha\beta}^{sl} = -\overline{\int_{\bar{\zeta}}^{\bar{\zeta}+\zeta'} \left(p\delta_{\alpha\beta} + \rho_w u_{\alpha}' u_{\beta}' \right) dx_3} \tag{3.9}$$

A conceptual diagram illustrating the partitioning of the momentum budget between the mean flow and the surface wave field is shown in Figure 3.1. The interaction stress represents the shear stress acting on the mean flow, or the shear stress acting at the mean free surface. The radiation stress, therefore, can be expressed as the sum of the average stress acting on the wavy surface layer and the interaction stress.

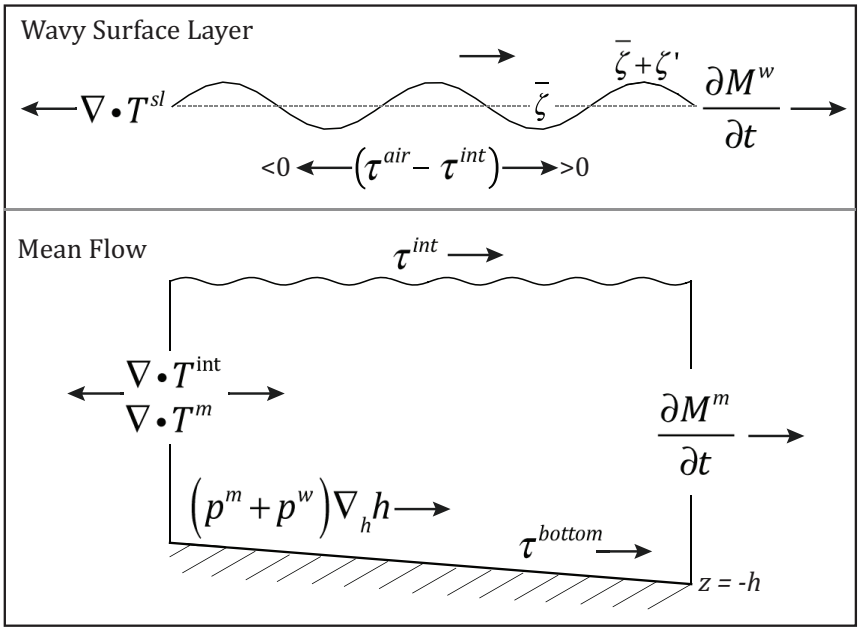

Figure 3.1 Conceptual diagram of partitioning the air-sea momentum flux between the surface wave field and the mean flow using interaction stress theory. The wave momentum is contained in a wavy surface layer between the mean free surface ($\bar{\zeta}$) and the instantaneous free surface ($\bar{\zeta}+\zeta'$). The fraction of momentum stored in or released by the surface wave field can be expressed as the difference between the wind stress and the interaction stress. The interaction stress then represents the surface shear stress acting on a mean flow that accounts for the effects of a wavy free surface. A similar diagram is shown in Ardhuin et al (2004).

3.2.3 Wave-Enhanced Turbulent Mixing

The effects of surface gravity waves on mixing and material transport within the water column can take many forms and usually result in an enhancement of vertical exchange relative to wall-bounded shear flows. Focusing on the ocean surface mixed layer, we will restrict our discussion to whitecapping dissipation, mixing due to breaking waves (Scully et al 2016), and Langmuir turbulence (Scully et al 2015). Wave breaking and Langmuir turbulence are strongly coupled, so the distinction between the two

processes may not be informative or meaningful in a shallow estuarine environment where coherent cells are modified by tidal shear, strong vertical density gradients, and bottom boundary layer dynamics. For simplicity, we refer to the sum of the latter two terms as wave-controlled coherent turbulence.

Wave breaking is a primary mechanism through which mechanical energy and momentum are transferred from the atmosphere to the mean flow (Melville 1996). Rapp and Melville (1990) suggested that the momentum flux associated with breaking waves constitutes a majority of the air-sea flux. Wave breaking in deep water is the result of wind-wave, wave-wave, and wave-current interactions (Melville 1996). Measured distributions of breaking rate show a peak at a phase speed approximately half that of the spectral peak with dissipation of high frequency, short-waves comprising a significant fraction of the total breaking rate (Gemmrich et al 2008, Thomson et al 2009, Schwendeman et al 2015). Schwendeman et al (2015) also noted that a regime shift occurs in young wind seas where large whitecaps replace, not add to, small-scale breakers as forcing becomes stronger. Furthermore, field observations of the dissipation of turbulent kinetic energy beneath surface gravity waves exceeds wall-bounded shear flow scaling (Kitaigorodskii et al 1983, Agrawal et al 1992, Drennan et al 1992, Terray et al 1996, Drennan et al 1996, Gemmrich & Farmer 1999, Gemmrich 2010, Scully et al 2016).

Coherent wave-driven turbulence can enhance the transport of momentum and energy beneath breaking waves into the oceanic surface layer through a combination of u-shaped vortices generated near the surface by whitecapping waves (Melville et al 2002, Scully et al 2016) and larger-scale Langmuir circulations which can occupy the full depth

of the surface mixed layer (Plueddemann and Weller 1999, D'Asaro 2001, Gerbi et al 2008, Scully et al 2015). It is generally accepted that Langmuir turbulence arises from a straining of the vorticity field generated beneath breaking waves by Stokes drift (Craik 1977, Leibovich 1977) and can significantly increase turbulent length and velocity scales relative to a wall-bounded shear flow (McWilliams et al 1997, Li et al 2005, Harcourt & D'Asaro 2008). Additionally, wave-controlled coherent turbulence may play an important role in entrainment at the base of the surface mixed layer directly or indirectly by enhancing Kelvin-Helmholtz billowing through a concentration of shear near the pycnocline (Li & Garrett 1997, Kukulka et al 2010).

§3.3 Methods

The centerpiece of a field deployment that included instrumented surface buoys, bottom landers, and towed-instrument surveys was a turbulence tower deployed on a western shoal of the middle reaches of Chesapeake Bay (38 27' 39", 76 24' 44") in a 14 m deep region of slowly-varying bathymetry. It was held vertically rigid using four guy-wires, which were secured to the top of the 16 m tower and anchored to 1000 lb railcar wheels. The tower was deployed on September 18, 2013 and recovered on October 29, 2013. A schematic of the tower and map of the deployment site are shown in Figure 3.2.

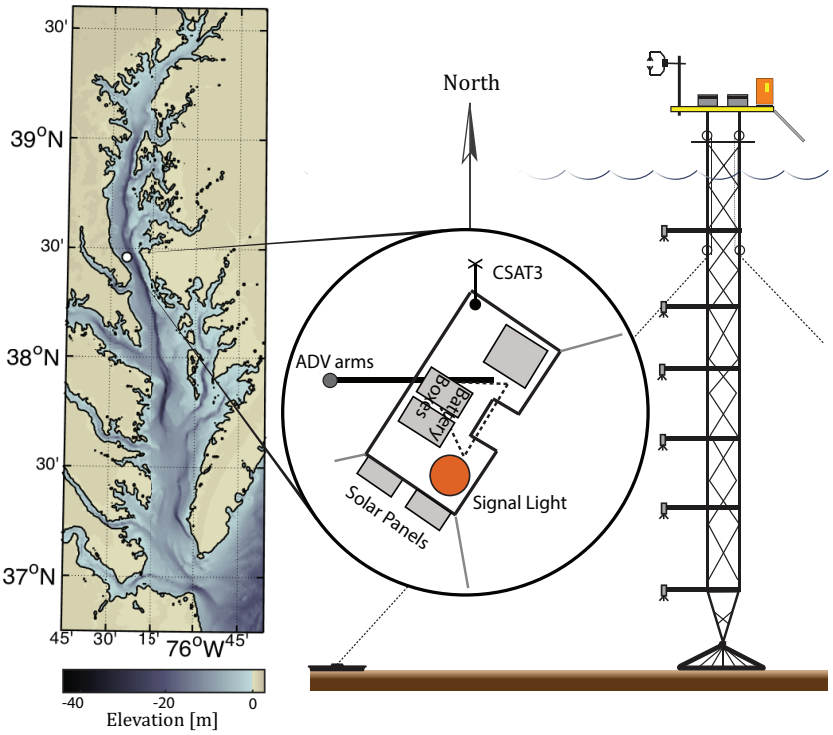

Figure 3.2 Map and tower schematic. Inset diagram shows the orientation of the tower, ultrasonic anemometer, and ADVs. Tower schematic at right shows vertical array structure.

High-resolution velocity data used in the estimation of momentum fluxes was recorded using a vertical array of Nortek Vector Acoustic Doppler Velocimeters (ADVs) in the water column and an ultrasonic anemometer deployed on an aerial platform atop the tower. The downward-looking ADV heads were mounted to 1 m aluminum arms attached to the tower ~2 m apart in the vertical, starting approximately 1.5 m below the mean water surface. The aluminum arms were oriented due west. The ADVs recorded three-dimensional velocity and pressure data at 32 Hz in 28-minute bursts centered 30 minutes apart.

Direct measurements of air-sea momentum and sensible heat fluxes were collected by a Campbell Scientific CSAT3 ultrasonic anemometer with fine-wire thermocouple deployed on top of the tower. The anemometer was oriented due North and

had a sampling volume elevation of ~2.82 m above MSL. The tidal range at the tower site was approximately 0.5 m, so the elevation of the anemometer ranged from ~2.3 m to ~3.3 m above the water surface. The system sampled the 3D velocity field and air temperature at 10 Hz continuously. The anemometer was deployed on September 25, 2013 and recovered on October 28, 2013.

3.3.1 Data Analysis

The analysis period was constrained to three weeks spanning September 25, 2013 to October 18, 2013 due to the exhaustion of ADV batteries at the end of the deployment. Additionally, periods of tower-induced flow distortion were omitted when the mean current was coming from 70° to 130° TN and when the winds blew from 170° to 250° TN.

Directional wave spectra were calculated from the uppermost ADV data (z = -1.7 m) using the PUV (pressure and horizontal velocity) method based on linear wavy theory and the DIWASP Matlab toolkit (Johnson 2002). The 32 Hz pressure and 3D velocity data from the ADV were resampled at 8 Hz and a 1024 s segment of each burst, starting with the ninth sample in the resampled burst, was used for each wave burst. Additionally, the pressure signal was corrected for variations in atmospheric pressure using barometric pressure data from the Cove Point NOS station (~6.9 km SE of tower site), and low-pass filtered using a second-order butterworth filter with a 1 Hz cutoff. The total energy level in each frequency was set using the corrected pressure signal. An f^{-4} tail was fit to observational spectra due to an inability of resolving wave frequencies above 0.6 Hz due to the depth of the pressure sensor (Jones & Monismith 2007). Doppler shifting by the

mean currents was accounted for by adjusting the frequency vector of observed wave spectra using linear wave theory.

A summary of tower conditions observed during the deployment is presented in Figure 3.3. The deployment was dominated by a 10-day Nor'easter that was recorded between October 6 and October 16, 2013. The event was characterized by winds blowing from NE to N at an average wind speed of 7 m/s. Wind stress peaked at 0.31 Pa, with an event average of 0.13 Pa. The event generated a surface wave field that had a significant wave height of ~1 m and typical peak wave period of 4 seconds. Tidal velocities were aligned with the central channel at 150° TN. Note that wave direction and period data for times when significant wave heights fell below 10 cm are spurious due to the depth of the pressure sensor.

Turbulent fluxes were calculated using velocity cospectra from the sonic anemometer and the vertical array of ADVs. Atmospheric measurements of wind stress were calculated by integrating velocity cospectra for frequencies less than 2 Hz in 30-minute blocks (Reider et al 1994). A 30-minute window should provide a sufficient range of sampling scales to properly represent turbulence in the near-surface atmosphere (Drennan et al 2003). The sensitivity of vertical flux measurements to variations in sensor orientation prompted a tilt correction using the planar fit method (Wilczak et al 2001) on daily subranges of the anemometer data as described in Fisher et al (2015). To avoid artificial enhancement of stress estimates from correlated wave orbital velocities, the integration of ADV burst velocity cospectra was limited to frequencies less than 0.1 Hz, below the wave band. Scully et al (2015,2016) analyzed the same data presented here and

showed that low-frequency motions, below the wave band, dominate the Reynolds stress tensor.

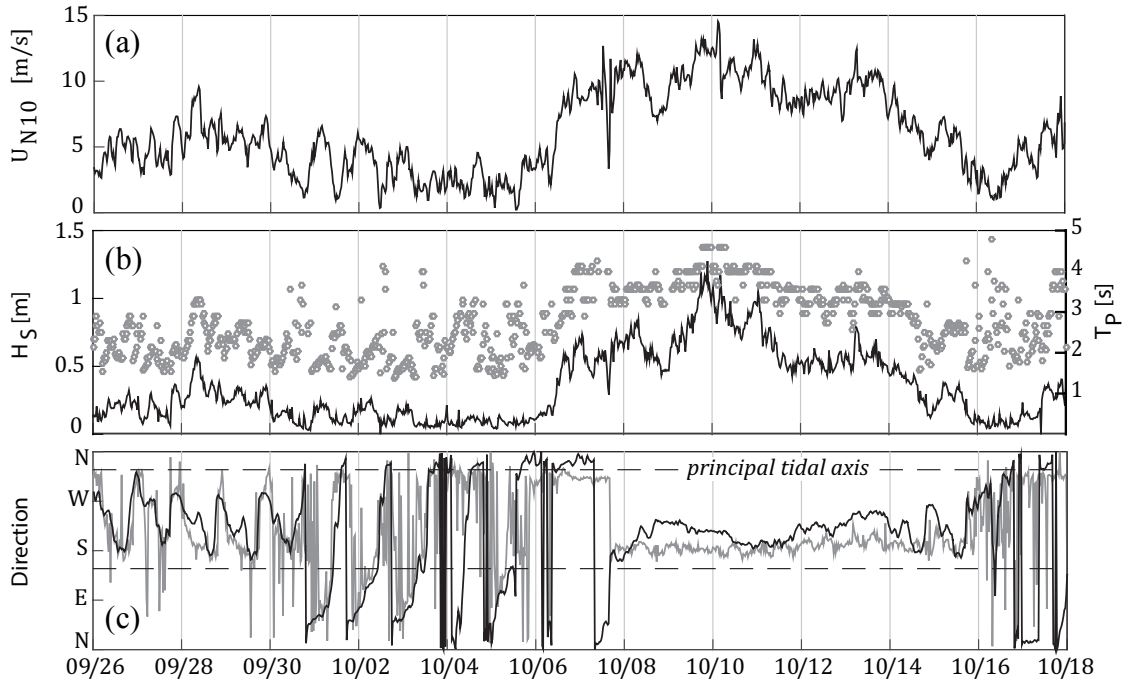

Figure 3.3 Wind and wave conditions at tower during the deployment. (a) Ten-meter neutral wind speed. (b) Significant wave height (black) and peak period (grey dots). (c) Wind (black) and wave (grey) direction in oceanographic convention. The principal tidal axis is also shown as dashed black lines.

3.3.2 Simulating the Surface Wave Energy Budget

A third generation numerical wave model, Simulating WAves Nearshore (SWAN version 40.91, Booij et al 1996), was used to examine the wave energy budget at the tower site. The nonstationary model solves the spectral action density equation on a 5-minute computational time step:

$$\frac{\partial N}{\partial t}+\nabla\bullet\left[\left(\overrightarrow{C_g}+\vec{U}\right)N\right]+\frac{\partial c_\sigma N}{\partial\sigma}+\frac{\partial c_\theta N}{\partial\theta}=\frac{1}{\sigma}\left(S_{wind}+S_{wcap}+S_{bot}+S_{nl3}+S_{nl4}\right) \quad (3.10)$$

where N is action density (F/σ), C_g and U are group velocity and barotropic current velocity respectively, σ is angular frequency, θ is direction, and S denotes source terms. The first term on the left-hand side is the time rate of change of action density, the second term is the geographic divergence of wave energy transport, and the next two terms are associated with the divergence of wave energy in wavenumber space due to frequency shifting (term 3) and refraction/diffraction (term 4). The source terms represent the sum of wind energy input (S_{wind}), whitecapping dissipation (S_{wcap}), bottom-induced frictional dissipation (S_{bot}) and nonlinear wave-wave interactions associated with triads (S_{nl3}) and quadruplets (S_{nl4}).

The model was setup as described in Fisher et al (2015). Wind wave generation was forced by an optimally interpolated 10-meter neutral wind field generated from over 60 surface stations in and around Chesapeake Bay. Over-land stations were corrected to 10-meter neutral conditions using a standard power law (Panofsky & Dutton 1984) and over-water stations were adjusted using the COARE 3.0 algorithm (Fairall et al 2003). A universal kriging scheme with algorithmically-fit exponential variogram was applied to the vector components of the 10-meter neutral wind field on a 30 minute timestep. Wave growth was formulated using the Zijlema et al (2012) expression for the drag coefficient in combination with the Komen et al (1984) expression for exponential wave growth. The model accounted for tidal elevation interpolated from nine tide gauges around the Chesapeake Bay and bottom friction was estimated through the empirical JONSWAP model (Hasselmann et al 1973). Barotropic currents were not included in the model.

§3.4 Results

An important feature of the surface conditions observed during the deployment was that wind and waves were consistently misaligned during the 10-day Nor'easter wind event. During the event, the dominant waves were aligned roughly 17° to the left of the wind (Figure 3.3, panel c). Model results accurately simulate measured significant wave height, period, and direction as shown in Figure 3.4. The model slightly overpredicts the directional spread of wave energy, but accurately captures the mean direction and the asymmetry observed in the high frequency portion of the directional wave spectra measured by the uppermost ADV.

Plotting directional wave data in wavenumber space reveals that wave directions measured in the mid-Bay bifurcate along two dominant directions: waves propagating down-estuary generally move south while waves propagating up-estuary align ~330 TN (Figure 3.5). Wavenumbers are calculated using the peak period and peak wave direction from directional spectra. The blue line shows log-transformed fetch (scaled to fit) as a function of direction. Fetch was calculated as the upwind distance to shore using elevation data used in the SWAN wave model. As waves mature (wave age increases), they concentrate on two principal directions that correspond to the direction of maximum upwind fetch. This behavior is consistent with the slanting fetch observations presented by Donelan et al (1985) and Ardhuin et al (2007). Observed waves were predominantly deep-water waves with only a brief period when λ was slightly greater than twice the water depth, so depth-induced refraction was not a significant factor in the misalignment

between wind and waves. Rather, the misalignment between wind and waves is the result of preferential wave growth along the dominant fetch axes of the embayment.

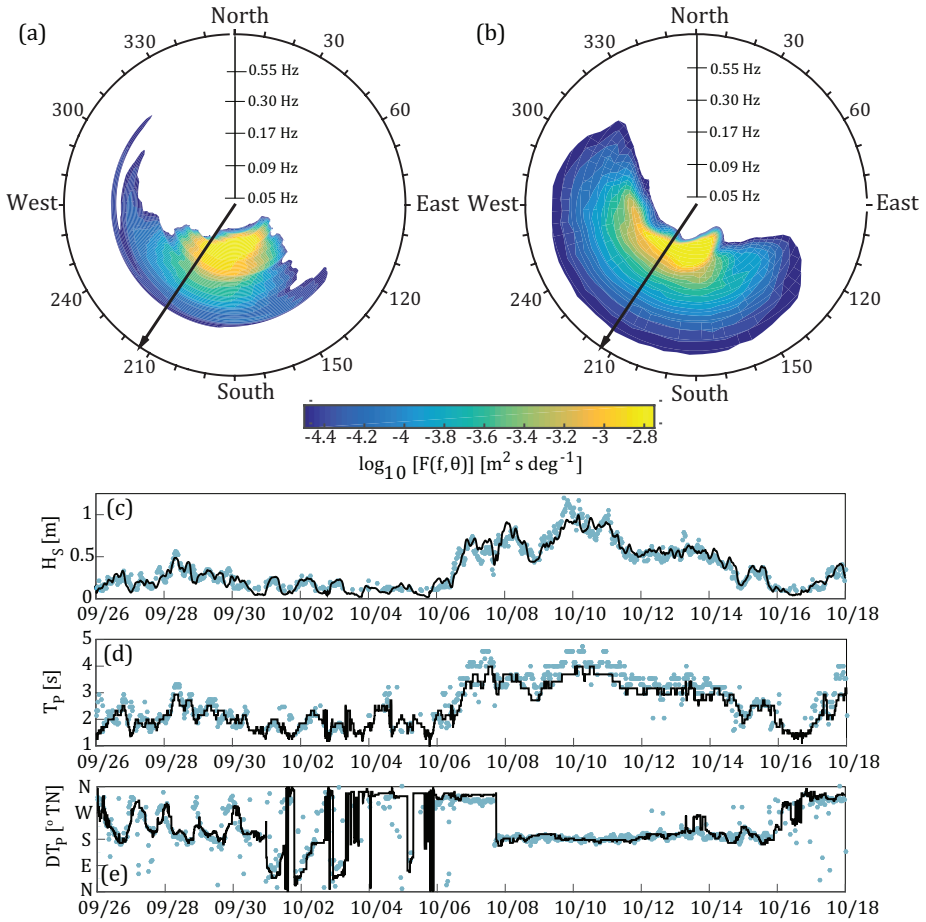

Figure 3.4 Model Validation. (a) Observed directional wave spectra at tower on October 10, 2013 10:30 EST with wind direction shown as a black vector. (b) Modeled spectra for same time period. SWAN captures the peak characteristics of the spectra, but slightly overpredicts directional spreading. Observed (blue) and simulated (black) significant wave height, peak period, and peak direction are shown in panels (c-e) respectively.

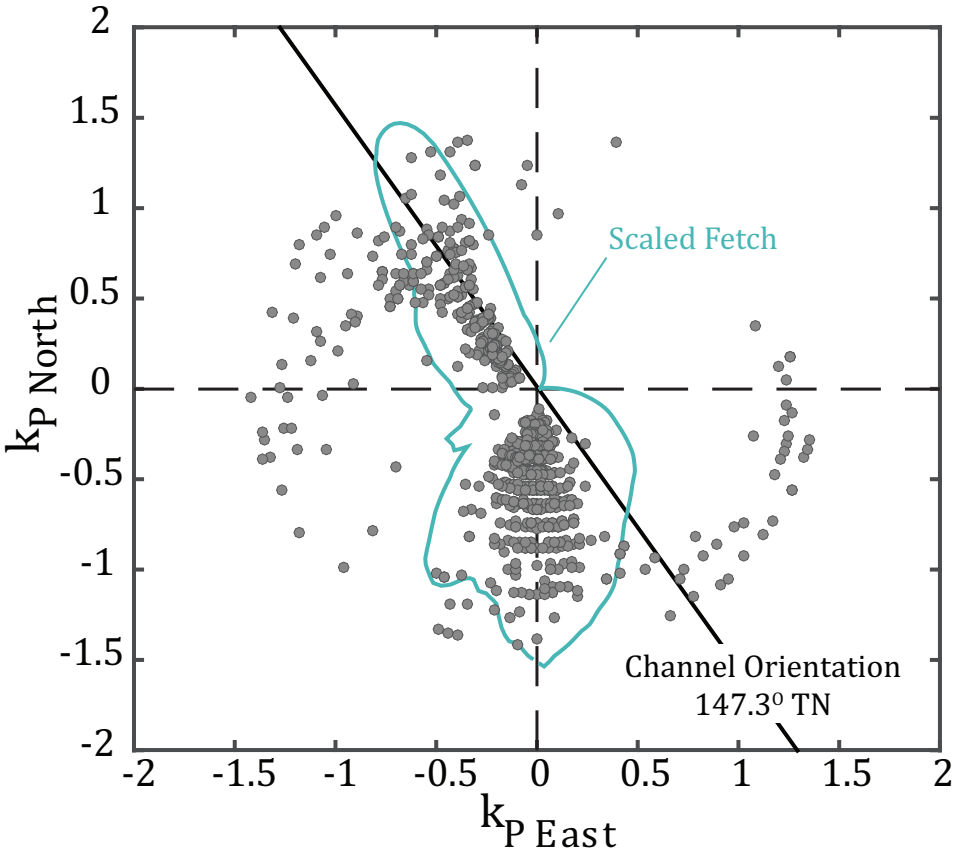

Figure 3.5 Tower wave data plotted in wavenumber space where $k_{p\ east}$ and $k_{p\ north}$ are the wavenumber vector components at the spectral peak. The blue line is a contour of log-transformed fetch scaled to fit. The channel orientation at the tower site is shown as a solid black line.

Analysis of SWAN model output for the tower site shows that the dominant terms in the wave energy budget are wind input, whitecapping dissipation, and the horizontal divergence of wave energy transport. The sum of whitecapping dissipation and the divergence of wave energy transport balance wind input to first order (Figure 3.6). This suggests that spatial gradients developed principally through directionally variable fetch-limitation can result in a significant divergence of wave energy transport, which may play an important role in the local air-sea momentum budget.

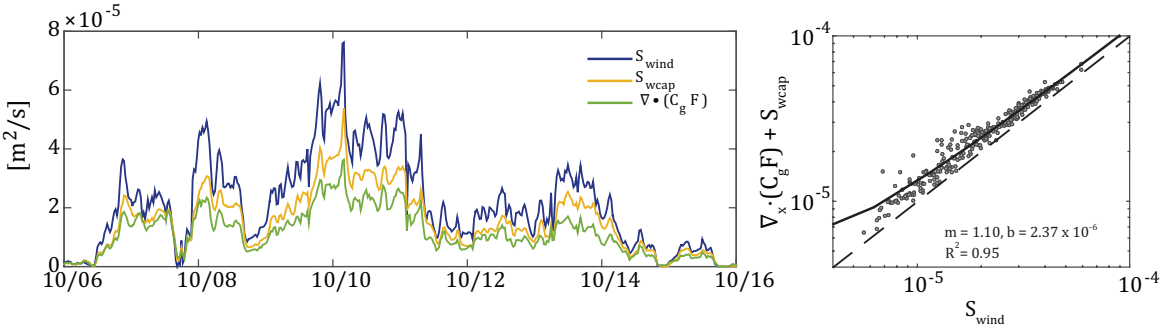

Figure 3.6 (a) Time series of simulated wind energy input (blue), whitecapping dissipation (yellow), and geographic divergence of wave energy transport (green). (b) Simulated wave energy budget at the tower site. Whitecapping dissipation and the horizontal divergence of wave energy transport balance wind input to first order.

As discussed in Scully et al (2016), the direction of the momentum flux vector changed across the air-sea interface. Direct measurements from the ultrasonic anemometer show that the stress in air is aligned with mean wind direction, with an average departure angle of 2.2±1.2° to the left of the wind. In contrast, the stress at the uppermost ADV (z = -1.7 m depth) is more aligned with wave forcing than wind forcing with a mean departure angle of 16.07 ± 1.8° to the left of the wind. These results are consistent among the top four ADVs, suggesting that the momentum flux vector in the

surface layer of the estuary is misaligned with local wind forcing and may be controlled by the surface wave field. However, the temporal variation of the stress direction measured by the uppermost ADV significantly exceeds the temporal variability of the dominant wave direction, which generally concentrates on 180° during the 10-day Nor'easter.

Figure 3.7a shows the distributions of departure angles, counterclockwise relative to wind forcing, of the momentum flux vector measured in air (θ_{air}), the momentum flux vector measured in water ($\theta_{z=-1.7m}$), and peak wave direction (θ_{waves}). Figure 3.7b shows a mean vector stress profile averaged over the same period, which shows that the directional divergence of the momentum flux vector at the air-sea interface is counterclockwise. Conversely, a clear clockwise rotation is present in the vertical stress profile of the surface layer of the estuary. The width of the mid-Bay is the same order as the internal Rossby radius, so this clockwise rotation is likely indicative of Ekman steering within the well-mixed surface layer.

During the wind event, persistent near-bottom stratification was present for depths greater than ~10m and limited the vertical extent of the bottom boundary layer (Scully et al 2015). The stress direction within this bottom boundary layer, measured by the lowest tower ADV (z = - 11.5m) and a co-located bottom lander, was tidally-dominated and is not shown in the Figure 3.7b. However, the principal tidal axis is denoted in Figure 3.7b as a black line.

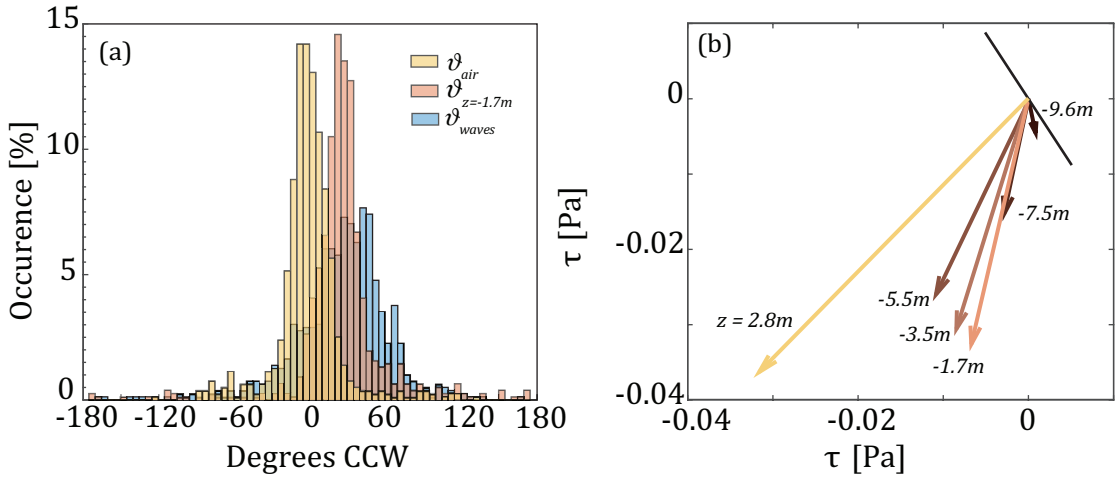

Figure 3.7 (a) Distributions of the departure angle of the momentum flux vector measured in air (ϑ_{air} , yellow) and at z= -1.7m ($\vartheta_{z=-1.7m}$, red) from mean local wind direction measured degrees CCW. The distribution of the angle between wind and waves at the tower site is also shown (ϑ_{waves} , blue). (b) Average momentum flux vectors showing the departure of the marine stress profile from the atmospheric surface stress. Black line denotes principal tidal axis.

Several studies have shown that swell can affect the direction of wind stress in the atmospheric surface boundary layer (Reider et al 1994, Drennan et al 1999, Potter et al 2015). However, the upper Chesapeake Bay is characterized as a pure wind sea environment, such that wave energy in the upper Bay is entirely generated by local winds, with any incoming ocean swell dissipating to negligible energy levels by the time it reaches the mid-Bay (Lin et al 2002). Phillips (1985) hypothesized that a portion of the wind sea spectrum would be in equilibrium with wind forcing, such that the source terms in Equation (3.10) would sum to zero. This "equilibrium range" occurs well above the peak frequency in the wave subrange that supports the majority of the atmospheric wind stress. Following Banner (1990), we define the equilibrium subrange as $f > 2f_p$.

The shear velocity required to maintain equilibrium can be described using the following relation (Thomson et al 2013):

$$u_{eq} = \left(\frac{1}{f_{\max} - 2f_p} \right) \int_{2f_p}^{f_{\max}} 8\pi^3 f^4 F(f)\, df \qquad (3.11)$$

where f_p is the peak frequency and f_{max} is the highest observed/modeled frequency. We calculated this equilibrium shear velocity from observational spectra truncated at 0.6Hz, averaged over the equilibrium range, and compared the results to shear velocities measured by the sonic anemometer. Bin-averaged results for the 10-day storm event are shown in Figure 3.8. For small to moderate stress values, the strong 1:1 correlation of the equilibrium shear velocity and the measured shear velocity indicates that the wave field is in equilibrium with the wind. At large measured stress values, however, the shear velocity measured by the sonic anemometer is higher than the equilibrium shear velocity calculated from wave spectra. This indicates that the surface wave field is not in equilibrium with the wind and that short gravity waves are in an active state of growth towards equilibrium. The threshold behavior shown in the comparison of the equilibrium shear velocity and the measured shear velocity could be the result of bounded wave growth due to fetch-limitation. Because the peak frequency is limited by fetch, the equilibrium shear velocity calculated from Equation (3.11) is therefore also limited, resulting in large wind events producing very young seas that never fully saturate.

Additionally, simulated wave spectra were used to calculate the average wave direction as a function of frequency, for times when the mean wind direction and wave directions were aligned and misaligned. Figure 3.9 shows that misalignment between wave direction and wind direction is predominantly a characteristic of wave frequencies

at or below the peak, with the quasi-equilibrium range being aligned with wind forcing. Modeled results were used in Figure 3.9 instead of observational spectra to present qualitative spectral structure that included frequencies above 0.6 Hz. Observational spectra showed a similar qualitative structure, but the average direction within the equilibrium subrange was significantly noisier than that calculated from simulated spectra.

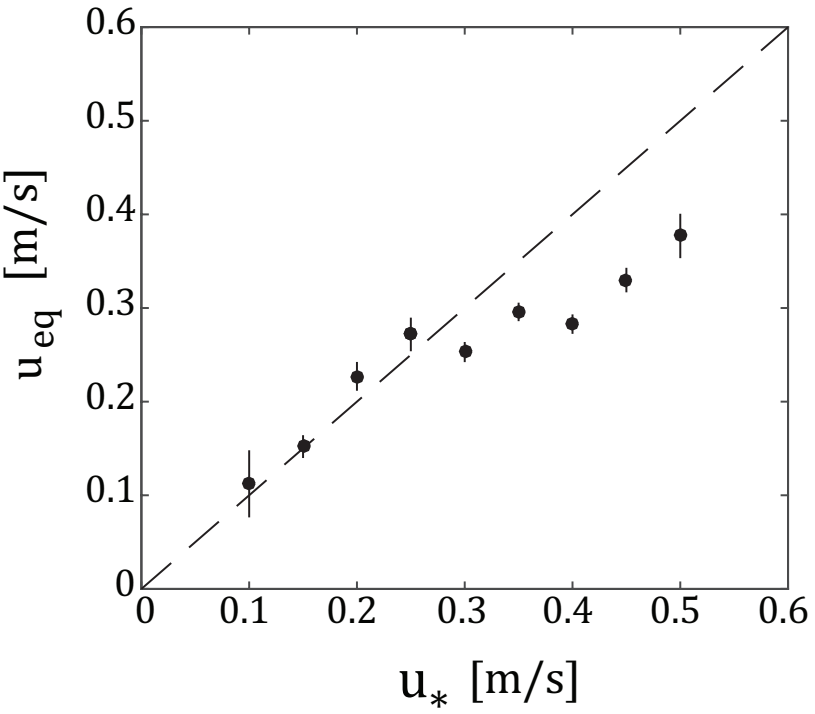

Figure 3.8 Bin-averaged comparison of equilibrium shear velocity calculated from observational wave spectra to measured wind shear velocity shown with standard error bars. Equilibrium shear velocity values were calculated as the average of Equation (3.11) over the equilibrium subrange of wave spectra ($f>2f_p$).

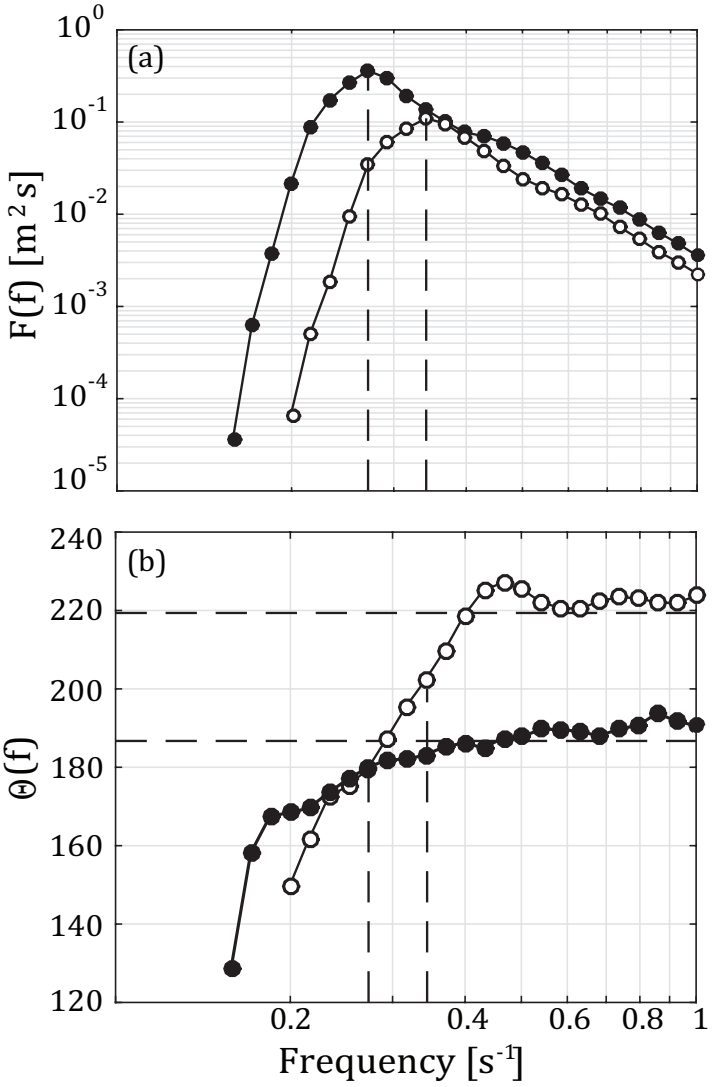

Figure 3.9 (a) Modeled wave energy spectra for a period when wind and waves were aligned (black dots) and when they were misaligned (white dots). Peak frequency shown as a dashed line. (b) Average wave direction as a function of frequency for the same periods. Horizontal dashed lines indicate wind direction.

Using interaction stress theory, we used measured wind stress and modeled terms in the wave energy budget to approximate the fraction of the momentum flux stored in (or released by) the surface wave field following Ardhuin et al (2004):

$$\tau_{\alpha}^{air} - \tau_{\alpha}^{int} = \int \left[\left(S_{wind} + S_{wcap} + S_{nl} \right) \frac{k_{\alpha}}{kC} - \frac{C_{k,\beta}}{C} \left(\frac{\partial F}{\partial k_{\beta}} \right) \right] + \frac{\partial}{\partial x_{\beta}} \left[F \left(\frac{1}{2} - \frac{C_g k_{\alpha} k_{\beta}}{Ck^2} \right) \right] dk \tag{3.12}$$

derived by dividing Equation (3.11) by the phase speed and integrating over the wavenumber vector, k. Note that the above equation is equivalent to Equation (3.8), where the last term on the right-hand side is the divergence of a depth-averaged wave-induced stress in the wavy surface layer due to the dynamic pressure associated with a fluctuating instantaneous free surface and the wave-component of the Reynolds stress. Because our model results indicate that refraction and frequency shifting effects due to depth variations are very small relative to other terms in the wave energy budget, we neglect the second term in the first pair of brackets in Equation (3.12).

Before proceeding with an analysis of the interaction stress, we note that our modeled interaction stress was significantly higher than the atmospheric stress at the onset of the 10-day Nor'easter event, which is likely due to an overprediction of high frequency wave energy during that period. A sheltering effect is expected for winds blowing out of the south-southwest due to a 30 m topographic feature, Calvert Cliffs. The Cliffs likely created an internal boundary adjustment that reduced surface atmospheric stress 1-2 km away from the shoreline (Markfort et al 2010). For this reason, we omit the period between October 6, 10:00 EST to October 8, 00:00 EST from further analysis.

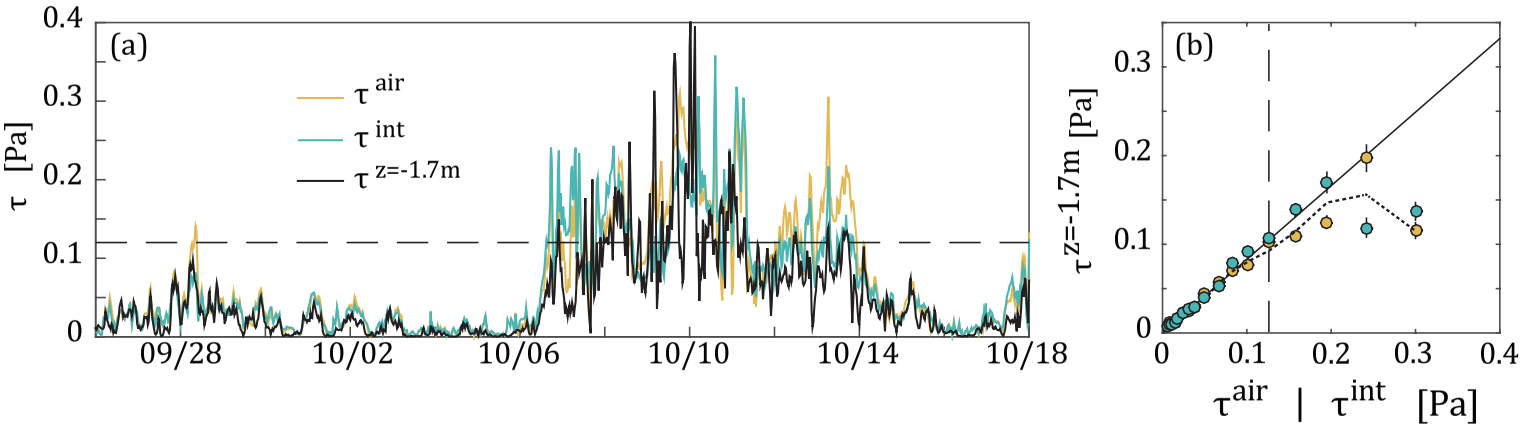

Figure 3.10 (a) Time series of atmospheric stress measured by the ultrasonic anemometer (τ^{air}), interaction stress (τ^{int}), and stress measured at the uppermost ADV ($\tau^{z=-1.7m}$). (b) Bin-averaged comparison of the interaction stress (blue) and the total atmospheric stress (yellow) to the stress at z = -1.7 m shown with standard error bars. The trend line calculated using a moving-window average of binned atmospheric stress is shown as a yellow dotted line. The solid line represents surface layer scaling (Eqn 3.13). The horizontal dashed line at 0.12 Pa in (a) corresponds to the vertical dashed line in (b), and represents the point above which $\tau^{air}\left(1-\left|z\right|/h\right)>\tau\left(z\right)$.

Using the measured atmospheric stress from the ultrasonic anemometer, we examine the air-sea momentum budget across the air-sea interface by comparing the magnitudes of the atmospheric stress (τ^{air}), interaction stress (τ^{int}), and the stress measured at the uppermost ADV at z = -1.7 m ($\tau^{z=-1.7m}$). In Figure 3.10b, a bin-averaged comparison of the stress measured in the surface layer of the estuary versus the interaction stress and the atmospheric stress is shown for all times when the atmospheric shear velocity exceeded 0.103 m/s (~0.013 Pa). The dashed yellow line in panel (b) represents binned atmospheric stress data using moving averaging window. The solid line in panel (b) indicates a linear surface layer stress scaling for a wall-bounded shear flow based on the depth of the mixed surface layer (~10 m):

$$\tau^z = \tau^0 \left(1 - \frac{|z|}{h} \right) \qquad (3.13)$$

where τ^0 is the stress at the mean free surface and h is the height of the boundary layer. This scaling of stress has been demonstrated to hold for the outer log layer and assumes a balance between shear production and dissipation (Tennekes & Lumley 1972). Turbulent kinetic energetics beneath breaking waves differ from those in a neutral log layer and are often described as a balance between divergent TKE transport and dissipation (Terray et al 1996). However, the LES results of Sullivan et al (2007) show a similar linear distribution of stress beneath energetic wave breaking and, as Scully et al (2016) also showed, a surface layer scaling of stress accurately represents our observations of stress within the oceanic surface boundary layer during periods of active wave forcing.

A time series of the total atmospheric stress, interaction stress, and stress at z = -1.7 m is also shown in Figure 3.10a. The horizontal dashed line in panel (a) indicates conditions when the atmospheric stress magnitude exceeds what is expected at z = -1.7 m given surface layer scaling and corresponds to the vertical dashed line in panel (b). Effectively, the threshold shown as dashed lines in panels (a) and (b) represents that point at which the total wind stress exceeds the stress that can be translated through the wave field to the mean flow, which is determined by fetch-limitation at the tower site (a similar behavior to the that shown in Figure 3.8. Results presented in Figure 3.10 suggest that: (1) the interaction stress properly accounts for changes in magnitude between the atmospheric stress and the stress measured by the uppermost ADV and (2) a significant portion of the atmospheric stress vector is not translated to a momentum flux within the surface layer of the estuary during moderate to large stress events.

It is of interest to examine how the fraction of stress stored in or released by the surface wave field varies over the deployment. Figure 3.11 shows a time series of the difference between (1) the atmospheric stress scaled to the depth of the ADV using the surface layer stress scaling shown in Figure 3.10 and the stress measurements at z ~ -1.7 m; and (2) the atmospheric stress and the interaction stress. The agreement between the two time series, particularly between 10/12 and 10/15, indicates that the surface wave field stored and released a significant fraction of the total air-sea momentum flux. Towards the end of the Nor'easter, October 11-15, the wind was blowing primarily out of the northeast and the stress measured at the uppermost ADV was only ~60% of that measured by sonic anemometer. Our results thus indicate that the momentum

storage/release in the surface wave field can be as high as 40% of the wind stress measured in the atmospheric boundary layer.

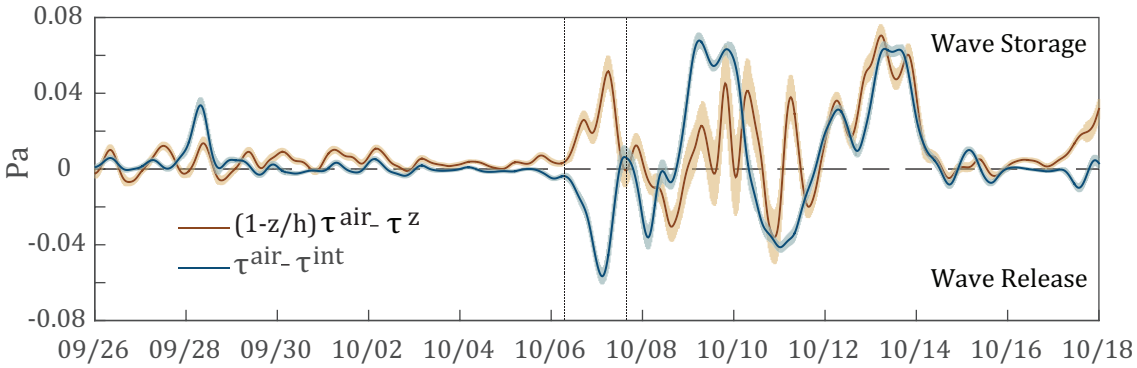

Figure 3.11 The difference between stress measured at z = -1.7 m and z = 2.8 m scaled to the depth of the ADV by surface layer scaling (brown). The fraction of surface stress stored in (positive) or released by (negative) the surface wave field expressed as the difference between the ultrasonic anemometer measurements and the modeled interaction stress (blue). The vertical dotted lines represent a period in which the simulated wave field used in the calculation of wind stress was unrealistic due to topographic sheltering – this period was removed from further analysis.

A strong correlation exists between this wave storage/release term and mean wind direction. Figure 3.12 shows the difference between τ^{air} and τ^{int} plotted as a function of wind direction. When winds blow across dominant fetch axes at moderate to high wind speeds, the generation of short gravity waves in the direction of wind forcing serves as a sink of momentum and can store a significant fraction of the air-sea momentum flux ($\tau^{air} > \tau^{int}$). Conversely, when winds blow along dominant fetch axes (~180° TN or 330° TN), the surface wave field enhances the flux of momentum into the mean flow by releasing momentum through the dissipation of remote wave energy ($\tau^{air} < \tau^{int}$). For periods when there was little momentum storage/release in the surface wave field ($|\ \tau^{air} - \tau^{int}\ | < 0.03$ Pa), the effects of wind direction on wave storage versus wave release

become less clear due to the fact that the wave field at the tower site was likely near fully saturated.

In steady state wind seas, breaking wave energy that exceeds wind input would not make sense. A closer look at the "wave release" period reveals that it corresponds to a brief relaxation in wind forcing and a period when wave energy at the tower site was decreasing. This suggests that estimated release values may be the result of spatial gradients in wave energy transport due to a decaying wind sea. While these results are specific to the middle reaches of Chesapeake Bay, similar dynamics stemming from anisotropic fetch-limitation may be common in coastal environments.

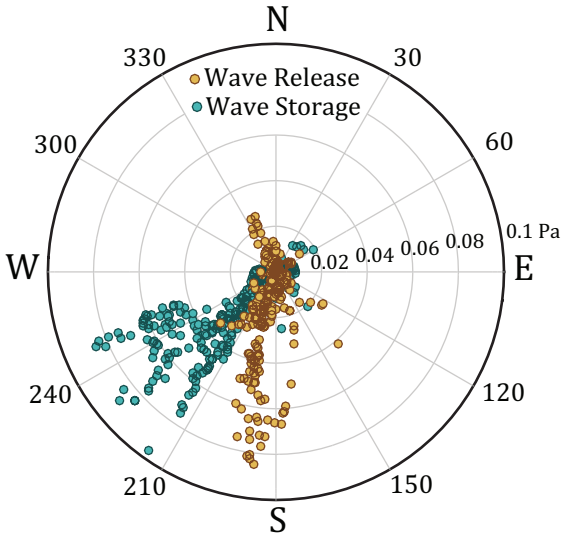

Figure 3.12 $\tau^{air} - \tau^{int}$ plotted as a function of wind direction. When winds blow across the dominant fetch axes of the estuary the surface wave field stores momentum, when winds blow along dominant fetch axes waves enhance the air-sea momentum flux through the dissipation of remote wave energy. Note that light winds (τ < 0.03 Pa) do not exhibit the same directional tendencies.

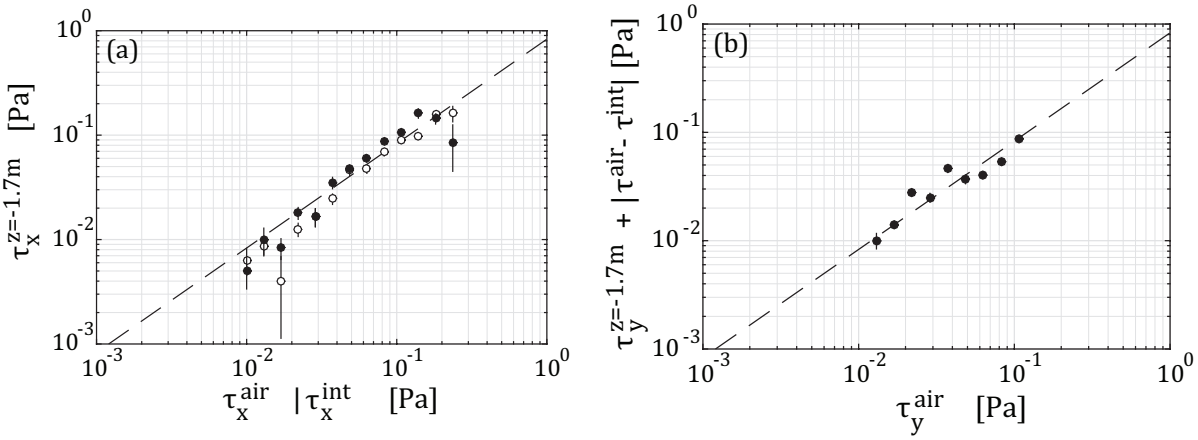

Figure 3.13 Bin-averaged comparison of (a) along-wave components of the interaction stress (black) and the atmospheric stress (white) to the along-wave component of the stress vector measured at z = -1.7 m shown with standard error bars. (b) A comparison between the cross-wave atmospheric stress and the sum of the measured cross-wave stress at z = -1.7 m and the momentum stored in the surface wave field ($\tau^{air} - \tau^{int}$). The dashed line in both subplots represents surface layer scaling.

A shown in Figures 3.10-3.12, the interaction stress is consistent with the stress observed at the uppermost ADV and a storage of momentum in the surface wave field occurs when winds blow across the dominant fetch-axes of the estuary. Therefore, the interaction stress provides a useful framework to address the apparent imbalance between the atmospheric stress vector and the marine stress vector. Using a wave-aligned coordinate system in which x is the direction of dominant wave propagation and y is parallel to wave crests, we examine the air-sea momentum budget for periods when wind and waves are misaligned and wave storage is expected. To isolate these conditions, we limit the analysis to periods when the atmospheric shear velocity exceeded 0.103 m/s and $\theta_{waves} > 20°$. In the along-wave direction, a balance exists between the interaction stress and the stress measured at z = -1.7 m assuming surface layer scaling (Figure 3.13a). In the cross-wave direction, the sum of the stress measured by the ADV and the storage of

momentum in the surface wave field (τ^{air} - τ^{int}) balance the cross-wave component of the atmospheric stress vector (Figure 3.13b). This indicates that the storage of momentum in the surface wave field occurs orthogonal to the direction of dominant wave propagation.

The dynamics of momentum storage in the surface wave field are best understood by looking at the time series of terms in Equation (3.12) (Figure 3.14). Throughout the 10-day event, the dominant term is the horizontal divergence of the surface Reynolds stress in the wavy surface layer, $\frac{\partial}{\partial x_\beta}\left[F\left(\frac{1}{2}-\frac{C_g k_\alpha k_\beta}{Ck^2}\right)\right]$, due to gravity waves. This, in combination with the agreement shown in Figures 3.10, 3.11, and 3.13, suggests that differences in stress between the sonic anemometer and uppermost ADV are directly attributable to the momentum fluxes associated with a fetch-limited wind sea.

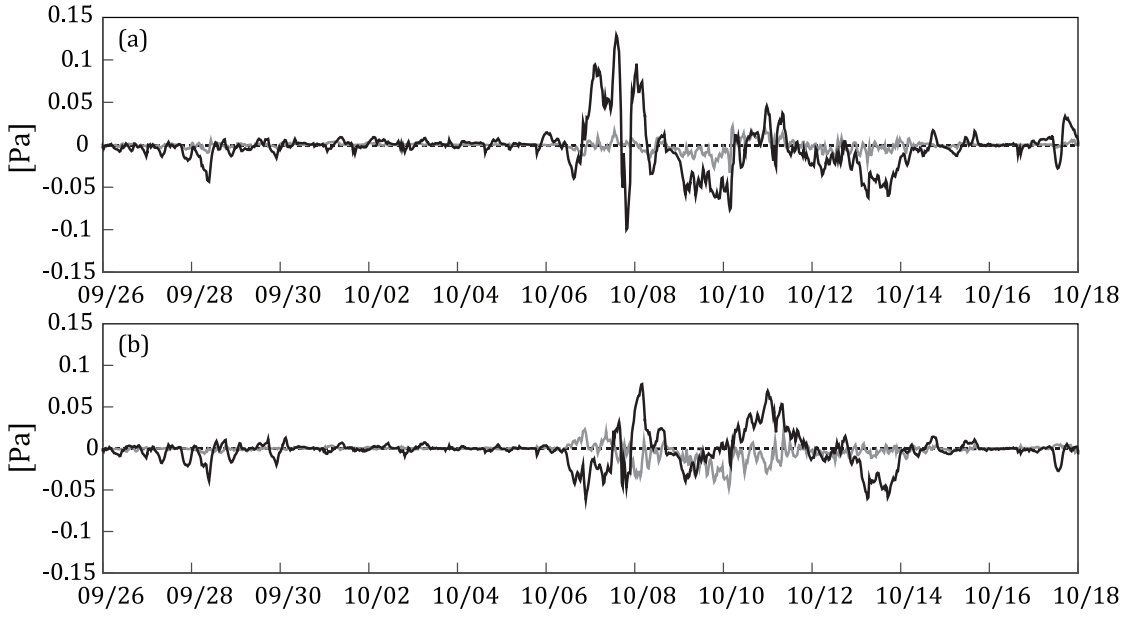

Figure 3.14 (a) E-W component and (b) N-S component time series of source term (grey) and stress divergence (black) terms used in calculation of $\tau^{air} - \tau^{int}$. Note that stress divergence is dominant throughout the deployment.

§3.5 Discussion

The preceding analysis illustrates that the surface wave field plays an important role in regulating the magnitude of the air-sea momentum flux in Chesapeake Bay, but results indicate that the interaction stress vector is aligned with the mean wind direction with a mean departure angle of $1.9 \pm 0.9°$ to the right of the wind. This suggests that another mechanism is responsible for directional divergence of the momentum flux and the apparent steering of the marine stress vector away from applied wind forcing.

Furthermore, Scully et al (2015) presented observations that show coherent turbulent structures beneath breaking waves that were consistent with Langmuir turbulence using the same dataset presented here. While numerous studies have shown that Stokes production is often a dominant term in the TKE budget during times when Langmuir turbulence is present (McWilliams et al 2012, Rabe et al 2014), an analysis of the TKE budget on this dataset indicates that the pressure work was the dominant transport term and balanced dissipation to first order in the surface layer of the estuary (Scully et al 2016). Scully et al also noted that turbulent cospectra exhibited a clear peak at frequencies much lower than the waveband and that these low-frequency motions were consistent with the scale and form of wave-controlled coherent turbulence (Scully et al 2015, Scully et al 2016).

The dominance of a vertical divergence in TKE transport driven by pressure work indicates that breaking waves provide a source of TKE and momentum at the water surface and are important in the structuring the transport of those quantities into the surface layer of the estuary. We evaluate the mean nonlinearity of dominant wind waves

observed during the deployment using the significant steepness parameter suggested by Banner et al (2000), which is equal to half of a significant wave height multiplied by the peak wavenumber: $\varepsilon = H_p k_p / 2$. The significant wave height in the steepness parameter was evaluated for frequencies ranging from 0.7 f_p to 1.3 f_p to account for contributions from shorter, higher frequency waves (Banner et al 2000). Throughout the 10-day wind event, the dominant wind wave steepness exceeded (often by a factor of 2) the breaking threshold of 0.055 proposed by Banner et al (2000). This suggests that the downward sweep of momentum resulting from breaking waves occurred primarily in the direction of dominant wave propagation, which is consistent with the mean agreement between the direction of the marine stress vector and the direction of wave propagation.

While breaking waves likely dominate the transport of TKE downward from the water surface, the vertical shear in the Lagrangian velocity, defined as the sum of the Eulerian velocity and the Stokes drift velocity, can also strain the vorticity field generated beneath breaking waves. We investigate the importance of Stokes drift in momentum exchange within the surface layer of the estuary by calculating stokes drift velocity from directional spectra following Kenyon (1969):

$$U_{stokes}(z) = \int_0^{2\pi} \int_0^{\sigma_{\max}} F(\sigma,\theta)\hat{\sigma}k \frac{\cosh\left(2k\left(h+z\right)\right)}{\sinh^2\left(k\left(h+z\right)\right)} \cos\left(\theta_{waves}\right) \partial\hat{\sigma}\,\partial\theta \qquad (3.14)$$

where $F(\sigma,\theta)$ is the directional wave spectrum, σ is frequency, and θ_{waves} is the angle between wind and waves. We can estimate the direction of Lagrangian shear in the surface layer of the estuary by taking a depth-average of the sum of cross-wind (v)

Eulerian and Stokes drift shear divided by the sum of the along-wind (u) Eulerian and Stokes drift shear (Van Roekel et al 2012).

$$\theta_{S_L} = \text{atan}\left(\frac{\left\langle \frac{\partial V}{\partial z} + \frac{\partial V_{stokes}}{\partial z} \right\rangle_z}{\left\langle \frac{\partial U}{\partial z} + \frac{\partial U_{stokes}}{\partial z} \right\rangle_z} \right) \tag{3.15}$$

Averaging over the upper 5 m of the water column shows that the direction of stress at z = -1.7 m closely matches the observed direction of Lagrangian shear in the estuarine surface layer (Figure 3.15). This is consistent with the inferred angle of Langmuir cells observed during the deployment (Scully et al 2015) and numerical simulations, which have shown that the orientation of Langmuir turbulence is aligned with the direction of Lagrangian shear in the surface layer (Sullivan et al 2012, Van Roekel et al 2012). Scully et al (2015) determined the orientation of Langmuir turbulence observed in the surface layer of the estuary by rotating ADV burst data to find the minimum (most negative) correlation between low-frequency horizontal and vertical turbulent velocities.

The strong agreement between Lagrangian shear and the direction of the momentum flux vector suggests that the combination of dominant wave breaking and vertical shear in the Lagrangian velocity field provide the mechanisms through which the stress vector in the surface layer of the estuary is steered away from applied wind forcing. We hypothesize that breaking waves were the primary pathway through which momentum was transferred between the air and the oceanic surface layer and that breaking waves injected momentum in the direction of dominant wave propagation

evidenced by the mean offset between the direction of the marine stress vector and local wind (atmospheric stress) direction (Figure 3.15). Furthermore, the strong correlation between the Lagrangian shear direction and marine stress direction suggests that Langmuir turbulence likely played a dominant role in momentum transfer within the oceanic surface boundary layer.

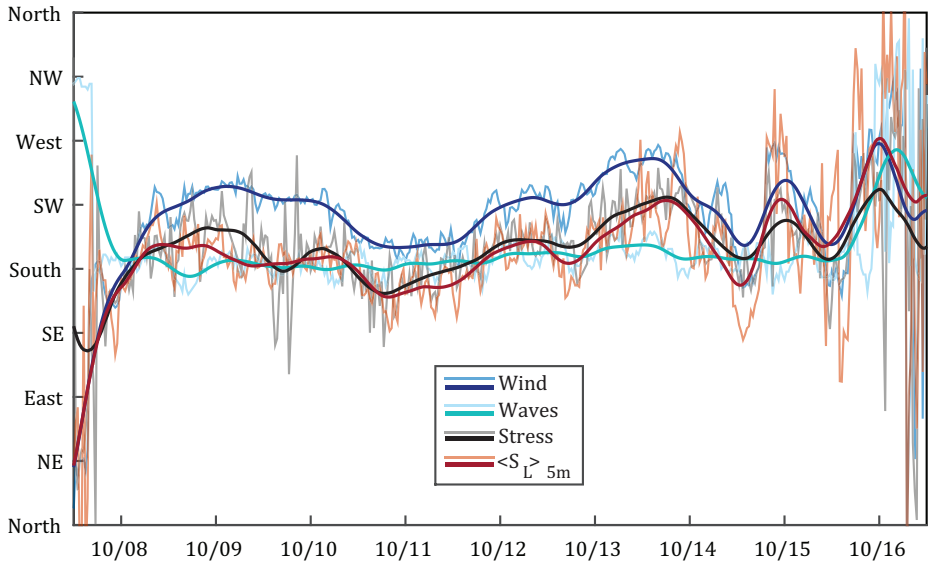

Figure 3.15 Time series of low-pass filtered wind (dark blue), wave (light blue), stress at z=-1.7m (black), and depth-averaged Lagrangian shear (red) for a 10-day nor'easter in October 2013. The direction of the momentum flux vector at the uppermost ADV is closely correlated to the direction of Lagrangian shear in the surface layer of the estuary.

§3.6 Conclusions

Anisotropic fetch-limitation in the middle reaches of Chesapeake Bay results in an environment where wind and waves are commonly and persistently misaligned. Although pure wind seas characterize the mid-Bay, directional wave spectra show that dominant waves develop along the dominant fetch axes of the estuary and may be significantly misaligned with the wind. Direct measurements of the momentum flux collected above and below the water surface indicate that the surface wave field plays an important role in the local air-sea momentum budget beyond simply the enhancement of surface fluxes associated with increased drag at the water surface and/or the injection of TKE by breaking waves.

The stress vector in the surface layer of the estuary was aligned more with wave forcing than wind forcing and was highly correlated to the direction of Lagrangian shear in the upper 5m of the water column. An apparent depth and directional divergence occurs between the ultrasonic anemometer ($z \sim 2.8$ m) and the uppermost ADV ($z \sim -1.7$ m). We address this observation by first partitioning the momentum flux between surface gravity waves and the mean flow using the interaction stress described by Hasselmann (1971) and Ardhuin et al (2004). Comparing the interaction stress magnitude to the magnitude of the momentum flux measured at the uppermost ADV agrees with a linear surface layer scaling of stress. Additionally, results indicate that the surface wave field can store a significant fraction of the momentum flux, up to 30-40%, at times when the wind blows across dominant fetch axes.

Fetch-limitation results in bounded wave growth, which for large wind events can result in very young seas that are not in equilibrium with wind forcing. The generation of

short gravity waves dominates the drag felt by the wind field and may serve as a momentum sink in the local momentum budget of the oceanic surface boundary layer. This is especially true when dominant, longer waves are misaligned with wind forcing. An analysis of the wave momentum evolution equation using a third-generation wave model and direct observations of wind stress indicate that the stress fraction stored in/released by the surface wave field is dominated by the horizontal stress divergence associated with a wavy instantaneous free surface.

While the interaction stress properly accounts for the vertical-divergence of stress that occurs at the air-sea interface, it does not capture the directional divergence of stress that results in the marine stress vector being steered away from applied wind forcing in the surface layer of the estuary. The authors hypothesize that the vorticity field generated by breaking waves is strained in the direction of the Lagrangian shear in a manner similar to Langmuir turbulence. However, several studies have shown that as waves become increasingly misaligned with the wind, the turbulence regime can shift from a Langmuir-dominated regime to an isotropic, shear-dominated regime (McWilliams et al 1997, Polton and Belcher 2007, Sullivan et al 2012, Rabe et al 2014). Additionally, tidal shear can significantly distort Langmuir turbulence in coastal environments (Kukulka 2011, Scully et al 2015). As Scully et al (2016) showed, the TKE budget measured during this deployment did not show a significant Stokes production term; rather, the dominant term that resulted in elevated dissipation was pressure work. Therefore, we suggest that vertical shear in Stokes drift does not significantly enhance near-surface turbulence, but rather modifies vertical transport regimes which act to strain the stress tensor into the direction of the Lagrangian shear in the surface layer of the estuary.

While the details of this manuscript are specific to the middle reaches of Chesapeake Bay, the trends presented suggest that further research is needed in fetch-limited, coastal environments where the tendency for misaligned wind and wave fields may be common. These results indicate that the surface wave field can significantly affect the translation of wind stress across the air-sea interface and may play an important role in coastal momentum budgets.

§3.7 Acknowledgements

This manuscript benefited greatly from the comments and suggestions of Dr. Bill Boicourt, Dr. Ming Li, and two anonymous reviewers. This work was supported by National Science Foundation Grants OCE-1061609 and OCE-1339032. UMCES contribution no. XXXX.

CHAPTER 4

WIND-WAVE EFFECTS ON ESTUARINE TURBULENCE

Preface

This chapter is a reproduction of work that will soon be submitted for publication with coauthors Larry Sanford and Malcolm Scully. The right to reuse this work will be retained by the authors when publication rights and nonexclusive copyright are granted to the publisher.

Fisher A.W., L.P. Sanford, and M.E. Scully (in prep): Wind-Wave Effects on Estuarine Turbulence: a comparison of observations and second-moment closure predictions.

§4.1 Introduction

Wind-driven flows can dominate subtidal material exchange in estuarine environments including oxygen (Scully 2010a, Scully 2010b, Scully 2013), sediments (Chen et al 2009), and salt (Geyer 1997, Scully et al 2005, Chen & Sanford 2009, Li & Li 2011, Li & Li 2012). Breaking surface waves serve as the principal pathway through which momentum and mechanical energy are transferred from the atmosphere to the oceanic surface boundary layer (Melville 1996) and, as such, can play a pivotal role in structuring turbulent mixing beneath the water surface. Within the surface boundary layer, surface waves can influence hydrodynamics in three principal ways (Jones & Monsmith 2008a): (1) direct injection of turbulent kintetic energy beneath breaking waves (e.g. Terray et al 1996); (2) enhanced vertical transport driven by coherent Langmuir turbulence (Craik & Leibovich 1976, Leibovich 1983); and (3) Reynolds stresses generated by nonlinearities in the surface wave field (Magnaudet & Thais 1995). This study examines the effects of (1) on turbulence profiles measured in Chesapeake Bay and discusses the interplay of (1 & 2) in governing momentum and energy transfer in the wave-affected surface layer.

Injection of TKE to the oceanic surface boundary layer by breaking waves can result in turbulent kinetic energy dissipation rates that are orders of magnitude larger (Kitaigorodskii et al 1983, Agrawal et al 1992, Anis & Moum 1995, Terray et al 1996, Drennan et al 1996, Soloviev et al 2005, Fedderson et al 2007, Jones & Monismith 2008a, Gerbi et al 2009, Gemmrich 2010) than those produced by shear production near a rigid boundary (Hinze 1975). Observational constraints have made directly measuring

turbulent fluxes difficult and as a result most studies have been constrained to an analysis of dissipation and turbulent vertical velocity statistics. Several studies conducted in the coastal ocean have shown that the region of elevated dissipation beneath breaking waves can occupy a significant fraction of the water column (Jones & Monismith (2008a), Young et al 2005, Scully et al 2016).

During an experiment conducted in the middle reaches of Chesapeake Bay in the fall of 2013, breaking waves dominated the transfer of momentum and energy in the oceanic surface layer (Scully et al 2016) and coherent turbulent structures consistent with Langmuir turbulence were documented (Scully et al 2015). Building on analyses presented in a series of manuscripts describing wind-forced responses observed during this experiment (Scully et al 2015, Scully et al 2016, Fisher et al *in review*), this paper examines the effects of wind-waves on vertical profiles of estuarine turbulence and compares observations to the predictions of second moment turbulence closure schemes.

The paper is organized as follows: (1) background material on the scaling relations used describing turbulence beneath breaking waves, second-moment turbulence closure schemes used in circulation modeling, and a framework for describing boundary- versus buoyancy-controlled turbulence; (2) field data collection and analysis methods; (3) results of the experiment, which relate the observed TKE budget to parameters used in second-moment closures (and an overview of the turbulent structure of the wind-driven response observed at the tower site); (4) a discussion of predicted and observed vertical mixing profiles; and (5) a summary of research findings and conclusions.

§4.2 Background

4.2.1 The Wave Transport Layer

The turbulent kinetic energy equation for a wave-affected surface layer can be expressed as follows (McWilliams 1997):

$$\frac{Dk}{Dt} = \langle u_i' w' \rangle \frac{\partial U_i}{\partial z} + \langle u_i' w' \rangle \frac{\partial U_{Si}}{\partial z} + \frac{g}{\rho_0} \langle \rho' w' \rangle + \frac{\partial}{\partial z} \left[\frac{1}{2} \langle u_j'^2 w \rangle + \frac{1}{\rho_0} \langle p' w' \rangle \right] - \varepsilon \qquad (4.1)$$

(i) (ii) (iii) (iv) (v) (vi)

where $k = \frac{1}{2}\left(\langle u'^2 \rangle + \langle v'^2 \rangle + \langle w'^2 \rangle \right)$ is the turbulent kinetic energy (TKE). The terms on the right hand side are: (i) Eulerian shear production, (ii) Stokes shear production, (iii) buoyancy flux, the divergence of the (iv) TKE flux and (v) pressure work, and (vi) dissipation. We refer to the sum of the TKE flux and pressure work as the total TKE transport. By assuming that wave breaking is the principal source of TKE and that breaking injects energy to a depth on the order of the significant wave height, Terray et al (1996) postulated that the wave affected-surface layer (WASL) consists of two sublayers: (1) a wave breaking sublayer in which direct injection of TKE near the surface leads to region of constant dissipation and negligible shear production; and (2) a wave transport layer where TKE is transported away from the surface by turbulent eddies such that dissipation is balanced by the vertical divergence of TKE transport (Terray et al 1996).

Collapsing their data using the estimated wind energy input to surface waves (F_0), the significant wave height (H_S), and the depth below the surface (z), Terray et al (1996) postulated a dissipation scaling for the wave transport layer:

$$\frac{\varepsilon H_s}{F_0} = c\left(\frac{|z|}{H_s}\right)^{-b} \tag{4.2}$$

where c and b were determined to be 0.3 and 2, respectively. We note that for the remainder of this paper, we will use an upward-positive z coordinate system with z=0 at the mean free surface.

The relationship in Equation (4.2) has been shown to hold for deep-water wave breaking conditions in both young, fetch-limited wind seas (Terray et al 1996, Jones & Monismith 2008b) and more developed wind seas (Drennan et al 1996). The model is valid over a range of depths determined by two factors: (1) the depth-integrated dissipation within the wave-affected surface layer matches the downward flux of TKE at the surface due to wave energy dissipation and (2) as shear production becomes more dominant, the dissipation rate reduces to wall layer scaling:

$$\varepsilon = \frac{u_{*s}^3}{\kappa |z|} \tag{4.3}$$

where u_{*s} is the surface shear velocity: $u_{*s} = \sqrt{\tau_{z=0}/\rho}$. Below the wave transport layer, the TKE budget is expected reduce to a balance between shear production and dissipation

consistent with a surface log layer. Field measurements (Agrawal et al 1992) and laboratory studies (Monismith and Magnaudet 1998) have shown that dissipation scales with wall layer theory below the wave transport layer, but in shallow coastal environments the wave transport layer may also transition directly to a bottom boundary layer (Jones & Monismith 2008b). The model assumes that one half of the surface TKE flux generated by wave breaking reaches the wave transport layer. Using the integral constraint on the wave transport layer, Terray et al (1996) determined that the depth of the wave breaking sublayer (constant dissipation layer) was $z_0 = -0.6H_S$ for the fetch-limited wind seas observed during the experiment – a result consistent with the laboratory results of Rapp & Melville (1990). We note that z_0 is a displacement height, not a roughness parameter, and represents the base of the active breaking and bubble entrainment sublayer.

The assumption of a constant dissipation layer very near the surface has been challenged by the wave-following measurements of Gemmrich & Farmer (1999), Soloviev & Lukas (2003) and Gemmrich & Farmer (2004), which suggest that the value of z_0 should be much less than the ratio of $|z_0/H_S|=0.6$ imposed by Terray et al (1996) scaling. Furthermore, modifications to the scaling in Equation (4.2) are needed when the model is applied to mixed seas with significant swell energy (Greenan et al 2001).

4.2.2 Turbulence Closure Models

In ocean circulation models, second moment closure schemes are often used to parameterize turbulence (Warner et al 2005). Most closure models do not include Stokes production and pressure work terms, reducing Equation (4.1) to:

$$\frac{Dk}{Dt} = P + B + F_{TKE} - \varepsilon \qquad (4.4)$$

where F_{TKE} represents the vertical divergence of the sum of turbulent and viscous TKE transport. Second-moment closure schemes solve Equation (4.4) in combination with a similar transport equation for dissipation (k-ε, Rodi 1987), turbulent length scale (k-kl, Mellor-Yamada 1982), or turbulent velocity (k-ω, Wilcox 1988). Some attempts have been made to incorporate the effects of Langmuir turbulence into second moment closure schemes (via the Stokes production term) using Mellor-Yamada (1982) style closure schemes (Kantha & Clayson 2004, Harcourt 2013, Harcourt 2015).

Several studies have used 1D vertical models with second-moment closure schemes to simulate the effects of wave breaking with good accuracy (Craig & Banner 1994, Craig 1996, Burchard 2001, Umlauf & Burchard 2003, Stips et al 2005). However, most of these studies focused on reproducing measured dissipation profiles and did not directly compare observed and modeled momentum fluxes due to limited data. The landmark model of Craig & Banner (1994) reproduced dissipation profiles observed by Agrawal et al (1992, Anis & Moum (1992), and Osborn et al (1992) quite well using a Mellor-Yamada (1982) closure scheme. However, these datasets did not include the

elevated near-surface dissipation rates measured by Terray et al (1996) or Drennan et al (1996). Terray et al (1999) adapted the original Craig & Banner (1994) model to match these observations through a modification to the expression for turbulent length scale (Terray et al 1999, Jones & Monismith 2008b).

Within second-moment closure schemes, the vertical transport of momentum and buoyancy is modeled as a downgradient process (Rodi 1980):

$$\left\langle u'w' \right\rangle = A_z \frac{dU}{dz} \qquad (4.5) \qquad\qquad \frac{g}{\rho_0}\left\langle \rho'w' \right\rangle = K_z N^2 \qquad (4.6)$$

where the eddy viscosity, A_z, and the eddy diffusivity, K_z, can be modeled as the product of a turbulent velocity and a turbulent length scale. Following the k-ε notation, the turbulent length scale is proportional to the ratio of TKE and dissipation (Tennekes & Lumley 1972):

$$l = c_\mu^{(3/4)} \frac{k^{3/2}}{\varepsilon} \qquad (4.7)$$

where c_μ is a nondimensional parameter known as the stability function. Assuming that the momentum flux is transported by the same family of eddies that govern TKE dynamics, the master length scale modeled in Equation (4.7) is equivalent to the Prandtl mixing length near rigid boundaries (Mellor & Yamada 1982). In an unstratified log layer where the ratio of the Reynolds stress to TKE is constant (e.g. a constant stress layer), c_μ

reduces to a constant value of c_μ^0 =0.09 (Umlauf & Burchard 2003). Using a constant value of $c_\mu = c_\mu^0$ =0.09 in Equation (4.7) yields a turbulent length scale that is consistent with the expected boundary layer scaling of a neutral log layer:

$$l_{BL} = \kappa |z| \sqrt{1 - \frac{|z|}{h_{bl}}} \qquad (4.8).$$

where κ=0.41, z is the distance from the boundary, and h_{bl} is height of the boundary layer (Scully et al 2011). By assuming that the velocity scale for energy-containing turbulent motions scales as $k^{1/2}$, Equation (4.7) can be used to formulate estimates of the eddy viscosity (Eqn 4.9) and eddy diffusivity (Eqn 4.10) based on terms in the TKE budget.

$$A_z = c_\mu \frac{k^2}{\varepsilon} \qquad (4.9) \qquad\qquad K_z = c_\mu' \frac{k^2}{\varepsilon} \qquad (4.10)$$

Umlauf & Burchard (2003) demonstrate that the formulation of different second-moment closure schemes is structurally similar regardless of the dynamical equation used in conjunction with the TKE equation. Therefore the formulation of the stability function, rather than the choice of model, influences model performance (Burchard et al 1998). Some modeling studies of wave transport layers have used a constant stability function (Craig & Banner 1994), but other approaches assume that the stability functions are functions of nondimensional shear, α_S, and stratification, α_N, (e.g. Burchard & Bolding 2001):

$$\alpha_S = S^2 \frac{k^2}{\varepsilon^2} \qquad (4.11) \qquad\qquad \alpha_N = N^2 \frac{k^2}{\varepsilon^2} \qquad (4.12)$$

Using the definition of eddy viscosity and Equation (4.9), the relationship between the momentum flux and TKE stress can be shown as (Scully et al 2011):

$$\frac{<u'w'>}{k} = \sqrt{c_\mu \frac{P}{\varepsilon}} = c_\mu \sqrt{\alpha_S} \qquad (4.13)$$

where the ratio of the Reynolds stress to TKE is known as the nondimensional stress and expresses the efficiency of turbulent motions in producing a momentum flux (Scully et al 2011). Stability functions are therefore used to relate TKE dynamics to the momentum flux within second-moment closure models.

However, the assumption that P+B=ε invokes that the vertical flux of TKE is modeled as a downgradient process within the stability function (Burchard & Boulding 2001). This leads to "quasi-equilibrium" stability functions that retain the full TKE equation, but whose solutions are limited to turbulence in structural equilibrium (Kantha & Clayson 1994, Scully et al 2011). Most numerical circulation models employ quasi-equilibrium stability functions (Chen et al 2003, Warner et al 2005), but nonequilibrium formulations (discussed below) are becoming increasingly common in coastal simulations (Warner et al 2005).

The quasi-equilibrium assumption may not be valid for strongly stratified estuarine flows (Scully et al 2011) or wave transport layers, where the vertical flux of TKE may be countergradient (Scully et al 2016). Nonequilibrium stability functions

account for departures from the P + B = ε balance expected for turbulence in structural equilibrium (Umlauf & Burchard 2003). Nonequilibirum formulations of the stability function, such as that proposed by Canuto et al (2001), do not restrict values to structural equilibrium solutions, and as such do not assume that the vertical TKE flux is a downgradient process. Burchard (2001) used the Canuto et al (2001) stability function formulation to reproduce dissipation profiles beneath breaking waves with good accuracy. A detailed discussion of nonequilibrium formulations of the stability function can be found in Burchard & Bolding (2001).

4.2.3 Buoyancy vs. Boundary-limited Turbulence

Chesapeake Bay is a partially stratified estuary, in which stratification often suppresses vertical mixing. It is therefore informative to consider the framework of stratified turbulence before proceeding to an analysis of the effects of surface waves on turbulent quantities. Using a hierarchy of length scales for stratified flows ranging from the largest (Ozmidov) to the smallest (Kolmogorov), three ratios can be calculated which form the basis of a state-space diagram that describes the relative influence of inertia, buoyancy, and frictional forces on turbulent mixing (see Ivy & Imberger 1991 for more details).

Under stratified conditions, the upper limit imposed in most models on turbulent length scales is the Ozmidov scale (Dillon 1982), which is a function of the turbulent dissipation rate and the Brunt-Väisälä frequency.

$$l_O = \left(\frac{\varepsilon}{N^2} \right)^{1/2} \tag{4.14}$$

The Ozmidov scale is proportional to the Thorpe scale and represents the largest overturn possible in the presence of stratification (Dillon 1982, Stacey et al 1999) or the point at which inertial and buoyancy forces are equal (Scully et al 2011). While applied as a numerical upper limit in simulations of stratified flows, the Ozmidov scale is not a dynamical property of most second moment closure models (Galperin et al 1988).

Formally, the integral length scale of turbulence represents the aggregated effect of all turbulent motions and is difficult to measure directly in the field (Stacey et al 1999). As a result, the Prandtl mixing length (l_M) is often used to describe energy-containing turbulent scales. The Prandtl mixing length is a shear-based estimate defined as follows:

$$l_M = \left(\frac{<u'w'>}{S^2} \right)^{1/2} \tag{4.15}$$

where S is the mean shear. Finally, the Kolmogorov length scale represents the scale at which overturning eddies are ultimately damped and turbulent kinetic energy is dissipated by molecular viscosity. By comparing the Prandtl mixing length and the Ozmidov scale, the influence of stable stratification on energy-containing turbulent scales can be determined using directly measured quantities.

§4.3 Methods

4.3.1 Field Observations

At the center of an extensive field experiment conducted in the fall of 2013, a turbulence tower was deployed on the western shoal of Chesapeake Bay (38 27' 39", 76 24' 44") in a 14m deep region of slowly-varying bathymetry. The tower was held vertically rigid using four guy-wires, which were secured to the top of the tower and anchored to 1000lb railcar wheels (Scully et al 2015, Fisher et al *in review*). The tower was deployed on September 18, 2013 and recovered on October 29, 2013. A schematic of the tower and map of the deployment site are shown in Figure 4.1.

A vertical array of Nortek Vector Acoustic Doppler Velocimeters (ADVs) provided direct measurements of turbulent fluxes and mean velocities (burst averages). The downward-looking ADV heads were mounted on 1m aluminum arms attached to the tower, spaced ~2m apart, starting at approximately 1.5m below the mean water surface. The aluminum arms were oriented due west. The ADVs recorded three-dimensional velocity and pressure data at 32Hz in 28-minute bursts centered 30 minutes apart. Temperature and conductivity measurements were collected every 5 minutes using six Seabird MicroCat CTDs mounted to the tower with sampling volumes aligned to the ADV sensor heights.

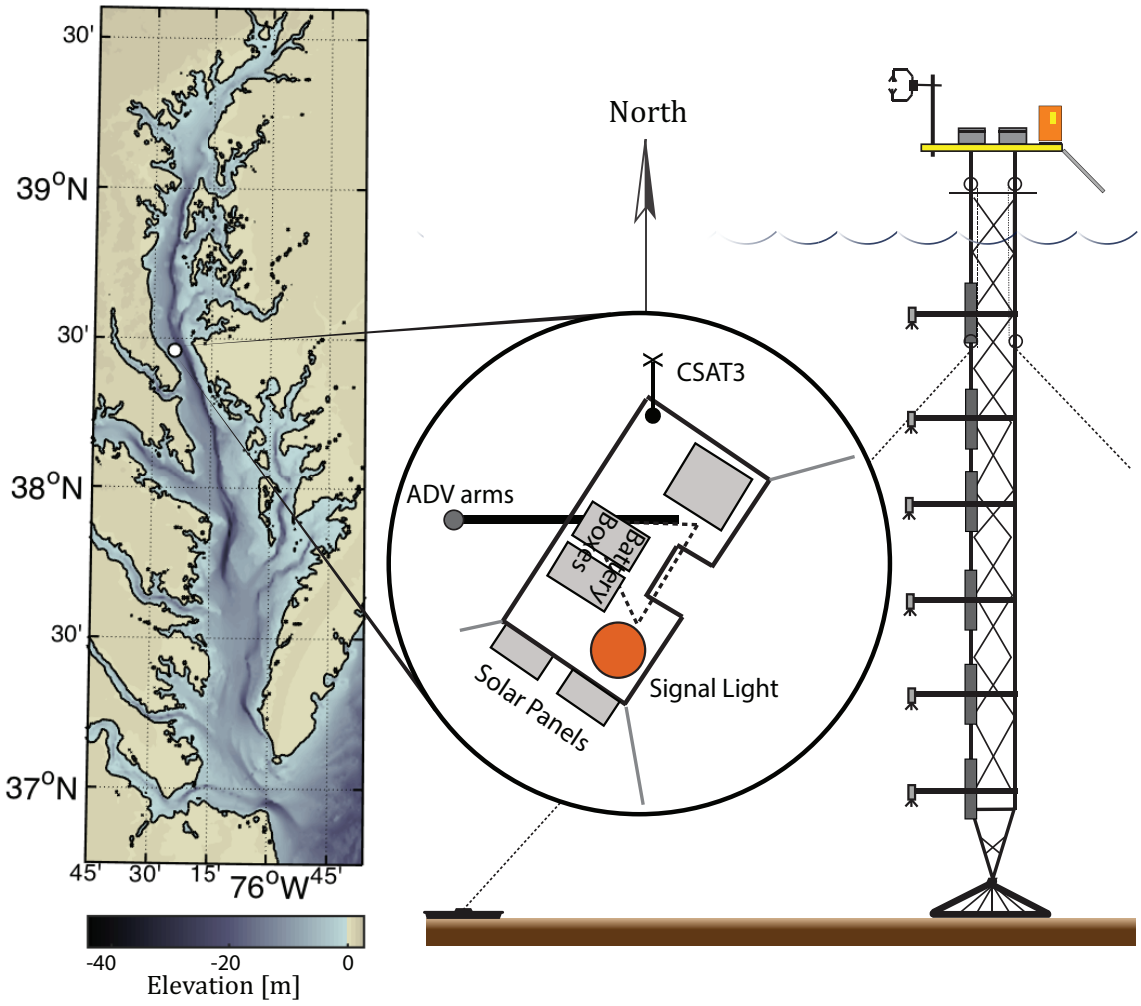

Figure 4.1 Map and tower schematic. Inset diagram shows orientation of the tower, ultrasonic anemometer, ADVs, and TCOs. Tower schematic at right shows vertical array structure.

Direct measurements of the total wind stress and sensible heat flux were collected by a Campbell Scientific CSAT3 ultrasonic anemometer with fine-wire thermocouple deployed on an aerial platform atop the tower. The anemometer was oriented due North and had a sampling volume elevation of ~2.82m above MSL. The system sampled the 3D velocity field and air temperature at 10Hz continuously. Atmospheric measurements of wind stress were calculated by integrating velocity cospectra for frequencies less than 2Hz in 30-minute blocks (Reider et al 1994). The sensitivity of vertical flux measurements to variations in vertical velocity prompted a tilt correction using the planar fit method (Wilczak et al 2001) on daily subranges of the anemometer data as described in Fisher et al (2015). The anemometer was deployed on September 25, 2013 and recovered on October 28, 2013.

Directional wave spectra were calculated from the uppermost ADV data (z = -1.7m) using the PUV method based on linear wave theory and the DIWASP Matlab toolkit (Johnson 2002). For details on wave processing used in this analysis, see Fisher et al (*in review*). Vertical profiles of Stokes drift velocity were calculated from directional wave spectra following Kenyon (1969).

The surface TKE flux (F_0) was estimated as the wind input into the surface wave field:

$$F_0 = g\int_0^{2\pi}\int_0^{\omega_{max}} \beta F(\omega,\theta)\partial\omega\,\partial\theta \qquad (4.16)$$

where β is the e-folding scale for the growth rate of wave energy formulated by Plank (1982) and F(ω,θ) is the observed directional wave spectra. The surface TKE flux can

also be expressed using an empirical wave energy factor, G_T (Craig & Banner 1994), which is often assumed to be wave-age dependent (Drennan et al 1996, Terray et al 1996). Following Kundu (1980), the wave energy factor was calculated using a least squares regression of estimated F_0 values and the directly measured wind stress, where u_{*w} is the water side shear velocity of the total wind stress, such that:

$$F_0 = G_T u_{*w}^3 \qquad (4.17).$$

As discussed in Fisher et al (*in review*), significant momentum storage within the surface wave field can occur in the middle reaches of Chesapeake Bay due to a horizontal divergence of wave energy transport that develops as a result of anisotropic fetch-limitation. Accounting for momentum storage in the surface wave field was needed to close the air-sea momentum budget at the tower site (Fisher et al *in review*) and should therefore be considered when using F_0 as a scaling for dissipation within the wave transport layer. The total wind energy input (F_0) was adjusted for the effects of momentum storage within the wave field using a ratio of the shear stress at the mean free surface to the total wind stress (u_{*s}^3 / u_{*w}^3), which reduced the surface TKE flux by an average of 8%. A linear regression of u_{*s}^3 and the adjusted F_0 value yielded a mean wave energy factor (G_T) of 77.

A co-located bottom lander equipped with an ADV, which sampled at 32Hz in 28 minute bursts, provided direct measurements of the bottom Reynolds stress. The ADV sensor head was mounted approximately 75 cm above the bed. In an estuarine tidal

bottom boundary layer, the constant stress layer thickness may be constrained by density stratification to very near the bed. Because the sensor height of the bottom-deployed ADV may have protruded above the top of the bottom log layer, bottom stress was calculated as the average of a cospectral estimate (integrated over $f < 0.1$Hz) and a TKE-based estimate (Pope et al 2006) following Kim et al (2000).

4.3.2 Terms in the TKE Budget

Terms within the TKE budget can be directly estimated using observed cospectra and mean shear measured by the vertical array of ADVs. Direct estimates of the buoyancy flux could not be made using measurements collected during this experiment. However, using the surface heat flux, Scully et al (2015) indirectly estimated the buoyancy term and showed that it was two orders of magnitude smaller than observed dissipation rates (e.g. Scully et al 2016). To avoid artificial enhancement of stress estimates from correlated wave orbital velocities, the integration of ADV burst velocity cospectra was limited to frequencies less than 0.1Hz, below the wave band. Dissipation was estimated by fitting the semiempirical model of Kaimal et al (1972) to vertical velocity spectra following the method outlined in Gerbi et al (2009). The method fits the Kaimal et al (1972) model using inertial range scaling (Tennekes & Lumley 1972) and accounts for unsteady advection by orbital velocities using the analytical model of Lumley & Terray (1983). The Gerbi et al (2009) approach extends the method outlined in Fedderson et al (2007) to directional wave spectra.

4.3.3 Data Analysis Conditions

The analysis period was constrained to three weeks spanning September 25, 2013 to October 18, 2013 due to the exhaustion of ADV batteries. Due to depth-limitations, reliable wave data provided by the uppermost ADV were limited to conditions when the significant wave height was greater than 15cm and the peak period was greater than 1.6s. Data analysis was limited to periods in which the atmospheric surface boundary layer was hydraulically rough ($\sqrt{\tau_w/\rho_a}$ >0.103) and when the observed wind speed was greater than 3 m/s. Periods when the two-parameter least squares fit to vertical velocity spectra provided unrealistic physical values for the roll-off wavenumber and variance were omitted. Finally, as discussed in Gerbi et al (2009), periods when the mean current was not strong enough to stop surface wave orbital velocities from advecting ADV sensor wakes back into the sampling volumes were omitted. Following Gerbi et al (2009), the advective threshold used here was $U_d/\sigma_d > 3$, where U is the mean current and σ is the wave orbital velocity variance in the downstream direction. Five hundred eighty-nine time points, ~44% of the deployment record, satisfied all of these criteria and were used in the analysis.

§4.4 Results

4.4.1 Deployment Conditions

A 10-day Nor'easter occurred between October 6 and October 16, 2013 and dominated the wind and wave conditions recorded during the deployment. The event was characterized by winds blowing from NE to N at an average wind speed of 7 m/s. Wind stress peaked at 0.31 Pa and averaged 0.13 Pa. The event generated a surface wave field that had a significant wave height of ~1m and typical peak wave period of 4 seconds. Tidal velocities were on the order of 0.5m/s and were aligned with the central channel at 150° TN. During periods of energetic wind-mixing, density stratification was generally weak (top to bottom density difference of ~0.5kg/m^3), except for persistent near bottom stratification at z~-10m. During the latter half of the Nor'easter, the water column was moderately stratified (top to bottom density difference of ~3kg/m^3). A summary of tower conditions observed during the deployment is presented in Figure 4.2.

Wind forcing generated a flow response within the estuary that resulted in near-surface shear that was much lower than expected for a logarithmic surface boundary layer (Figure 4.3). A time series of the Eulerian shear measured between the top two ADVs (z ~ -2.5m) shows that during periods of active wind and wave forcing, the Eulerian shear significantly lower than log surface log layer scaling: $\partial U/\partial z = u_{*_s}/\kappa|z|$. Between October 9 and October 11, the near-surface Eulerian shear was nearly an order of magnitude lower than surface log layer scaling. This dramatic reduction in shear is consistent with the conceptual model of a shear-free transport layer and provides a basis

for further analysis of scaling arguments used in describing a turbulent transport layer beneath breaking waves.

Examining the data collected during this experiment through the lens of stratified turbulence reveals that: (a) Chesapeake Bay is considerably more energetic (Re_t ranging from 10^2 to 10^6) than the lake data (Re_t ranging from 10^1 to 10^4) analyzed in Ivy & Imberger (1991), consistent with previously reported observations of estuarine turbulence (e.g. Stacey et al 1999); and (b) despite moderate wind forcing, a significant fraction of the data falls within the stratification-controlled regime discussed by Luketina & Imberger (1989) and Ivy & Imberger (1991). This suggests that the turbulence generated during observed wind events was anisotropic in a significant fraction of the water column. Additionally, persistent near bottom-stratification limited vertical mixing and likely capped the vertical extent of the bottom boundary layer with a number of near bottom data falling at the transition between Region II (stratification-controlled) and Region III (buoyancy-suppressed) of the Ivy & Imberger (1991) state-space. Because data in Region III represents internal wave energy rather than active turbulence, all data for which the turbulence activity, $\varepsilon/\nu N^2$, was less than 20 (Itsweire et al 1993, Stacey et al 1999) was omitted from any further analysis (2% of the data).

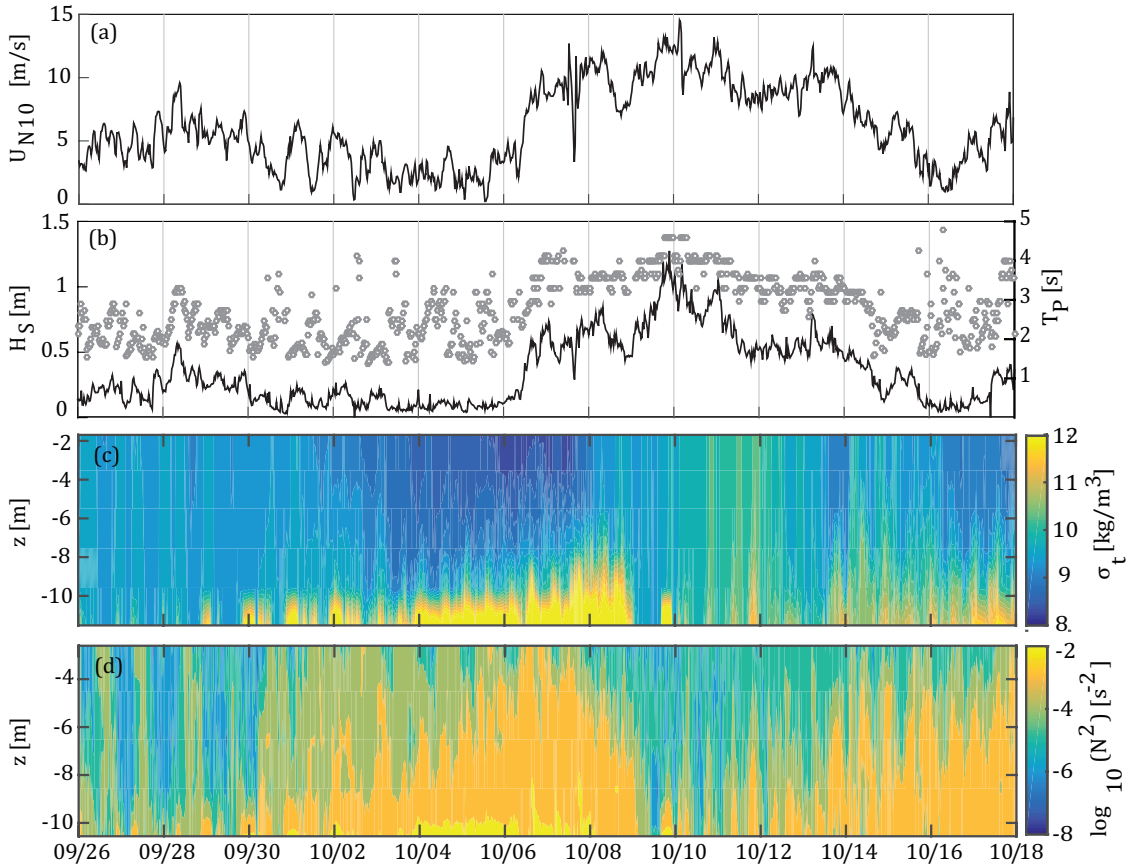

Figure 4.2 Time series of deployment conditions: (a) 10 meter neutral wind speed, (b) significant wave height and peak period, (c) density anomaly, and (d) N^2.

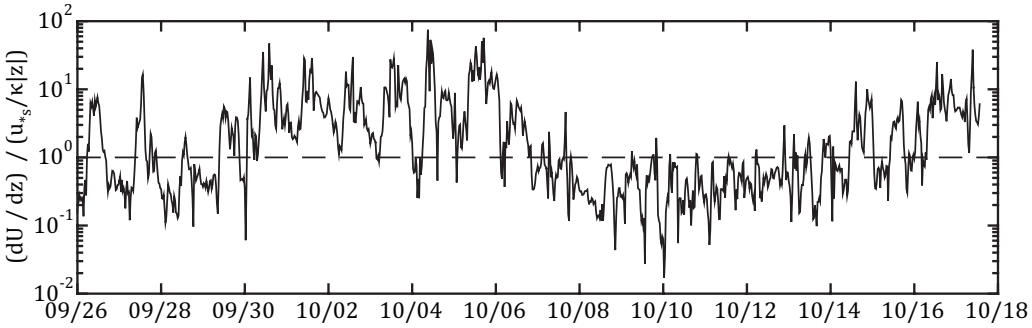

Figure 4.3 Time series of Eulerian shear measured at z ~ -2.5m normalized by surface log layer scaling: $dU/dz=u_{*s}/\kappa z$. During periods of active wind and wave forcing, the measured near-surface shear was much less than that expected for a surface log layer and was consistent with the conceptual model of a free shear transport layer used in scaling turbulent quantities beneath breaking waves.

4.4.2 TKE Budget

As documented in numerous other studies (Agrawal et al. 1992, Anis and Moum 1995, Terray et al. 1996, Drennan et al. 1996, Greenan et al. 2001, Feddersen et al. 2007, Jones and Monismith 2008b), dissipation rates measured beneath breaking waves greatly exceeded wall layer scaling during this experiment. Within the wave-affected surface layer, elevated dissipation rates were balanced to first order by a divergence in the vertical transport of TKE (Figure 4.4). TKE transport was driven primarily by the pressure work associated with breaking-induced vortices as discussed by Scully et al (2016). This pressure work was more than an order of magnitude larger than the sum of the Eulerian and Stokes drift shear production and was a factor of 4 larger than the divergence in the vertical flux of TKE (Scully et al 2016). Below the wave transport layer, dissipation was primarily balanced by shear production. For a more thorough analysis of the TKE budget observed during this experiment, including a discussion of the TKE transport driven by pressure work, see Scully et al (2016).

During the experiment, energetic wave breaking (Scully et al 2016) and Langmuir turbulence (Scully et al 2015) were documented during periods when wave forcing was present. Because wave breaking can provide a seed of vertical vorticity that generates Langmuir turbulence through the CL2 vortex force mechanism (Craik & Leibovich 1976, Leibovich 1983), it is informative to quantify the relative contributions of Langmuir turbulence and wave breaking to the surface TKE flux. Skyllingstad & Denbo (1995) suggest that the TKE flux generated by the CL2 vortex force should scale with $U_S u_{*_S}^2$, where U_S is the surface stokes drift. Following Jones & Monismith (2008a), the ratio of

TKE flux generated by Langmuir turbulence to the TKE flux generated by breaking waves within the wave transport layer can then be expressed as $U_S/G_T u_{*s}$.

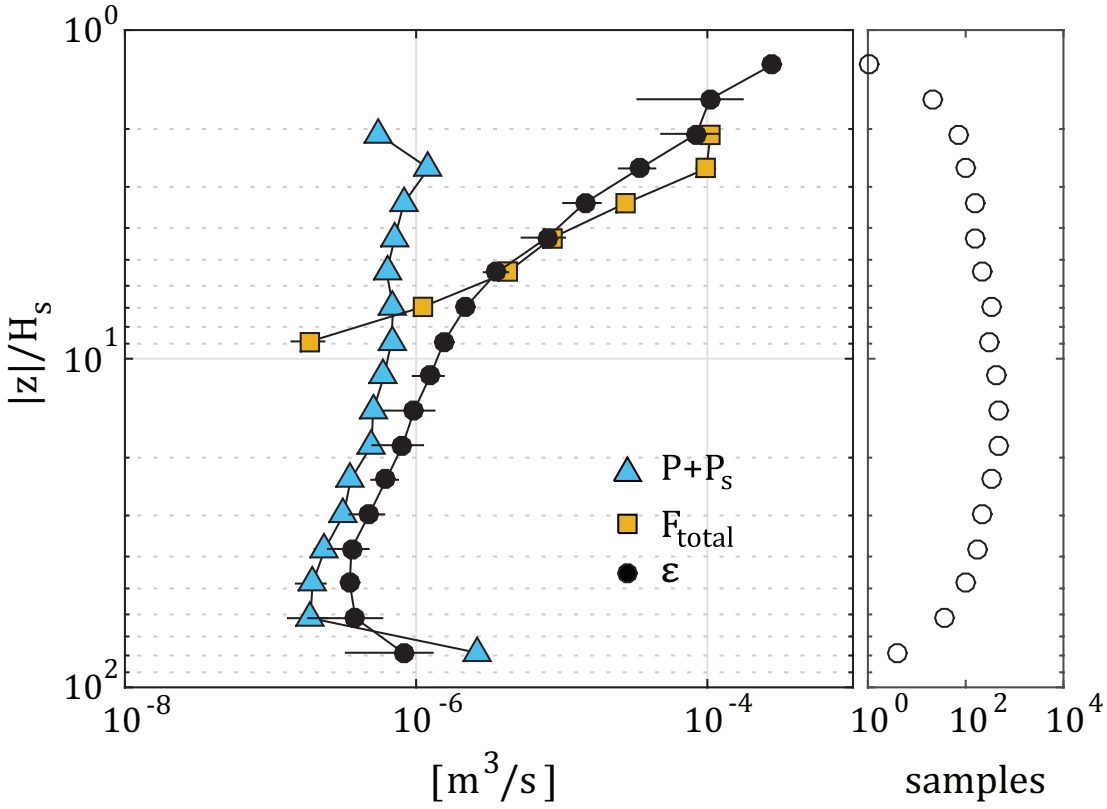

Figure 4.4 Average Turbulent Kinetic Energy Budget. Terms in the TKE budget: (blue triangles) total production (P + Ps), (yellow squares) vertical divergence of total TKE transport, and (c) (black dots) dissipation. Figure adapted from Scully et al (2016).

During the course of the experiment, wave breaking was the dominant source of TKE in the wave transport layer with Langmuir turbulence contributing less than 10% of the surface TKE flux (Figure 4.5). This is similar to the results presented by Jones & Monismith (2008a) for a shallow estuarine environment in Grizzly Bay, CA and consistent with the results of Scully et al (2016) in which the Stokes production term was found to be insignificant compared to the divergence in the TKE flux driven by the pressure work under breaking waves. The Skyllingstad & Denbo (1995) relation does not however, describe the effects of Stokes drift shear in modifying vertical transport regimes within the wave transport layer.

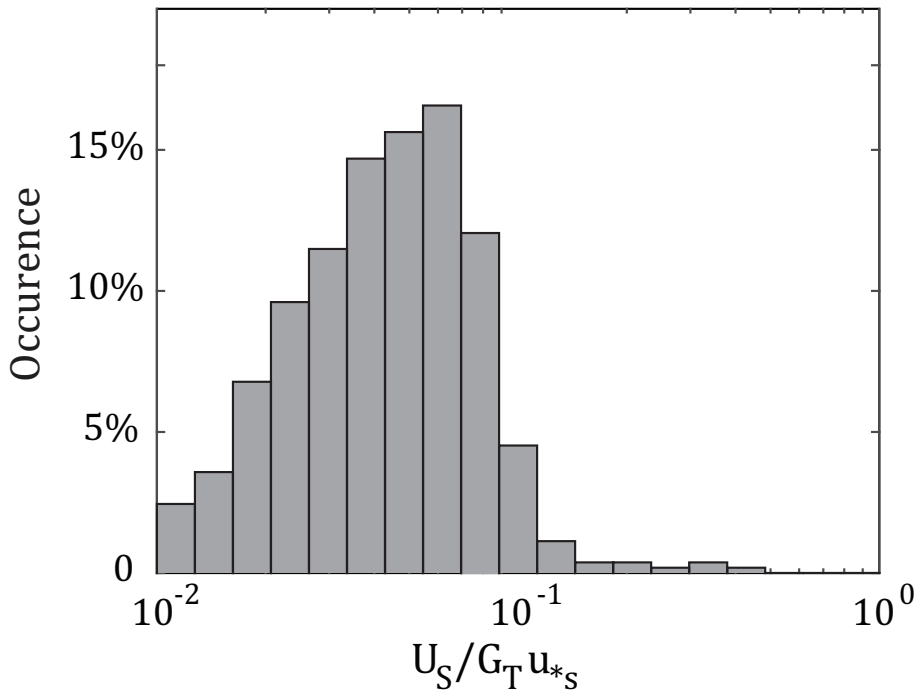

Figure 4.5 Ratio of the surface TKE flux generated by the CL2 vortex force to the TKE flux generated by breaking waves. Wave breaking dominates the surface TKE fluxe with Langmuir turbulence contributing less than 10%.

4.4.3. Dissipation Structure and Scaling

In an energetic, shallow environment like Chesapeake Bay, the distribution of TKE within the water column is dependent on the relative strength of three factors: the surface stress, wave breaking, and the bed stress. The depth at which the wave transport layer transitions to a surface log layer can be found by equating the scaling arguments for a wave transport layer (Eqn 4.2) and a surface log layer (Eqn 4.3), (Terray et 1996, Jones & Monismith 2008a):

$$z_{t1} = -0.3\kappa H_S G_T \qquad (4.18)$$

where $F_0 = G_T u_{*s}^3$, κ=0.41, and H_s is the significant wave height. The base of the wave transport layer occurs at z_{t1} and represents the point at which TKE transported from beneath breaking waves becomes negligible. The observed dissipation profile, scaled by surface log layer scaling, is presented in Figure 4.6. The analytical mean transition depth between the wave transport layer and the surface log layer is shown as a horizontal dotted line.

Within the wave transport layer, dissipation estimates agree well with the conceptual model of Terray et al (1996), but are elevated relative to Terray et al (1996) scaling (Eqn 4.2, thick black line). The transition between wave transport layer and surface log layer occurs at z_{t1} = -4.94 ± 0.09m. While measured dissipation rates exceeded the scaling suggested by Terray et al (1996) within the wave transport layer, the

transition to a surface log layer occurred at the same depth as predicted by Equation (4.18).

In an estuarine environment like Chesapeake Bay, the bottom boundary layer is tidally dominated while the surface log layer is wind-dominated. The gradient Richardson number often exceeded the critical value of 0.25 near the seabed, suggesting that the height of the bottom boundary layer was often restricted by stable stratification. Based on comparison to expected surface log layer scaling, Figure 4.6 demonstrates that the surface log layer extended to a depth of ~ 8.40m ± 0.12m. The mean velocity profile near the bed did not follow a logarithmic profile and dissipation measured at the deepest ADV (~ -11.5m) often exceeded bottom log layer scaling suggesting that a vertical divergence in TKE transport resulting from stable stratification likely played an important role in near-bed TKE dynamics. Characterizing the specific nature of the stratified bottom boundary layer observed during this experiment, however, is beyond the scope of this paper.

The challenges and limitations associated with measuring turbulent dissipation in situ means that observations of multi-layer turbulent response to wind forcing are rare despite being predicted by the analytical solutions of Craig & Banner (1994), Craig (1996), and Burchard (2001). A three-layer structure; consisting of a wave transport layer, a surface log layer, and a stratified bottom boundary layer; dominated the wind-forced response at the tower site with the transition between the wave transport layer and the surface log layer (zt1) being shallower than the depth of the surface log layer for 98% of the observations.

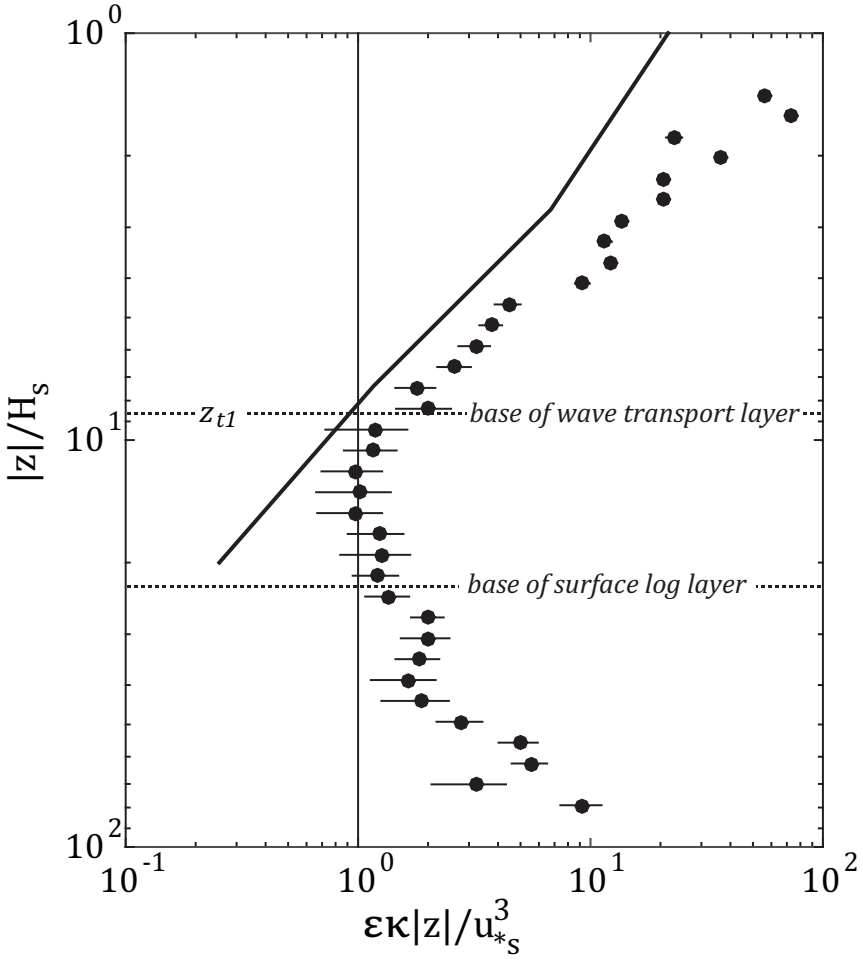

Figure 4.6 Observed profile of dissipation normalized by log layer scaling (Eqn 4.3). Horizontal dotted lines represent transition depths between the wave transport layer, surface log layer, and bottom boundary layer. The average depth of the transition between the wave transport layer and the surface log layer agrees well with the analytical scaling in Equation 4.18 (z_{t1}). Solid black line represents Terray et al (1996) scaling for a wave transport layer. layer.

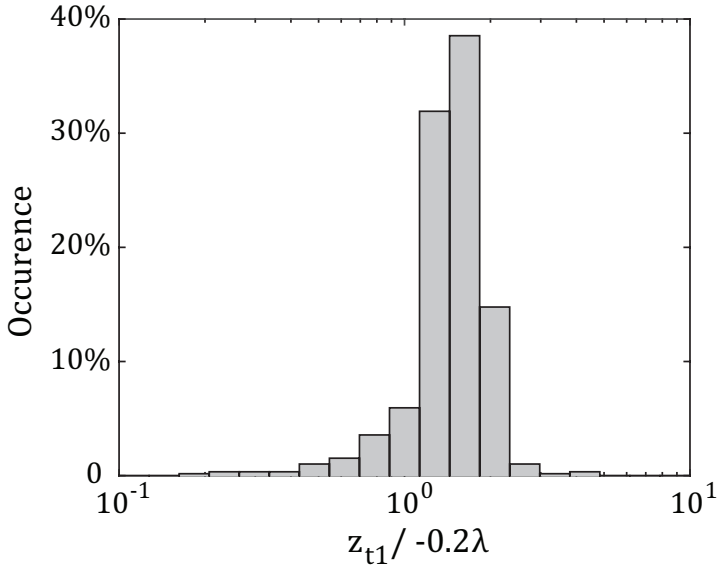

Figure 4.7 Distribution of the ratio of the wave transport layer depth, z_{t1}, to the expected maximum depth of breaking-induced roll vortices (Melville et al 2002, Scully et al 2016). The mean of the distribution is approximately 1.4, which suggests that the depth of the wave transport layer exceeded the maximum depth of penetration of breaking waves.

Scully et al (2016) documented that negative pressure skewness associated with TKE transport driven by pressure work was limited to depths greater than -0.2λ, where λ is the wavelength associated with H_s, which is consistent with the laboratory results of Melville et al (2002) for the maximum depth of penetration of roll vortices generated by breaking waves. The ratio of the observed z_{t1} to -0.2λ is shown in Figure 4.7. The distribution of $|z_{t1}|/0.2\lambda$ had a mean of 1.4, suggesting that wave transport layer extended below the maximum depth of penetration of breaking waves observed during this experiment.

4.4.4. Relationship Between Turbulent Length Scale, Dissipation, and TKE

The relation between dissipation, TKE, and the turbulent length scale (Eqn 4.7) can be used to evaluate the relationship between the stability function and turbulent length scale used in second moment closure schemes. Following Umlauf & Burchard (2003), we assume that the turbulent length scale increases linearly with distance from the boundary such that:

$$l = L|z| \tag{4.19}$$

In an unstratified log layer, L=κ=0.41. In a transport layer, however, L is expected to decrease based on grid stirring experiments and direct numerical simulations of free shear turbulence (Umlauf & Burchard 2003). The modeling studies of Umlauf (2003) and Umlauf & Burchard (2003) suggest that L ~ 0.2 for wave breaking transport modeled as a free shear layer, but field observations which validate this assumption are rare. Jones & Monismith (2008b) found that L = 0.25 was needed to reproduce dissipation rates measured within the wave transport layer using a one-equation closure model with a constant stability function and a z_0=O(H_s).

Combining Equation (4.7) with Equation (4.19), we can evaluate the relation between stability function and length scale growth rate directly using measurements of dissipation and TKE (Gerbi et al 2009):

$$k^{3/2} = \frac{L}{c_\mu^{0(3/4)}}\varepsilon|z| = \Lambda\varepsilon|z| \tag{4.20}$$

Where $\Lambda = L/c_{\mu}^{0(3/4)}$. Gerbi et al (2009) showed that near-surface dissipation and TKE observations collected as part of the CBLAST-LOW suggest that Λ is significantly reduced in the wave transport layer when compared to rigid boundary scaling derived using L=κ and c_{μ}^{0}=0.09.

In Figure 4.8, a scatterplot of TKE and dissipation measured at the top two ADVs (z ~ - 1.7m and z ~ -3.5m) is shown. A linear regression of the data yields a Λ of 1.06, which is consistent with the value reported by Gerbi et al (2009) for the CBLAST-LOW experiment. Assuming a constant stability function, this is consistent with the reduction in length scale relative to rigid boundary scaling that has been reported by previous studies. During large dissipation events, Λ is significantly reduced (0.27) suggesting that either the turbulent length scale is greatly reduced under energetic breaking conditions or that the stability function value is greatly enhanced.

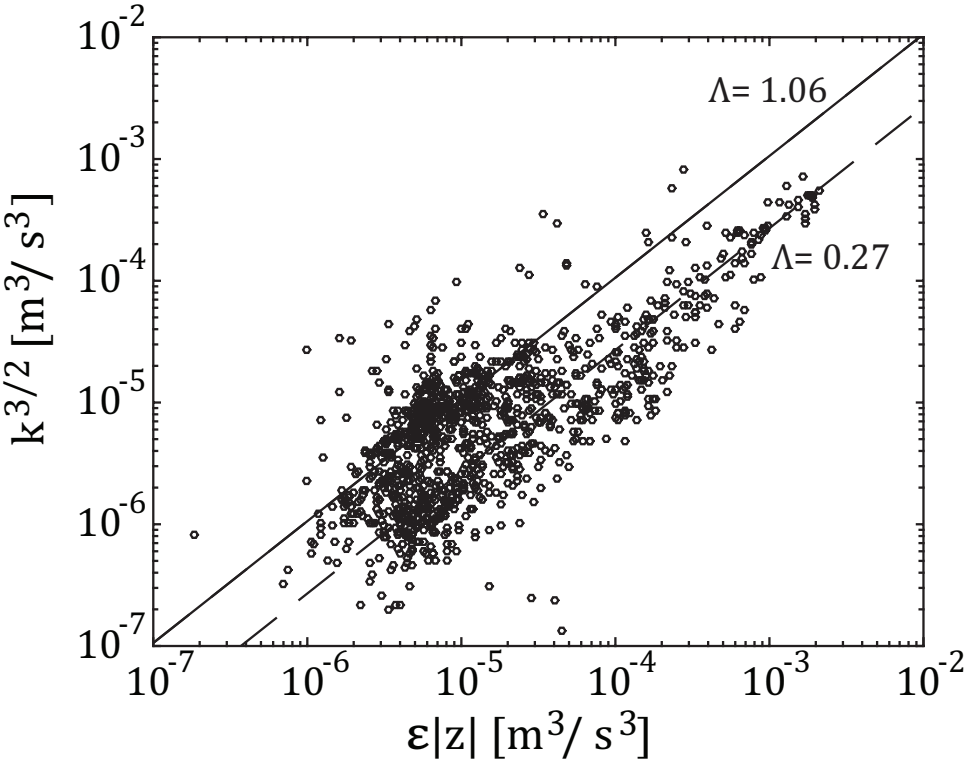

Figure 4.8 Relationship between TKE, dissipation, and the turbulent length scale observed at z >= -3.5. The solid black line represents a linear regression line that yields a Λ value (Eqn 4.21) of 1.06. The dashed line denotes a Λ value associated with the largest dissipation events (Λ =0.27).

4.4.5. Vertical Profile of TKE

Craig (1996) developed an analytical solution for the vertical profile of TKE in the oceanic surface layer through solution of the TKE equation invoking a balance between dissipation, shear production, and vertical divergence of TKE transport. The model was shown to be consistent with the predictions from a full k-ε model (Burchard 2001) and has been used to compare observed energy profiles with model predictions (Gerbi et al 2009, Li et al 2013). Following the notation of Gerbi et al (2009), the Craig (1996) model for TKE can be expressed as:

$$\frac{k^{3/2}}{u_{*_s}^3} = \frac{1}{c_\mu^{0(3/4)}} + G_b \left(\frac{3\sigma_k}{2c_\mu} \right)^{1/2} \left(\left| \frac{z}{z_0} \right| \right)^{-m} \tag{4.21}$$

where,

$$m = \frac{1}{\Lambda} \left(\frac{3\sigma_k}{2c_\mu} \right)^{1/2} \tag{4.22}$$

$G_B u_{*_s}^3$ is the TKE flux into the wave transport layer and σ_k is the turbulent Schmidt number. The first term on the right hand side is the log layer limit (production dominant) and the second term is the wave transport layer limit (divergent TKE transport dominates). It should be noted that the Gerbi et al (2009) form of the Craig (1996) model accounts for a virtual origin at the base of the wave breaking layer as suggested by

Burchard et al (2001) and maintains the distinction between the stability function used in the calculation of the eddy viscosity (c_μ) and a constant stability function assumed for the surface log layer (unstratified, $c_\mu = c_\mu^0 = 0.09$).

Due to uncertainty regarding the proper value of z_0 (Terray et al 1996, Burchard et al 2001, Umlauf & Burchard 2003, Jones & Monismith 2008b, Gerbi et al 2009), we briefly discuss the choice of parameterization used in this paper. The significant mode of wave breaking observed during this experiment was dominant wave breaking at the spectral peak (Fisher et al *in review*). Strong fetch-limitation likely resulted in steep, plunging breaking waves (Rapp & Melville et al 1990), which entrained air to a greater depth than the spilling breakers measured by the wave-following measurements of Gemmrich & Farmer (2004). Given the consistency with the Terray et al (1996) model shown in Scully et al (2016, Figure 4d), the top of the wave transport layer will be taken to be $z_0 = -0.6H_s$ for the remainder of this analysis.

We compare the observed TKE profile to the one-equation model of Craig (1996) using $z_0 = -0.6H_s$, and $\sigma_k = 1$ in Figure 4.9. Following Burchard (2001) and Gerbi et al (2009), we assume that $c_\mu = c_\mu^0$, such that the values of c_μ^0 and L of are constrained by Λ. Furthermore, using the results discussed in section 3d, we evaluate the model for values of c_μ^0 and L that are equivalent to the observed Λ value of 1.06. The observed TKE profile and model predictions for Λ=1.06 are shown in Figure 4.9, along with curves suggested for the CBLAST-LOW experiment and for rigid-boundary scaling (Gerbi et al 2009). The model agrees well with our data when evaluated with a c_μ^0 value of 0.14 and L=0.24 and captures the transition from a wave transport layer to a surface log layer that

occurs at z ~ -10H_s. Increasing TKE near the bed is indicative of the bottom log layer, which is not accounted for in the Craig (1996) model. A value of L=0.24 is consistent with the findings of Jones & Monismith (2008b) and the proposed transport layer scalings of Umlauf & Burchard (2003), however Λ values in our data were significantly lower during large dissipation events suggesting that L and/or c_μ^0 were not constant within the wave transport layer.

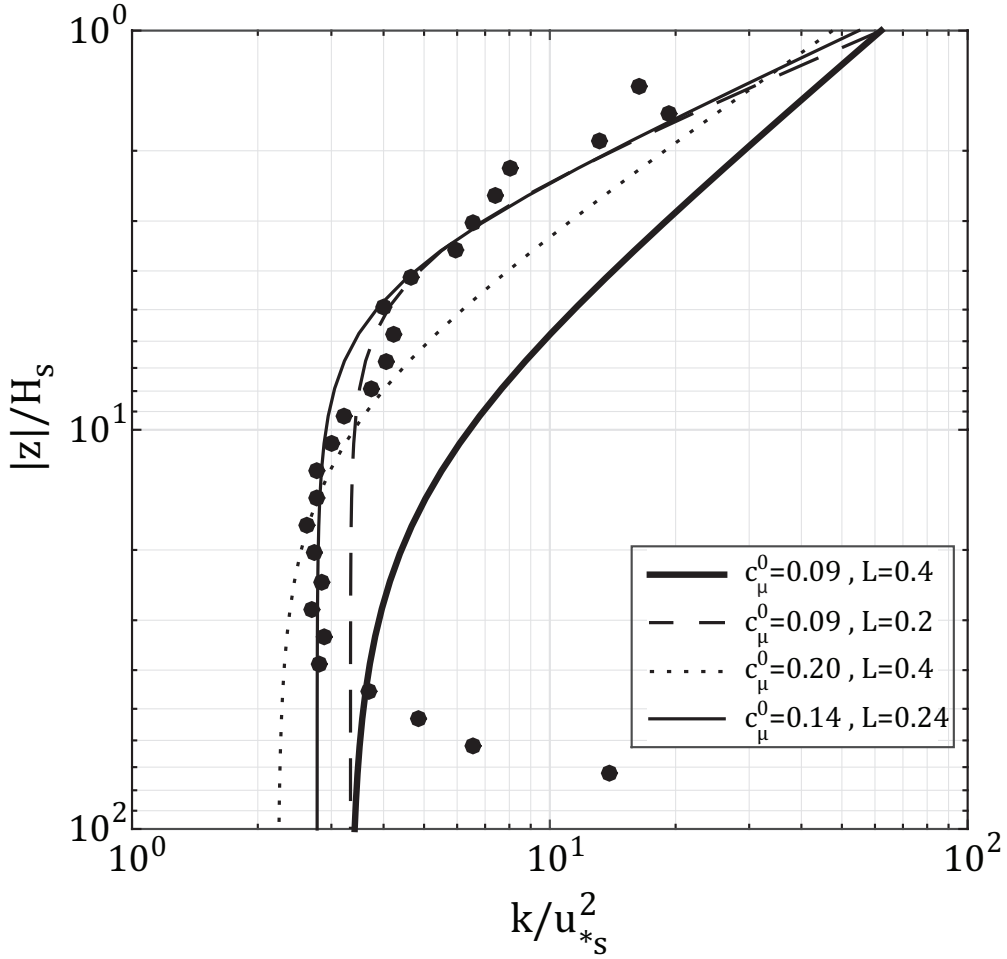

Figure 4.9 Comparison of the observed TKE profile to analytic solutions (Eqn 4.21) of Craig (1996), Burchard et al (2001) and Gerbi et al (2009). Rigid-wall scaling is shown as a thick solid black line. Fits proposed by Gerbi et al (2009) for the CBLAST-Low dataset are shown as dashed and dotted lines. The thin solid black line is a best-fit curve to our dataset using an observed Λ value of 1.06, which corresponds to a constant stability function of c_μ^0 = 0.14 and L = 0.24.

§4.5 Discussion

4.5.1 Observed versus Predicted Stability Functions

Following Scully et al (2011), the value of the stability function can be estimated from Equation (4.9) using observations of TKE, dissipation, stress, and shear: $c_\mu = A_z \varepsilon / k^2 = -\langle u'w' \rangle \varepsilon / \left(Sk^2 \right)$. Measurements of stress, TKE, and dissipation were linearly interpolated between ADV sensor heads to give estimates co-located with shear. To assess the performance of stability functions commonly employed in second moment closure schemes, we compare observed stability function values to those predicted by the nonequilibrium formulations of Kantha & Clayson (1994) derived by Burchard & Bolding (2001) and Canuto et al (2001); referred hereafter as BB01 and CA01, respectively. For a detailed discussion of these nonequilibrium functions, see Burchard & Bolding (2001). Stability function values predicted by BB01 and CA01 were calculated using observed profiles of the momentum flux, mean Lagrangian shear, dissipation, buoyancy frequency, and TKE.

The momentum flux vector measured in the wave transport layer during this experiment was aligned with the mean direction of the Lagrangian shear suggesting that Stokes drift likely altered vertical transport regimes (Fisher et al *in review*). We therefore chose to calculate the eddy viscosity from the mean Lagrangian shear, $-\langle u_i'w' \rangle = A_z \left(\partial U_i / \partial z + \partial U_{Si} / \partial z \right)$, to account for the observed wave-driven steering of the marine stress vector away from applied wind forcing (Scully et al 2016, Fisher et al *in review*). Within closure frameworks, this Lagrangian formulation of the eddy viscosity does not explicitly account for pressure strain relationships that can lead to enhanced vertical transport driven by Langmuir turbulence as discussed in Harcourt (2013) and Harcourt (2015).

Predicted and observed stability function values, bin-averaged by mean depth, are shown in Figure 4.10. A constant stability function value does not represent this dataset well as observed stability function values ranged over two orders of magnitude. Within the wave transport layer, results indicate that observed c_μ values ranged from $O(10^{-2})$ to O(1) with a mean value of 0.74, which significantly exceeds free shear limits often employed in closure schemes (Umlauf & Burchard 2003). The inclusion of the Stokes drift shear in the calculation of A_z reduces its value near the surface, so the dramatic increase of c_μ beyond typically assumed free shear limits within the wave transport layer is not solely the result of the Lagrangian formulation of the eddy viscosity.

The formulation of BB01 produces less scatter and performs slightly better than CA01 when compared to observations. While both models reproduce low stability function values reasonably well, they significantly underpredict large observed stability

function values. Both parameterizations include an empirically determined free shear limit, ~0.16 (BB01) and ~0.11 (CA01), which results in the asymptotic solutions shown in Figure 4.10. This underprediction is likely rooted in the fact that grid-stirring experiments are commonly used to calibrate stability functions for free shear conditions, which do not account for the enhanced vertical transport scales generated beneath surface gravity waves due to Langmuir turbulence and/or wave breaking.

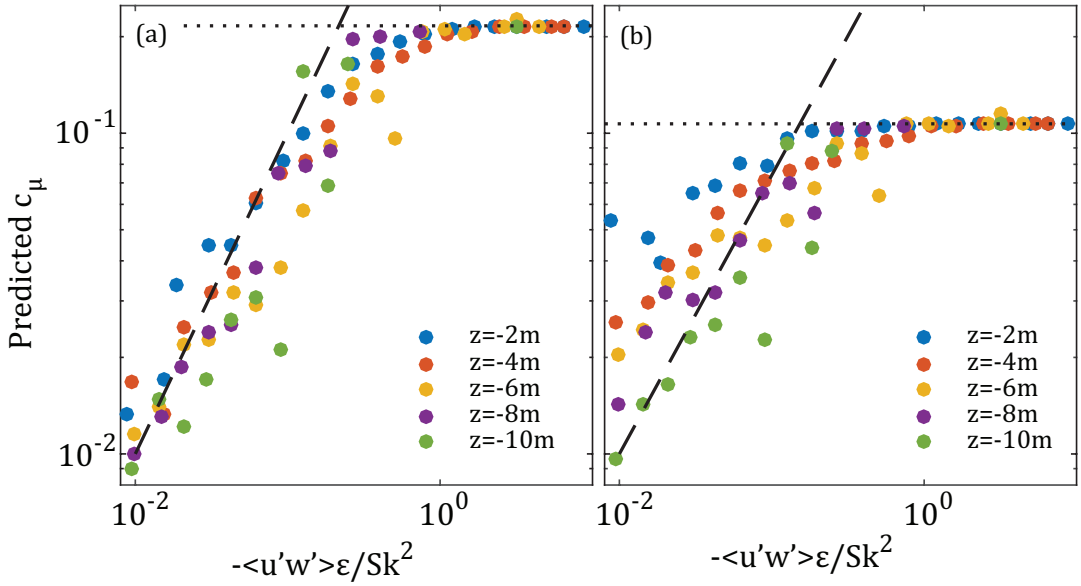

Figure 4.10 Bin-averaged comparison of predicted stability functions and observed stability functions. (a) Kantha & Clayson 1994 rederived by Burchard & Boulding 2001 (BB01). (b) Canuto et al 2001 (CA01). Dotted lines are model asymptotes in free shear conditions. In wave-affected surface layer, observed stability functions greatly exceed empirical asymptotes and can be O(1).

Using observed Λ and stability function values in Equation (4.20) yields an average L=0.20, which is consistent (though slightly smaller) with the model fit for the TKE profile presented in Figure 4.9 and the modeling results of Umlauf & Burchard (2003). This indicates that within the wave transport layer, the transport of TKE is carried out by eddies smaller than those responsible for shear production next to a rigid boundary. The assumption of a turbulent Schmidt number of $\sigma_k = 1$, may therefore not be an appropriate assumption for turbulence generated beneath breaking waves.

Because the only difference between predicted and observed eddy viscosities was the value of c_μ, a comparison of predicted eddy viscosity to observed eddy viscosity (Figure 4.11) demonstrates the impact of underpredicting the ratio of stress to TKE in the wave transport layer. Both CA01 and BB01 show strong agreement for $|z| > 7H_s$ where stable stratification limited turbulent length scales and shear production became more dominant. However, both nonequilibrium formulations underpredict (by nearly an order of magnitude) the eddy viscosity observed under breaking waves. This indicates that the presence of breaking waves homogenized the surface mixed layer to a greater extent than predicted by the classical model of TKE diffusing away from a source at the surface.

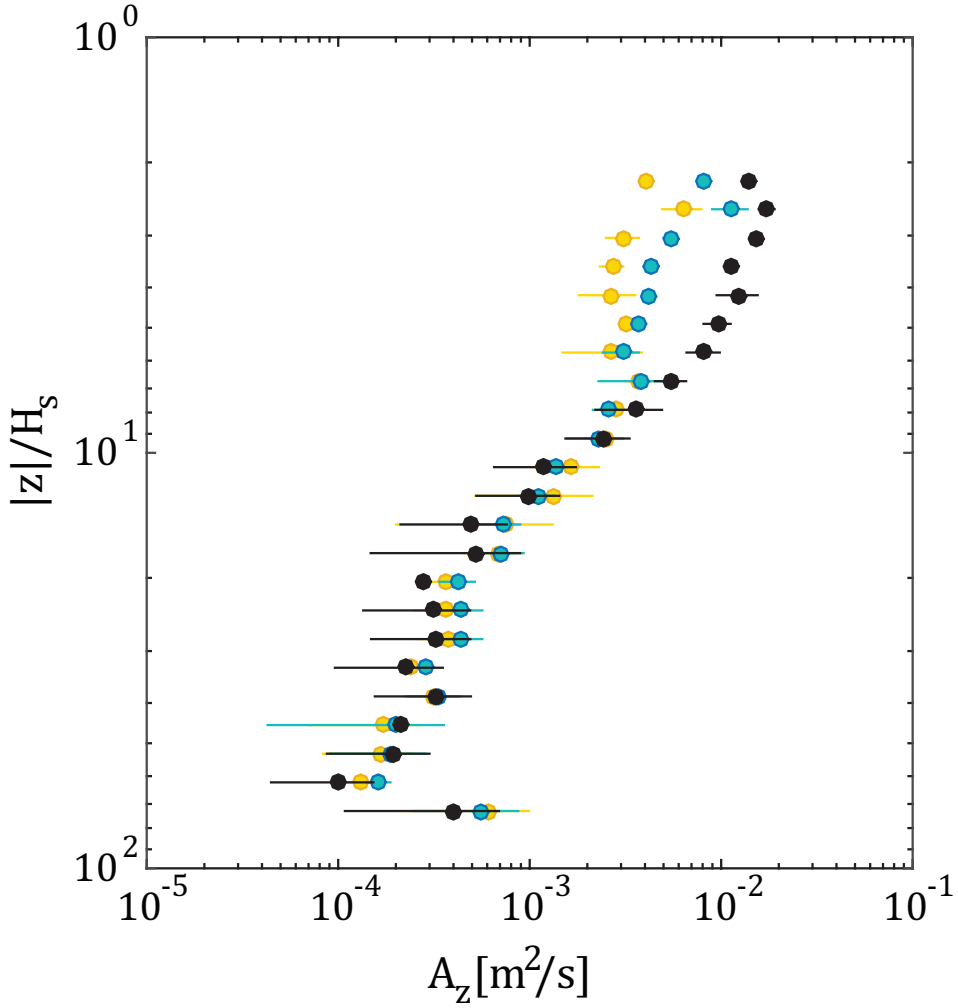

Figure 4.11 Comparison of predicted (blue - BB01, yellow - CA01) and observed (black) profiles of eddy viscosity shown with standard error bars. The asymptotic behavior of predicted stability functions results in a significant underprediction of eddy viscosity in the wave-affected surface layer.

4.5.2 Turbulent Length Scales

As discussed in section 4.2.3, turbulent length scales provide a useful framework for evaluating the relative importance of boundary versus stability-limited turbulent mixing. We compare the master turbulent length scale (Eqn 4.7) to the observed Prandtl mixing length, which was calculated from Equation (4.15) using measurements of shear and stress, in Figure 4.12. Also shown are the mean observed Ozmidov scale (Eqn 4.14) and a boundary layer scaling (l_{WBL}) that has been modified for the effects of wave breaking:

$$l_{WBL} = L|z|\sqrt{1-\frac{|z|}{h_{bl}}} \qquad (4.23)$$

where L=0.20, and h_{bl} is taken to be the top of the bottom boundary layer. The vertical coordinate in Figure 4.12 has been adjusted to the depth relative to the base of the assumed active breaking layer ($|z-z_0|$) to reflect the growth of turbulent eddies beneath a surface source of TKE in accordance with Craig & Banner (1994), Burchard (2001), and Umlauf & Burchard (2003). Results indicate that stratification controls turbulent length scale at depths of $|z| > 7Hs$ and that within this buoyancy-controlled region the master length scale relation accurately reproduces the observed Prandtl mixing length. The transition between stratification-limited conditions and boundary-limited conditions occurs at a mean depth of $|z| \sim 7H_s$ shown as the intersection between the mean Ozmidov length scale and the modified boundary layer scaling.

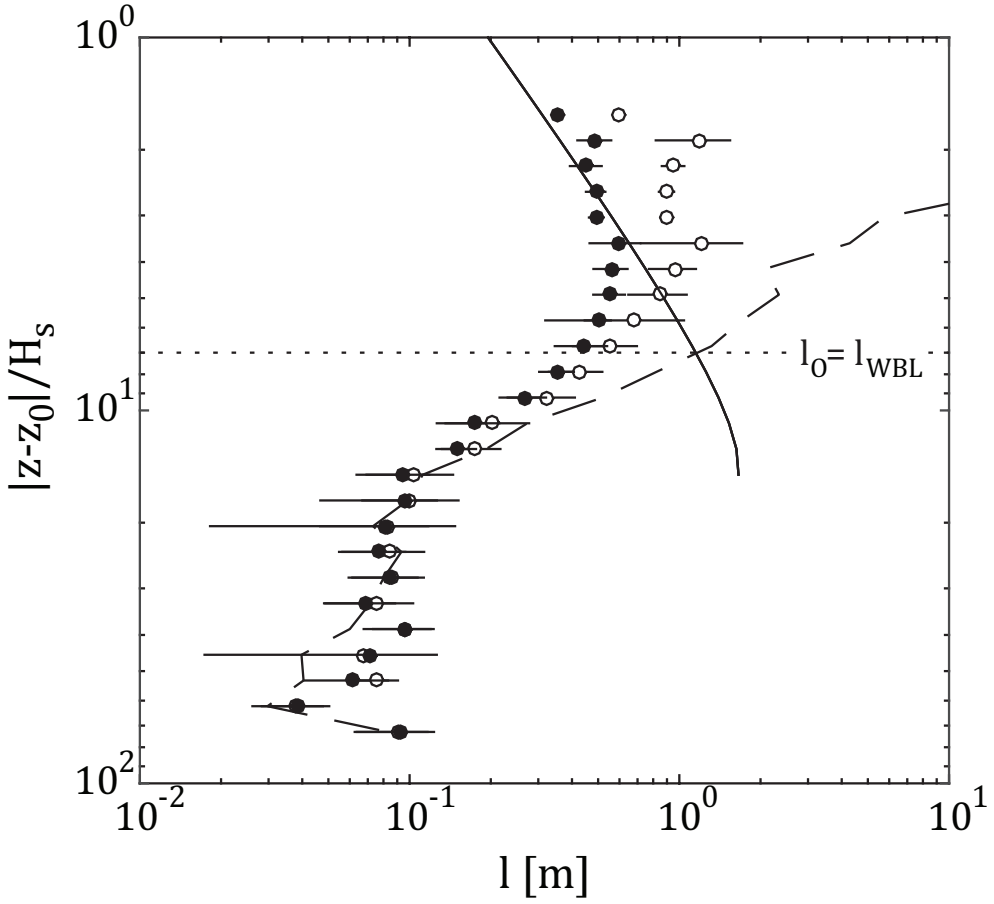

Figure 4.12 Comparison of the observed profiles of the Prandtl mixing length (white dots, Eqn 4.15) and the master length scale of turbulence (black dots, Eqn 4.7) calculated from observed stability function values, TKE, and dissipation rates. A boundary layer scaling modified for wave breaking (Eqn 4.23) is shown as a solid black line and the mean observed profile of the Ozmidov scale (Eqn 4.14) is shown as a dashed line. Within the wave transport layer, the observed Prandtl mixing length is larger than the TKE transport scale. In the buoyancy-controlled region, Eqn (4.7) accurately predicts the observed Prandtl mixing length, which is limited by stratification.

Because a divergence of the total TKE transport balances dissipation within the wave transport layer, the master length scale is equivalent to the TKE transport scale within the surface mixed layer. At depths shallower than $|z| \sim 7H_s$, a divergence occurs between the Prandtl mixing length and the TKE transport length scale. The observed Prandtl mixing length is larger than the TKE transport scale and remains relatively constant at 1m. This is consistent with the cospectral analysis of the pressure work, TKE flux, and momentum flux presented in Scully et al (2016), which showed that the spectral peak in momentum flux occurred at smaller wavenumbers than the spectral peaks of the TKE transport terms. While observed Λ and c_μ^0 values suggest that the TKE transport length scale increases linearly away from the surface boundary such that L=0.20, the ability to directly compare profiles of the TKE transport length scale and boundary-limited scaling is restricted by our data coverage.

Enhanced length scales and coherency of eddies within the wave-affected surface layer are often associated with Langmuir turbulence where the CL2 vortex force generates coherent eddies with length scales that are similar to the depth of the surface mixed layer (Harcourt & D'Asaro 2008, Grant & Belcher 2009, Harcourt 2013). However, for a mean significant wave height of ~0.5m observed during the experiment, $|z| = 7H_s$ corresponds to a mean depth of z ~ -3.5m, such that the observed constant Prandtl mixing length of l_M=1 is not consistent with depth-filling coherent Langmuir cells.

Between $5Hs < |z| < 11Hs$, the nondimensional stress takes the form of a hyperbolic secant function (Figure 4.13), which Scully et al (2011) show can be used to describe the vertical profile of stress in a stratified free shear layer. The subsurface

maxima in nondimensional stress coincided with the depth at which $l_O=l_{WBL}$ and the depth limit of breaking events ($z= -0.2\lambda$), which suggests that enhanced shear-driven mixing occurred at the base of the surface mixed layer. As shown by Scully et al (2011), TKE transport within a shear layer may comprise a significant portion of the TKE budget. Within this region of enhanced shear, the observed Prandtl mixing length was slightly less than the Ozmidov scale. Because the Ozmidov scale implicitly assumes a $P +B = \varepsilon$ balance (Dillon 1982) for energetic flows, the authors hypothesize that this slight difference is likely due to the effective transport scale being reduced by nonlocal TKE production. Taken together, Figures 4.12 and 4.13 suggest that wave breaking eroded vertical stratification and reduced near surface shear sufficiently within the wave transport layer to allow for a separation in TKE and momentum transport regimes.

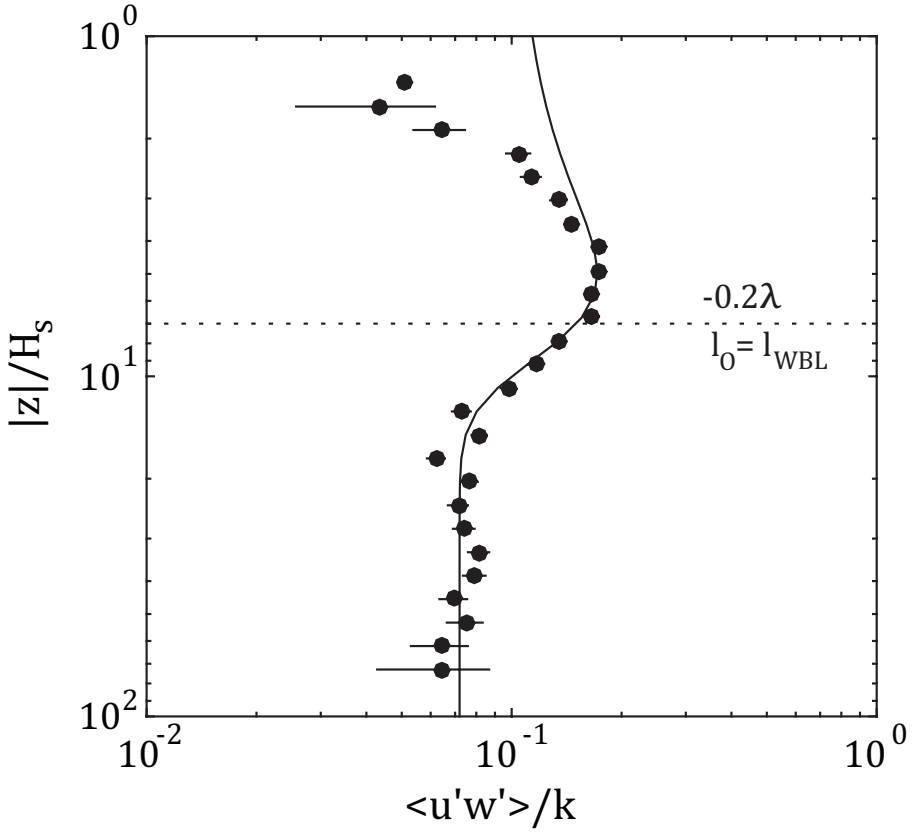

Figure 4.13 Observed mean profile for nondimensional stress shown with standard error bars. The horizontal dashed line represents the average depth where the Ozmidov scale equals surface boundary layer scaling (l_O=l_{WBL}) and the depth of breaker roll vortices (-0.2λ). The subsurface maxima is consistent with enhanced stress due to enhanced shear at the base of the surface mixed layer as evidenced by the agreement with the expected form of a stratified shear layer (black line, Scully et al 2011).

4.5.3 Wave Breaking vs. Langmuir Turbulence

The modeling results of Melsom & Sætra (2004) suggest that shear production is only important episodically during breaking events, which provides a conceptual link between diffusive breaking models and intermittent breaking events (Umlauf & Burchard 2005). Conditional averaging of ADV burst data indicates that TKE transport carried out by pressure work associated with breaker roll vortices was associated with upward vertical velocities while the momentum flux was associated with downward sweeps of high velocity fluid (Scully et al 2016). This suggests that the momentum flux and the TKE transport may have been carried out by different classes of turbulent eddies within the wave transport layer.

A sample time series of the instantaneous momentum flux (panel a) and pressure work (panel b) observed at the uppermost ADV shows apparent independent sweeps of high momentum fluid that were unaccompanied by an instantaneous spike in pressure work (Figure 4.14). Two significant downward sweeps of momentum occurred early in the record that did not have a corresponding breaking eddy signature (e.g. spike in pressure work). Rapp & Melville (1990) demonstrated that as much as 25% of the total air-sea momentum flux could be attributed to plunging breaker events, but the laboratory experiments of Melville et al (2002) showed that despite breaker roll vortices reaching depths of -0.2λ, the momentum flux associated with breaking impulses was quite small.

It has generally been documented that surface gravity waves enhance vertical kinetic energy in the surface layer relative to rigid boundary scaling, but observational constraints make isolating the effects of breaking and Langmuir turbulence difficult (D'Asaro 2001, Tseng & D'Asaro 2004). Using the impulse formulation of breaking

waves suggested by the laboratory results of Melville et al (2002), Sullivan et al (2007) conducted a series of LES simulations that sought to isolate the effects of wave breaking and Langmuir turbulence on mixed layer properties. The results of Sullivan et al (2007) suggest that vertical velocity variance is greatly enhanced by the CL2 vortex force mechanism beyond that simulated for a rigid boundary or a pure wave-breaking scenario.

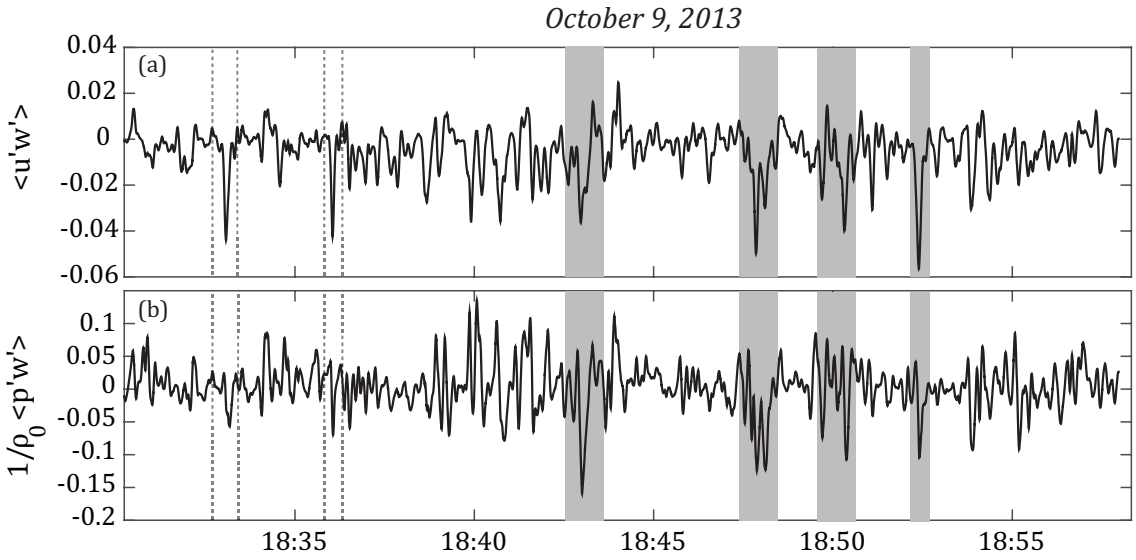

Figure 4.14 Sample plot of the (a) instantaneous momentum flux and (b) pressure work observed on October 9, 2013. Shaded regions represent periods of strong correlation between TKE transport and momentum flux, while dashed lines indicate periods when downward momentum sweeps occur without a corresponding breaking eddy signature.

In Figure 4.15, the average vertical velocity variance profile observed in the surface mixed layer, defined as $z >= z(l_O=l_{WBL})$, are shown with the observational results of Hinze (1975) for a rigid boundary (note that a similar figure was shown in Scully et al 2015) and LES results of Sullivan et al (2007) for a breaking-Langmuir scenario and a pure breaking scenario. The observed profile of vertical velocity variance within the surface mixed layer is very similar to the modeling LES results for a wave breaking-Langmuir regime, with variances greatly enhanced relative to that expected for a rigid boundary or a pure wave breaking case. The results are also consistent with field observations of D'Asaro (2001), which show enhanced vertical velocity variance (Scully et al 2015).

Conducting simulations for a range of breaking intensities, Sullivan et al (2007) determined that energetic breaking reduced the coherency of Langmuir cells. Energetic breaking events disrupted Langmuir turbulence and resulted in strong, localized downwelling jets that were strained by the CL2 vortex force into a patchy distribution of intensified vertical vorticity (Sullivan et al 2007). This picture is consistent with the observations presented here, where strong fetch-limitation results in the dominant mode of wave breaking occurring at the spectral peak (Fisher et al *in review*), which likely produced plunging breakers (Rapp & Melville 1990) that dominated TKE transport near the surface (Scully et al 2016).

While not exhaustive, these results in combination with the observed agreement between the Lagrangian shear direction and the stress direction (Fisher et al *in review*) suggests that the CL2 mechanism influenced momentum exchange during periods of active wave breaking. The authors hypothesize that the momentum flux observed during

the experiment was likely not driven solely by wave breaking, but rather that the combined mechanism of Langmuir turbulence and wave breaking controlled momentum transfer in the wave transport layer.

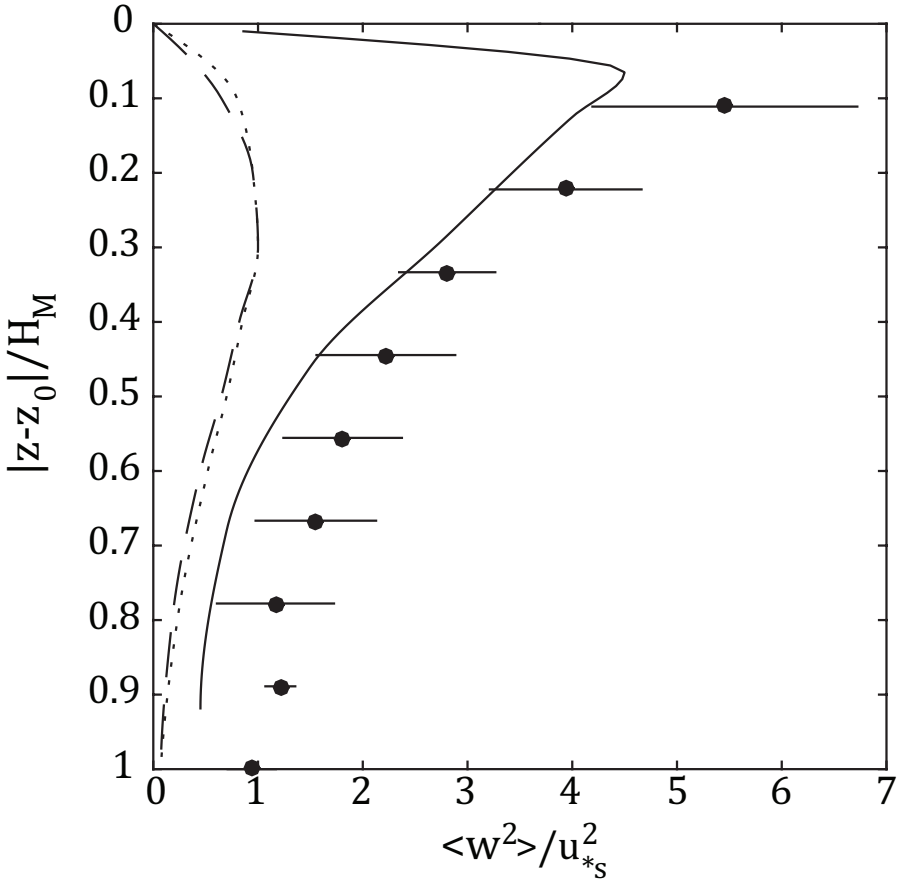

Figure 4.15 Comparison of normalized vertical velocity variance within the surface mixed layer (black dots) to the LES modeling results of Sullivan et al (2007). H_M is the depth at which $l_O = l_{WBL}$ and z_0=-0.6H_S. The solid black line represents simulation results that included wave breaking and Langmuir turbulence. The dashed line represents a pure wave breaking scenario. Also shown is the observational rigid boundary scaling (dotted line) from Hinze (1975). Figure adapted from Scully et al (2015).

§4.6 Conclusions

Direct observations of dissipation, TKE and stress indicate that breaking waves dominated the structure of turbulent transport within the oceanic surface boundary layer of Chesapeake Bay. During periods of active wave forcing, a three-layer turbulent response was detected in which the wave transport layer transitioned to a surface log layer ($z \sim -10H_s$), which then merged with the tidal, bottom boundary layer. The depth of the transition between the wave transport layer and the surface log layer agreed well with the analytical scalings suggested by Terray et al (1996) and Jones & Monismith (2008a).

Within the wave transport layer, elevated dissipation rates in agreement with Terray et al (1996) scaling were balanced by the divergence in the total TKE transport. Breaking waves dominated the TKE budget within the wave-affected surface layer contributing over 90% of the surface TKE flux. As assumed in most closure models, the dissipation rate and TKE were related through a length scale proportional to the distance from the surface boundary. However, this proportionality coefficient was determined to be less than half that expected for turbulence produced near a rigid boundary and was not constant during the experiment. A comparison of the base of the wave transport layer to the maximum depth of negative pressure skewness, which corresponded to energetic breaking events (Scully et al 2016), indicates that the wave transport layer extended below the maximum depth of roll vortices generated beneath breaking waves.

The one-equation closure model of Craig (1996) model, modified by Burchard (2001) & Gerbi et al (2009), agreed well with the measured average profile of TKE when applied using a constant stability function value of c_μ^0=0.14 and surface length scale

growth rate of L=0.24. However, stability function values calculated from time series of observed TKE, stress, shear, and dissipation ranged over two orders of magnitude and greatly exceeded the maximum values of two commonly used nonequilibrium formulations within the wave transport layer. As a result, both nonequilibrium stability function formulations significantly underpredicted observed eddy viscosities in the wave transport layer. Within the buoyancy-controlled interior, both parameterizations performed well and accurately predicted observed mixing profiles.

Horizontal buoyancy gradients in Chesapeake Bay likely resulted in a restratifying flux that resisted vertical wind-driven mixing and maintained a buoyancy-limited turbulent regime in a significant fraction of the water column during periods of energetic wave breaking. A subsurface peak in nondimensional stress at the transition between boundary- and buoyancy-limited turbulence indicated that within the wave transport layer, wave-driven mixing likely resulted in a two-layer sheared flow. This region of enhanced shear coincided with the maximum depth of breaker rolls vortices, suggesting that breaking waves were the primary driver of vertical stratification erosion.

Analysis of the observed Prandtl mixing length and the master turbulent length scale (Tennekes & Lumley 1972) estimated using TKE, dissipation, and observed stability function values indicated that within the wave transport layer, the momentum flux and the transport of TKE were likely carried out by different classes of eddies. The observed Prandtl length was nearly constant within the boundary-limited region of the wave transport layer and was larger than the length scale associated with TKE transport.

Coherent structures characterized by enhanced vertical turbulent velocity likely dominated momentum transfer within the wave transport layer. Analysis of the

instantaneous pressure work and momentum flux showed periods when downward sweeps of high velocity fluid were unaccompanied by a corresponding breaking eddy signature. While breaking waves controlled the surface TKE flux, the authors hypothesize that the CL2 vortex force mechanism enhanced vertical transport regimes in a manner consistent with Langmuir turbulence that is disrupted by energetic wave breaking. These results suggest that wave breaking was the primary driver in eroding vertical stratification, reducing shear and density stratification sufficiently to allow coherent structures consistent with Langmuir turbulence to homogenize the surface layer beyond that predicted by the simple model of TKE being transport away from a source at the surface.

The transfer of momentum and mechanical energy beneath breaking waves has important implications for mixing in the coastal ocean. Recent observations of pressure work dominating TKE transport beneath breaking waves (Scully et al 2016) highlight the need to incorporate pressure work into closure models used in simulating wave-affected surface layers. Underpredictions of the eddy viscosity within the surface layer suggest that current modeling efforts could benefit from further research into the form and nature of turbulent transport carried out by coherent structures beneath breaking waves.

§4.7. Acknowledgements

This manuscript benefited greatly from the comments and suggestions of two anonymous reviewers. This work was supported by National Science Foundation Grants OCE-1061609 and OCE-1339032. UMCES contribution no. XXXX.

CHAPTER 5

CONCLUSIONS

§5.1 Research Conclusions

Using a combination of numerical simulations and direct field observation, this dissertation investigated the role of surface gravity waves in structuring vertical fluxes of momentum and energy that drive wind-driven flows in Chesapeake Bay. The findings and conclusions of this work are applicable to many environments where the growth of wind-waves is limited by the proximity to shore, including regions of the inner shelf and large lakes. A summary of major research findings is outlined below.

WIND STRESS DYNAMICS

Observations of the atmospheric turbulent momentum flux collected by an ultrasonic anemometer show a clear interdependence between wind stress and the surface wave field. Using wave-age and wave-slope formulations of Charnock's alpha, a parameterization of turbulent roughness due to surface waves, our observations suggest that accounting for surface wave effects can reduce the bias of bulk wind stress predictions to below 5%. Additionally, spatial distributions of wind stress calculated from numerical wave model simulations show that the 10 meter neutral drag coefficient can vary by as much as a factor of 2 over the extent of Chesapeake Bay due to variable wind and wave conditions. Modeled alpha values exhibit a clear transition from open-ocean conditions over the shelf to highly variable, fetch-limited conditions within the estuary. Comparisons to a wind-speed dependent drag formulation suggest that wave effects can affect wind stress by up to 20% within the Bay.

Surface Wave Effects on the Translation of Wind Stress Across the Air-Sea Interface

Anisotropic fetch-limitation in Chesapeake Bay results in the propensity for wind waves to align with the dominant fetch axes of the Bay and be persistently and commonly misaligned with wind forcing. Measurements of the momentum flux vector above and below the air-sea interface revealed that within the middle reaches of Chesapeake Bay, the stress in the surface layer of the estuary was misaligned with the atmospheric wind stress. Using interaction stress theory (Hasselmann 1971), the effects of surface gravity waves were examined within the context of the air-sea momentum budget. Horizontal divergence in geographic wave energy transport can result in the surface wave field storing a significant fraction of the total wind stress (up to 40%) when winds blow across dominant fetch axes. Accounting for surface gravity waves was needed to close the momentum budget between the wind and the mean flow. It was hypothesized that coherent wave-driven turbulence drove stress dynamics in the upper water column, steering the marine stress vector away from applied wind forcing and into the direction of the mean surface Lagrangian shear.

Wind-Wave Effects on Estuarine Turbulence

Using observations collected using an instrumented, stationary tower, turbulent profiles generated beneath breaking waves were compared to second-moment turbulence closure predictions. As documented by several other studies, dissipation rates greatly exceeded log-layer scaling within the wave transport

layer and were balanced by the divergence of the vertical transport of turbulent kinetic energy. Turbulent profiles at the tower site were dominated by a three-layer response that consisted of a wave transport layer, a surface log layer, and a stratified bottom boundary layer. Within the surface mixed layer, measured eddy viscosities greatly exceeded the predictions of two non-equilibrium turbulence closures commonly employed in estuarine circulation modeling, indicating that breaking waves homogenized the surface mixed layer to a greater extent than predicted by a simple model of TKE being transport away from a source at the surface. Wave breaking determined the depth of the surface mixed layer and eroded vertical stratification and shear sufficiently for a departure to occur between the Prandtl mixing length and the length scale of TKE transport. Observations suggest that the Prandtl mixing length was significantly larger than the TKE transport scale within the wave affected surface layer and was relatively constant over the depth of the surface mixed layer. Elevated vertical turbulent velocities and a comparison of the instantaneous momentum flux to the instantaneous pressure work suggest that coherent wave-driven turbulent eddies, consistent with Langmuir turbulence, likely dominated momentum transfer in the wave transport layer.

Collectively, these results describe the dynamic control that surface waves exert on air-sea momentum transfer in an estuarine environment. Ranging from regulating wind stress at the water surface to controlling vertical mixing within the water column; surface waves are a significant component of the coastal ocean's response to wind

forcing. This dissertation built upon previous studies of wind-wave-stress dynamics and wave-driven mixing to illuminate several areas of future research needs regarding the impact of surface gravity waves on coastal hydrodynamics.

§5.2 Future Research Directions

Outlined below, are a few topics that would benefit from further research based on the findings of this dissertation. Many of the topics below are immediately relevant to questions surrounding the fate and function of ecosystems within the Chesapeake Bay and other estuaries around the world.

5.2.1 Estuarine Circulation Dynamics

The spatiotemporal variability of wind stress may represent an important caveat of wind-forced estuarine circulation, which has significant implications for material exchange in coastal ecosystems. While the results presented in Chapter 2 and Chapter 3 suggest that stress development at the water surface is highly variable within a coastal embayment, the impact of this spatiotemporal variability on the integrated circulation response of an estuary to wind forcing remains an open question. By using coupled wave and circulation models, such as COAWST (Warner et al 2010), forced with wave-dependent stress formulations and realistic surface wind fields, the importance of fetch-limitation and complex wind fields to scalar exchange within estuaries could be examined. Comparing model runs that include waves to those that do not, would provide

a direct assessment of the potential for the impact of wave-dependent stress on larger-scale circulation features.

Modification of standard turbulence closures to include the effects of surface gravity waves represents another important area of future research in estuarine circulation modeling. Investigations of wave-enhanced mixing on estuarine momentum balances and salt balances would provide valuable insights into the nature of how transient wind-wave-driven mixing impacts wind-driven flows in estuaries. Additionally, the implications of wave-driven mixing for the exchange of oxygen, sediments, and nutrients may be profound considering the role of wind in structuring scalar transport in estuaries. Finally, enhanced transport scales beneath breaking waves can impact several biophysical interactions (e.g. air-sea gas exchange, autotrophic primary production, zooplankton grazing, larval dispersal, and/or benthic-pelagic coupling) suggest that modeling wave-driven turbulence within coupled physical-biogeochemical simulations could address several aspects of how wind and waves affect the ecological functioning of an estuary.

5.2.2 Wave Energy & Momentum Transmission

The results of Chapter 3 indicate that the surface wave field acts as a regulator of momentum exchange between the air and the coastal ocean. Once stored in the wave field, when and where does this wave energy dissipate? What are the implications of wave energy and momentum transmission within the surface wave field for the momentum and energy balances of the mean flow? While numerical wave models are an appealing tool to use in answering these questions, the empirical formulations of wind energy input and dissipation introduce large uncertainities regarding the balance between

the atmospheric wind stress and the stress in the oceanic surface layer. However, these questions could be addressed using high-resolution observational arrays of stress above and below the water surface in combination with a numerical model to isolate the effects of wave energy transport divergence on larger-scale momentum budgets. Because storage within the wave field is expected to occur when winds blow across dominant fetch axes, the potential of significant mean flow impacts are likely greater for lateral circulation than axial circulation.

5.2.3 Turbulence Closure

The results of Chapter 4 indicate that breaking waves dominate the transfer of energy and momentum within the surface mixed layer and that standard turbulence closure assumptions can substantially underpredict the eddy viscosity in the wave transport layer. Until quite recently (Scully et al 2016), direct observations of pressure work were unavailable and its role in the TKE budget beneath a wavy free remained uncertain. As such, nearly all turbulence closure schemes do not include pressure work in empirical relations that are used to describe turbulent dynamics in circulation models. Future research into methodologies for parameterizing coherent eddies near the free surface would greatly benefit our ability to model the effects of breaking waves within coastal circulation simulations.

The apparent separation between momentum and TKE transport scales within the wave-affected surface layer prompts future analysis of the turbulent Schmidt number (Sc) beneath breaking waves. While often assumed to be equal to 1 in turbulence closure models, the results of this experiment and other numerical modeling discussions (e.g.

Burchard 2001) suggest that there is no clear evidence to support the assumption of Sc=1 within a wave transport layer.

Finally, a major challenge in implementing a closure framework similar to that outlined in Chapter 4 within a circulation model is the prescription of a constant dissipation layer of depth z_0. Further work is needed in formulations of z_0 that could be calculated based on the outputs of a numerical wave model. This includes continuing the ongoing effort of parameterizing deep-water wave dissipation and future work into methodologies for near-surface direct observation.

5.2.4 Structure of Wave-Driven Turbulence

Much of our current understanding of the turbulent structure beneath breaking waves comes from large eddy simulations and laboratory studies that are limited in their representation of a realistic oceanic surface boundary layer. With the growing availability of autonomous underwater vehicles and surface observational platforms, opportunities for fine-scale observations of wave-controlled coherent turbulence are becoming more possible. Observations of the structure and nature of turbulence beneath breaking waves could shed light on the coupling of wave breaking and Langmuir turbulence, as well as inform turbulence models used in the formulation of second-moment closure schemes. Furthermore, these platforms could collect additional data that would provide information on the impact of wave-driven turbulence on near-surface heat and scalar exchange.

APPENDIX A

DEVELOPMENT OF A KRIGED WIND FIELD

To examine the impacts of fine scale variations in the surface wind field, a universal kriging scheme was developed to optimally interpolate a 10 meter neutral field derived from 65 stations in and around Chesapeake Bay. Over-land stations were adjusted to 10 meter conditions using a standard power law:

$$U_z = U_{ref}\left(\frac{z}{z_{ref}}\right)^{1/7} \qquad \text{(A1)}$$

where U_z is the wind speed at height z and U_{ref} is the wind speed at some reference height, z_{ref}.

Overwater stations were adjusted to 10 meter neutral conditions using bulk formulae outlined in Large and Pond (1981) and Fairall et al (1996, 2003). Following Chiles & Delfiner (1999), a universal kriging scheme was chosen to allow for the presence of drift in the mean. The scattered distribution of stations within the interpolation area resulted in a sheltering effect in which stations screened from an interpolation point by stations in front of them were assigned a negative kriging weight. These negative weights associated with sheltering effects were corrected following the procedure outlined in Duetsch et al (1996). The procedure nudges negative weights to zero and then restandardizes the remaining kriging weights to sum to one.

When cross-validated with observations, kriging estimates tended to underestimate observed values resulting in a conditional bias. This is due to the well-known smoothing effect of kriging in which the reduction of variance can result in the underprediction of observations (Olea & Pawlowsky 1996, Isaaks & Srivastava 1989). To

correct for the smoothing effect of kriging, we followed Olea & Pawlowsky (1996) in which a compensated kriging technique was used to adjust kriging estimates based on their conditional bias:

$$Z^*(x) = Z(x) - \frac{\sigma^2(x)}{\sigma^2_{max}(x)}\left(Z(x) - \frac{Z(x)-b}{a}\right) \qquad \text{(A2)}$$

where Z*(x) is the corrected kriging estimate at location x, Z(x) is the original kriging estimate, σ^2 is the kriging variance, σ^2_{max} is the maximum kriging variance, and a and b are the slope and intercept, respectively, of a linear regression curve which describes the conditional bias present at a station. The linear regression coefficients, a and b, were linearly interpolated over the interpolation grid to estimate the smoothing effect at interpolation grid points which did not have observations.

The kriging scheme was applied to u (East-West) and v (North-South) components of the surface wind field independently for each 30 minute time step. Using a fixed range (a) of 24km and a 30% nugget effect, a modeled variogram of the form:

$$\gamma(h) = B\left(1 - 0.7e^{-\frac{h}{24}}\right) \qquad \text{(A3)}$$

was fit to data by using a variable sill height (B) calculated from data at a separation distance (h) between 90-200km. In Figure A.1, the mean and interquartile range of experimental variograms (calculated using a 5km bin size) normalized by their sill height,

are shown with the exponential variogram model. The model agrees reasonably well with the mean experimental variogram for both u and v components.

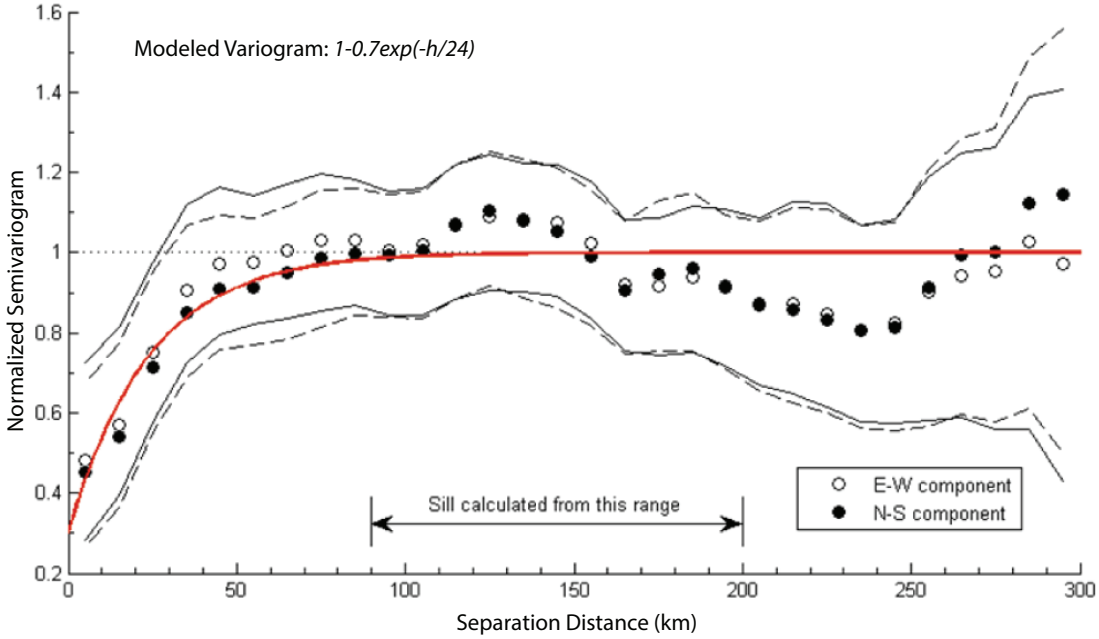

Figure A.1 Normalized semivariogram for u (E-W) and v (N-S) component of surface wind field. Red line represents the modeled variogram, markers represent bin-averaged experimental variograms, and black lines (dashed/solid) represent the interquartile range of experimental variograms (u/v).

BIBLIOGRAPHY

Agrawal, Y.C., E.A. Terray, M.A. Donelan, P.A. Hwang, A.J. Williams III, W.M. Drennan, K.K. Kahma, and S.A. Kitaigorodskii (1992): Enhanced dissipation of kinetic energy beneath surface waves, *Nature*, 359, 219-220.

Anctil, F., and M.A. Donelan (1996): Air-water momentum flux observations over shoaling waves, *J. Phys. Oceanogr.*, 26, 1344– 1353.

Andreas, E. L. (2009): Relating the drag coefficient and the roughness length over the sea to the wavelength of the peak waves, *J. Phys. Oceanogr.*, 39, 3011-3020.

Anis, A., and J. N. Moum (1992): The superadiabatic surface-layer of the ocean during convection, *J. Phys. Oceanogr.*, 22, 1221– 1227.

Anis, A., and J. N. Moum (1995): Surface wave-turbulence interactions-Scaling epsilon(z) near the sea-surface, *J. Phys. Oceanogr.*, 25, 2025-2045.

Ardhuin, F., B. Chapron, and T. Elfouhaily (2004): Waves and the air-sea Momentum Budget: Implications for Ocean Circulation Modeling, *J. Phys. Oceanogr.,* 34, 1741-1755.

Ardhuin, F., T. H. C. Herbers, K. P. Watts, G. P. van Vledder, R. Jensen, and H. C. Graber (2007): Swell and Slanting-Fetch Effects on Wind Wave Growth, *J. Phys. Oceanogr.*,37:4, 908-931.

Atatürk, S, and B. Katsaros (1999): Wind stress and surface waves observed on Lake Washington. *J. Phys. Oceanogr.*, 29, 633–650.

Babanin, A. V., and Y. P. Soloviev (1998): Field investigation of transformation of the wind wave frequency spectrum with fetch and the stage of development. *J. Phys. Oceanogr.*, 28, 563–576.

Badulin, S. I., A. V. Babanin, V. E. Zakharov, and D. Resio (2007): Weakly turbulent laws of wind-wave growth. *J. Fluid Mech*., 591, 339–378.

Baldocchi, DD, B.B. Hicks, and T.P.P. Meyers (1988): Measuring biosphere–atmosphere exchanges of biologically related gases with micro- meteorological methods. *Ecology*, 69, 1331–1340.

Banner, M.L., (1990): Equilibrium Spectra of Wind Waves, *J. Phys. Oceanogr.,* 20, 966-984.

Banner, M.L., A.V. Babanin, and I.R. Young (2000): Breaking Probability for Dominant Waves on the Sea Surface*, J. Phys. Oceanogr*., 30, 3145-3160.

Banner, M.L., and W.L. Peirson (1998): Tangential stress beneath wind-driven air-water interfaces. *J. Fluid Mech.,* 364, 115–145.

Booij, N., Holthuijsen, L.H. and Ris, R.C., 1996: The" SWAN" wave model for shallow water. *Coastal Engineering Proceedings*, *1*(25).

Boon, J.D. (1998): Wave climate and wave monitoring in lower Chesapeake Bay. Proc. Third Int. Conf. on Ocean Wave Measurement and Analysis. Virginia Beach, VA, ASCE, 1076–1087.

Burchard H., O. Petersen, and T. P. Rippeth (1998): Comparing the performance of the Mellor–Yamada and the k–« two-equation turbulence models. *J. Geophys. Res*., 103, 10 543-10 554.

Burchard, H. (2001): Simulating the wave-enhanced layer under breaking surface waves

with two-equation turbulence models*, J. Phys. Oceanogr*.,31, 3133-3145.

Burchard, H., and K. Bolding (2001): Comparative analysis of four second-moment turbulence closure models for the oceanic mixed layer. *J. Phys. Oceanogr*., 31, 1943–1968.

Burchard, H., R.D. Hetland, E. Schulz, and H.M. Schuttelaars (2011). Drivers of residual estuarine circulation in tidally energetic estuaries: straight and irrotational channels with parabolic cross section. *J. Phys. Oceanogr.* 41:548-570

Canuto, V. M., A. Howard, Y. Cheng, and M. S. Dubovikov (2001): Ocean turbulence. Part I:One point closuremodel—Momentum and heat vertical diffusivities. *J. Phys. Oceanogr*., 31, 1413–1426.

Cassiani, M., G.G. Katul, and J.D. Albertson (2008): The effects of canopy leaf area index on airflow across forest edges: Large-eddy simulation and analytical results, *Boundary Layer Meteorol*., 126, 433–460, doi:10.1007/s10546-007-9242-1.

Charnock, H. (1955): Wind stress on a water surface. *Quart. J. Roy. Meteor. Soc*., 81, 639–640.

Chen, S.N. and L.P. Sanford (2008): Lateral circulation driven by boundary mixing and the associated transport of sediments in idealized partially mixed estuaries. *Cont. Shelf. Res.* 29:101-118

Chen, S.N. and L.P. Sanford (2009): Axial wind effects on stratification and longitudinal salt transport in an idealized, partially mixed estuary. *J. Phys. Oceanogr.* 39:1905-1920

Chen, S.N., L.P. Sanford, and D.K. Ralston (2009): Lateral circulation and sediment transport driven by axial winds in an idealized partially, mixed estuary. *J. Geophys. Res.* 114:C12006

Chiles, J.P., and P. Delfiner (1999): Geostatistics: modeling spatial uncertainty, John Wiley Intersciences, 695 pp.

Chuang, W.S. and W.C. Boicourt (1989): Resonant seiche motion in the Chesapeake Bay. *J. Geophys. Res.* 94:C2 2105-2110

Churchill, J.H., A.J. Plueddemann, and S.M. Faluotico (2006): Extracting wind sea and swell from directional wave spectra derived from a bottom-mounted ADCP. *Tech Rep* 2006-13, 34pp, Woods Hole Oceanogr. Inst., Woods Hole, MA.

Craig, P. D. (1996): Velocity profiles and surface roughness under breaking waves, *J. Geophys. Res.*, 101, 1265-1277.

Craig, P. D., and M. L. Banner (1994): Modeling wave-enhanced turbulence in the ocean surface-layer*, J. Phys. Oceanogr*., 24, 2546-2559.

Craik, A. D. D., and S. Leibovich (1976): A rational model for Langmuir circulations*. J. Fluid Mech.*, 73, 401-426.

Craik, A.D., 1977: The generation of Langmuir circulations by an instability mechanism. *J. Fluid Mech*, *81*(2), pp.209-223.

Craik, P.D., and S. Leibovich S. (1976). A rational model for Langmuir circulations. *J. Fluid Mech.* 73:401-426

Csanady, G.T. (1973).: Wind-induced barotropic motions in long lakes. *J. Phys Oceanogr.* 39:2324-2337

D'Asaro, E. A. (2001): Turbulent vertical kinetic energy in the ocean mixed layer. *J.*

Phys. Oceanogr., 31, 3530–3537.

Deutsch, C. (1996): Correcting for Negative Weights in Ordinary Kriging, *Computers & Geosci*, 22, 7, 765-773

Dillon, T. M. (1982): Vertical overturns: A comparison of Thorpe and Ozmidov length scales. *J. Geophys. Res*., 87 (C12), 9601–9613.

Dobson, F.W., S.D. Smith SD, and R.J. Anderson (1994): Measuring the relationship between wind stress and sea state in the open ocean in the presence of swell. *Atmos.–Ocean*, 32, 237–256.

Donelan, M. A., (1990): Air–sea interaction. The Sea, B. LeMehaute and D. M. Hanes, Eds., *Ocean Engineering Science*, Vol. 9, Wiley and Sons, 239–292.

Donelan, M., J. Hamilton, and W. H. Hui (1985): Directional spectra of wind-generated waves, *Philos. Trans. Roy. Soc. London*, A315, 509–562.

Donelan, M.A. , and W. J. Pierson Jr. (1987): Radar scattering and equilibrium ranges in wind-generated waves with application to scatterometry. *J. Geophys. Res*., 92, 4971-5029.

Donelan, M.A., (1982): The dependence of the aerodynamic drag coefficient on wave parameters, Preprint, Conf. on Meteorology and Air-Sea Interaction of the Coastal Zone*, Le Hague Amer. Meteorological Soc*, 381-187.

Drennan, W, and H. Graber (2003): On the wave age dependence of wind stress over pure winds seas. *J. Geophys. Res*., 108, FET 10 -1-13.

Drennan, W. M., H. C. Graber, D. Hauser, and C. Quentin (2003): On the wave age dependence of wind stress over pure wind seas, *J. Geophys. Res*., 108, 8062

Drennan, W. M., H. C. Graber, D. Hauser, and C. Quentin (2003): On the wave age dependence of wind stress over pure wind seas, *J. Geophys. Res*., 108, 8062

Drennan, W. M., Kahma, K. K., & Donelan, M. A. (1999): On momentum flux and velocity spectra over waves. *Bound.-Layer Meteor.*, *92*(3), 489-515.

Drennan, W. M., M. A. Donelan, E. A. Terray, and K. B. Katsaros (1996): Oceanic turbulence dissipation measurements in SWADE, *J. Phys. Oceanogr*., 26, 808-815.

Drennan, W.M., K. K. Kahma, E. A. Terray, M. A. Donelan, and S.A. Kitaigorodskii, (1992): Observations of the enhancement of kinetic energy dissipation beneath breaking wind waves, *Breaking waves*, 95-101.

Drennan, W.M., M.A. Donelan, E.A. Terray, and K.B. Katsaros (1996): Oceanic turbulence dissipation measurements in SWADE, *J. Phys. Oceanogr.,* 26, 808-815.

Edson, J.B., V. Jampana, R.A. Weller, S.P. Bigorre, A.J. Plueddemann, C.W. Fairall, S. Miller, L. Mahrt, D. Vickers, and H. Hersbach (2013): On the Exchange of Momentum over the Open Ocean. *J. Phys. Oceanogr.*, 43, 1589–1610.

Erickson, D.J. (1993): A stability dependent theory for air–sea exchange. *J. Geophys. Res*., 98, 8417–8488

Fairall, C. W., E. F. Bradley, J. E. Hare, A. A. Grachev, and J. B. Edson (2003): Bulk Parameterization of Air–Sea Fluxes: Updates and Verification for the COARE Algorithm. *J. Climate*, 16:4, 571-591

Fairall, C.W., E.F. Bradley, D.P. Rogers, J.B. Edson, G.S. Young (1996): Bulk parameterization of air–sea fluxes for TOGA COARE. *J. Geophys. Res*., 101, 3747–3764.

Feddersen, F., J. H. Trowbridge, and A. J. Williams (2007): Vertical structure of

dissipation in the nearshore, *J. Phys. Oceanogr*., 37, 1764-1777.

Fisher, A.W., L.P. Sanford, and S.E. Suttles (2015): Wind Stress Dynamics in Chesapeake Bay: Spatiotemporal Variability and Wave Dependence in a Fetch-Limited Environment. *J. Phys. Oceanogr.*, **45**, 2679–2696.

Fisher, A.W., L.P. Sanford, M.E. Scully, and S.E. Suttles (*in review*): Surface Wave Effects on the Translation of Wind Stress Across the Air-Sea Interface in a Fetch-limited, Coastal Embayment. *J. Phys Oceanogr*.

Fleagle, R.G., J.A. Businger (1980): An Introduction to Atmospheric Physics, Academic Press, 432pp.

Friedrichs, C.T. and J.D. Hamrick (1996): Effects of channel geometry on cross sectional variations in along channel velocity in partially stratified estuaries. In Buoyancy Effects on Coastal and Estaurine Dynamics, Coastal Estuarine Stud. Ser., vol 53, edited by Aubrey & Friedrichs

Galperin, B., L. H. Kantha, S. Hassid, and A. Rosati (1988): A quasiequilibrium turbulent energy model for geophysical flows. *J. Atmos. Sci*., 45, 55–62.

Gargett, A. E., and J. R. Wells (2007): Langmuir turbulence in shallow water. Part 1. Observations, *J. Fluid Mech*. 576:27–61.

Gargett, A. E., T. R. Osborn, and P. W. Nasmyth (1984): Local Isotropy and the decay of turbulence in a stratified fluid. *J. Fluid Mech*., 144, 231-280.

Gargett, A.E., J. Wells, A.E. Tejada-Martinez, C.E. Grosch (2004): Langmuir supercells: a mechanism for sediment resuspension and transport in shallow seas. *Science* 306:1925-1928

Garratt, J.R. (1977): Review of drag coefficients over oceans and continents. *Month. Weath. Rev.* 105, 915-929

Garratt, J.R. (1992): The Atmospheric Boundary Layer, 316 pp., Cambridge Univ. Press, New York

Geernaert ,G.L., K.B. Katsaros, and K. Richter (1986): Variations of the drag coefficient and its dependence on sea state, *J. Geophys. Res*., 91, 7667–7679.

Geernaert, G., S. Larsen, and F. Hansen (1987): Measurements of the wind stress, heat flux, and turbulence intensity during storm conditions over the North Sea, *J. Geophys. Res.*, 92(C12), 13127-13139.

Geernaert, G.L. (1990): Bulk parameterization for the wind stress and heat fluxes, in Surface Waves and Fluxes, edited by G. L. Geernaert and W. J. Plant, pp. 91–172, Kluwer Acad., Norwell, Mass.

Gemmrich, J. (2010): Strong turbulence in the wave crest region. *J. Phys Oceanogr.*, 40, 583-595.

Gemmrich, J. R., and D. M. Farmer (2004): Near-surface turbulence in the presence of breaking waves, *J. Phys. Oceanogr*., 34, 1067-1086.

Gemmrich, J. R., M. L. Banner, and C. Garrett (2008): Spectrally resolved energy dissipation rate and momentum flux of breaking waves, *J. Phys. Oceanogr*., 38, 1296–1312.

Gemmrich, J.R, and D. Farmer (1999): Observations of the scale and occurrence of breaking surface waves, *J. Phys. Oceanogr*., 29, 2595–2606.

Gerbi, G. P., J. H. Trowbridge ,E. A. Terray, A. J. Plueddemann, and T. Kukulka, (2009): Observations of turbulence in the ocean surface boundary layer: Energetics and

transport. *J. Phys. Oceanogr*., 39, 1077-1096.

Gerbi, G.P., J.H. Trowbridge, J.B. Edson, A.J. Pleuddemann, E.A. Terray, and J.J. Fredericks (2008): Measurements of Momentum and Heat Transfer across the Air-Sea Interface. *J. Phys Oceanogr.,* 38, 1054-1072.

Geyer, W.R. (1997): Influence of wind on dynamics and flushing of shallow estuaries. *Estuarine, Coastal, and Shelf Science* 44:713-722

Grant, A. L., and S. E. Belcher (2009): Characteristics of Langmuir turbulence in the ocean mixed layer. *J. Phys. Oceanogr*., 39,1871–1887.

Greenan, B. J. W., N. S. Oakey, and F. W. Dobson (2001): Estimates of dissipation in the ocean mixed layer using a quasihorizontal microstructure profiler. *J. Phys. Oceanogr*., 31, 992-1004.

Hagy, J. D., W. R. Boynton, C. W. Keefe, and K. V. Wood (2004): Hypoxia in Chesapeake Bay, 1950–2001: long-term change in relation to nutrient loading and river flow. *Estuaries,* 27, 634–658.

Hansen, D.V. and M. Rattray (1965): Gravitational Circulation in straits and estuaries. *J. Mar. Res.* 23:104-22

Harcourt, R. R. (2013): A second-moment closure model of Langmuir turbulence. *J. Phys. Oceanogr*., 43, 673–697.

Harcourt, R. R., and E. A. D'Asaro (2008): Large-eddy simulation of Langmuir turbulence in pure wind seas. *J. Phys. Oceanogr*.,38, 1542–1562.

Harcourt, R.R. (2015): An improved second-moment closure model of Langmuir turbulence. J. Phys. Oceanogr., 45, 84-103.

Hasselmann, K, T.P. Barnett, E. Bouws, H. Carlson, D.E. Cartwright, K Enke, J.A. Ewing, H. Gienapp, D.E. Hasselmann, P. Kruseman, A. Meerburg, P. Muller, D.J. Olbers, K. Richter, W. Sell W, and H. Walden (1973): Measurement of wind–wave growth and swell decay during the Joint North Sea Wave Project (JONSWAP). *Dtsch. Hydrogr. Z.,* 12 (Suppl.), A8.

Hasselmann, K. (1971): On the mass and momentum transfer between short-gravity waves and larger-scale motions. *J. Fluid Mech.,* 4, 189-205.

Hinze, J. O. (1975): Turbulence. 2nd ed. Mc-Graw Hill, 790 pp.

Holt, S. E., J. R. Koseff, and J. H. Ferziger, (1992): The evolution of turbulence in the presence of mean shear and stable stratification. *J. Fluid Mech*., 237, 499–539.

Huijts, K.M.H., H.M. Schuttelaars, H.E. de Swart, and C.T. Friedrichs (2009): Analytical study of the transverse distributions of along-channel and transverse residual flows in tidal estuaries. *Cont. Shelf Res.* 29:89-100

Hwang, P.A. (2010): Comments on Relating the drag coefficient and the roughness length over the sea to the wavelength of the peak waves, *J. Phys. Oceanogr.,* 40, 2556-2562

Isaaks, E.H., and R.M. Srivastava (1989): An Introduction to applied geostatistics, Oxford Univ. Press, New York, 561pp.

Itsweire, E. C., J. R. Koseff, D. A. Briggs, and J. H. Ferziger (1993): Turbulence in a stratified shear flows: Implications for interpreting shear-induced mixing in the ocean. *J. Phys.. Oceanogr*., 23, 1508–1522.

Ivey, G. N., and J. Imberger (1991): On the nature of turbulence in a stratified fluid. Part I: The energetics of mixing. *J. Phys. Oceanogr*., 21, 650–658.

Janssen, P. A. E. M. (1989): Wave-induced stress and the drag of air flow over sea waves. *J. Phys. Oceanogr.*, 19, 745–754.

Johnson, D. (2002): DIWASP, a directional wave spectra toolbox for MATLAB: User manual. Centre for Water Research, University of Western Australia, Research Rep. WP-1601-DJ (V1.1), 19 pp.

Johnson, H.K., and H.J. Vested (1992): Effects of water waves on wind shear stress for current modeling. *J. Atmos. Oceanic Technol*., 9, 850–861.

Johnson, H.K., J. Højstrup, H.J. Vested, and S.E. Larsen (1998): On the dependence of sea surface roughness on wind waves, *J. Phys. Oceanogr*., 28, 1702– 1716.

Jones, N. L., and S. Monismith (2008a): The influence of whitecapping waves on the vertical structure of turbulence in a shallow estuarine embayment, *J. Phys. Oceanogr.,* 38, 1563-1580.

Jones, N. L., and S. Monismith (2008b): Modeling the influence of wave enhanced turbulence in a shallow tide- and wind-driven water column, *J. Geophys. Res*., 113, C03009, 1-13.

Jones, N.L., and S. G. Monismith (2007): Measuring short-period wind waves in a tidally forced environment with a subsurface pressure gauge, *Limnol. Oceanogr. Methods*, 5, 317–327.

Kaimal, J. C., J. C. Wyngaard, Y. Izumi, and O. R. Cote, (1972): Spectral characteristics of surface-layer turbulence. *Quart. J. Roy. Meteor. Soc.,* 98, 563–589.

Kaimal, J.C., and J.A. Businger (1963): A continuous wave sonic anemometer-thermometer, *J. Appl. Meteor*.,2, 156-164.

Kaimal, J.C., and J.E. Gaynor (1991): Atmospheric Boundary Layer Flows, Their Structure and Measurement, Oxford University Press, New York, 289 pp.

Kantha, L. H., and C. A. Clayson (1994): An improved mixed layer model for geophysical applications. *J. Geophys. Res*., 99, 25 235–25 266.

Kemp, W.M., W.R. Boynton, J.E. Adolf, D.F. Boesch, W.C. Boicourt, G. Brush, J.C. Cornwell, T.R. Fisher, P.M. Glibert, J.D. Hagy, L.W. Harding, E.D. Houde, D.G. Kimmel, W.D. Miller, R.I.E. Newell, M.R. Roman, E.M. Smith, and J.C. Stevenson (2005): Eutrophication in Chesapeake Bay: historical trends and ecological interactions. *Mar. Eco. Prog. Ser.* 303:1-29

Kenyon, K. E. (1969): Stokes drift for random gravity waves. *J. Geophys. Res*., 74, 6991–6994.

Kim, S-C, C.T. Friedrichs, JP-Y Maa, and L.D. Wright (2000): Estimating bottom stress in tidal boundary layer from acoustic Doppler velocimeter data, *J Hydraul. Eng*., 126, 399-406.

Kitaigorodskii, S.A., (1983):On the theory of the equilibrium range in the spectrum of wind-generated gravity waves. J. Phys. Oceanogr.,13, 816-827.

Kitaigorodskii, SA, (1973): The Physics of Air–Sea Interaction. Cambridge University Press, 273 pp.

Komen, G. J., S. Hasselmann, and K. Hasselmann (1984): On the Existence of a Fully Developed Wind-Sea Spectrum, *J. Phys. Oceanogr.,* 14, 1271-1285.

Komen, G., L. Cavaleri, M. Donelan, K. Hasselman, and P.A.E.M. Janssen (1994): Dynamics and Modelling of Ocean Waves, Cambridge Univ. Press, 532 pp.

Komen, G.J., P.A.E.M. Janssen, V. Makin, and W. Oost (1998): On the sea state dependence of the Charnock parameter, *Global Atmos. Ocean Syst.,* **5,** 367-388.

Kraus, E.B. and J.A. Businger (1994): Atmosphere-Ocean Interaction. Oxford University Press, 362 pp.

Kukulka, T., A. J. Plueddemann, and P. P. Sullivan (2012), Nonlocal transport due to Langmuir circulation in a coastal ocean, *J. Geophys. Res.* 117:C12007

Kukulka, T., A. J. Plueddemann, J.H. Trowbridge, and P.P. Sullivan (2011): The influence of crosswind tidal currents on Langmuir circulation in a shallow ocean. *J. Geophys. Res.,* 116, C08005.

Kukulka, T., A.J. Plueddemann, J.H. Trowbridge, and P.P. Sullivan (2009): Significance of Langmuir circulation in upper ocean mixing: comparison of observations and simulations. *Geophys. Res. Lett.* 117:C12007

Kukulka, T., A.J. Plueddemann, J.H. Trowbridge, and P.P. Sullivan (2010): Rapid mixed layer deepening by the combination of Langmuir and shear instabilities: a case study. *J. Phys. Oceanogr.* 40:2381-2399

Kundu, P. K. (1980): A numerical investigation of mixed-layer dynamics, *J. Phys. Oceanogr*., 10, 220-236.

Langmuir, I. (1938): Surface motion of water induced by wind. *Science* 87:119-123

Large, W.G., and S. Pond (1981): Open ocean momentum flux measurements in moderate to strong winds. *J. Phys. Oceanogr*., 11, 324–336.

Leibovich, S. (1977): Convective instability of stably stratified water in the ocean. *J. Fluid Mech* ., 82, 561 -585.

Leibovich, S. (1983): The form and dynamics of Langmuir circulations. *Annu. Rev. Fluid*

Mech., 15, 391–427.

Lerczak J.A. and W.R. Geyer (2004): Modeling the lateral circulation in straight, stratified estuaries. *J Phys Oceanogr.* 34:1410-1428

Li, M. and C. Garrett, (1997): Mixed Layer Deepening Due to Langmuir Circulation. *J. Phys. Oceanogr.,* 27, 121-132.

Li, M., C. Garrett, and E. Skyllingstad, (2005): A regime diagram for classifying turbulent large ddies in the upper ocean. *Deep-Sea Res.,* 52, 259-278.

Li, M., L. Zhong, W.C. Boicourt (2005): Simulations of Chesapeake Bay estuary: sensitivity to turbulence mixing parameterizations and comparison with observations. *J. Geophys Res.* 110:C12004

Li, S., M. Li, G. Gerbi., and J-B Song (2013): Roles of Breaking waves and Langmuir circulation in the surface boundary layer of a coastal ocean, *J. Geophys. Res: Oceans*, 118, 5173-5187.

Li, Y. and M. Li (2011a). Effects of winds on stratification and circulation in a partially mixed estuary. *J. Geophys. Res.* 116:C12012

Li, Y. and M. Li (2012): Wind-driven lateral circulation in a stratified estuary and its effects on the along-channel flow. *J. Geophys. Res.*, *117*(C9).

Li, Y. and M. Li. (2011b). Wind-driven lateral circulation in a stratified estuary and its effects on the along-channel flow. *J. Geophys. Res.* 117:C09005

Lin, W. (2000): Modeling surface wind waves and their effects on air–sea fluxes in Chesapeake Bay. *Ph.D. dissertation*, University of Maryland Center for Environmental Science, Cambridge, MD, 226 pp.

Lin, W., L.P. Sanford, and S.E. Suttles (2002): Wave measurement and modeling in Chesapeake Bay. *Cont. Shelf. Res*., 22, 2673-2686.

Lin, W., L.P. Sanford, B.J. Alleva, and D.J. Schwab (1998): Surface wind wave modeling in Chesapeake Bay. Proc. Third Int. Conf.on Ocean Wave Measurement and Analysis. Virginia Beach, VA, ASCE, 1048–1062.

Lin, W., L.P. Sanford, S.E. Suttles, and R. Valigura (2002): Drag coefficients with fetch-limited wind waves. *J. Phys. Oceanogr*., 32, 3058-3074.

Liu W.T., K.B. Katsaros, and J.A. Businger (1979): Bulk parameterization of air–sea exchanges of heat and water vapor including the molecular constraints at the interface. *J. Atmos. Sci*., 36, 1722–1735.

Longuet-Higgins M.S., R.W. Stewart (1964): Radiation stresses in water waves; a physical discussion, with applications, *Deep-Sea Res.*,11, 529-562.

Longuet-Higgins, M.S. (1970): Longshore currents generated by obliquely incident sea waves: 1. *J. Geophys. Res.*, 75(33), 6778-6789.

Longuet-Higgins, M.S. and R.W. Stewart (1960): Changes in the form of short gravity waves on long waves and tidal currents, *J. Fluid Mech.*, 8, 565-583.

Luketina, D. A., and J. Imberger (1989): Turbulence and entrainment in a buoyant surface plume. *J. Geophys. Res*., 94 (C9), 12 619-12 636.

Lumley, J. L., and E. A. Terray (1983): Kinematics of turbulence convected by a random wave field, *J. Phys. Oceanogr*., 13, 2000-2007.

MacCready, P., and W.R. Geyer (2014): The Estuarine Circulation. *Ann. Rev. Fluid Mech.* 46:175-197

Magnaudet, J., and L. Thais (1995): Orbital rotational motion and turbulence below

laboratory wind water waves. *J. Geophys. Res*., 100, 757-771.

Mahrt, L., D. Vickers, J. Howell, J. Højstrup, J.M. Wilczak, J.B. Edson, J.E. Hare (1996): Sea surface drag coefficients in RASEX. *J. Geophys. Res*., 101, 14 327–14 335.

Makin, V.K., and C. Mastenbroek (1996): Impact of waves on air-sea exchange of sensible heat and momentum, *Bound-Layer Meteor*., 79, 279– 300.

Markfort, C.D., A.L.S. Perez, J.W. Thill, D.A. Jaster, F. Porte-Agel, H.G. Stefan (2010): Wind sheltering of a lake by a tree canopy or bluff topography. *Water Resources Res.* 46, W03530

Martin, M.J. (1998): An investigation of momentum exchange parameterizations and atmospheric forcing for the coastal mixing and optics program. *M.S. thesis*, Massachusetts Institute of Technology, Boston, MA, and the Woods Hole Oceanographic Institution, Woods Hole, MA, 83 pp.

Mastenbroek, C.V., V.K. Makin, M.H. Garrat, J.P. Giovanangeli (1996): Experimental evidence of the rapid distortion of the turbulence in the air flow over water waves. *J. Fluid Mech*., 318, 273–302.

McMillan, R.T. (1987): An eddy correlation technique with extended application to non-simple terrain. *Bound.-Layer Meteor*., 43, 231–245.

McWilliams, J. C., P. P. Sullivan, and C.-H. Moeng (1997): Langmuir turbulence in the ocean. *J. Fluid Mech*., 334, 1–30.

McWilliams, J.C., E. Huckle, J. H. Liang, and P. P. Sullivan (2012): The wavy Ekman layer: Langmuir circulations, breaking waves, and Reynolds stress. *J. Phys Oceanogr.,* 42, 1793-1816.

Mellor, G. L., and T. Yamada (1982): Development of a turbulence closure model for

geophysical fluid problems, *Rev. Geophys*., 20, 851-875.

Melsom, A., and Ø. Sætra (2004): Effects of wave breaking in the near-surface profiles of velocity and turbulent kinetic energy. *J. Phys. Oceanogr*., 34, 490–504.

Melville, W. K. (1996): The role of surface-wave breaking in air-sea interaction. *Annu. Rev. Fluid Mech.*, 28, 279–321.

Melville, W. K., F. Veron, and C. White, (2002): The velocity field under breaking waves: Coherent structures and turbulence. *J. Fluid Mech*., 454, 203–233.

Miles, J.W. (1957): On the generation of surface waves by shear flows, *J. Fluid Mech.*, *3*(02), pp.185-204.

Mitsuyasu, H. (1985): A note on the momentum transfer from wind to waves. *J. Phys. Oceanogr.*, 33, 1978-1989.

Monin, A.S., and A.M. Obukhov (1954): Basic laws of turbulent mixing in the surface layer of the atmosphere. *Tr. Geofiz. Inst., Akad. Nauk SSSR*, 151, 163–187.

Monismith, S. G., and D.A. Fong, (2004): A note on the potential transport of scalars and organisms by surface waves, *Limnol. Oceanogr.*,*49*(4), 1214-1217.

Monismith, S. G., and J. Magnaudet (1998): On wavy mean flows, Langmuir cells, strain, and turbulence. Physical Processes in Lakes and Oceans, J. Imberger, Ed., Coastal and Estuarine Studies Series, Vol. 54, Amer. Geophys. Union, 101–110.

Monismith, S.G. (1986): An experimental study of the upwelling response of stratified reservoirs to a surface shear stress. *J. Fluid Mech.* 171:407-439

Mortensen, N.G. (1994): Flow-response characteristic of the Kaijo Denki omni-direction sonic anemometer (TR-61V), Riso-R-704 (EN), Riso National Laboratory, Roskilde, Denmark.

Murphy, R.R., W.M. Kemp, and W.P. Ball (2011): Long-term trends in Chesapeake Bay seasonal hypoxia, stratification, and nutrient loading. *Estuaries & Coasts* 34:1293-1309

Noh, Y., H. S. Min, and S. Raasch (2004): Large eddy simulation of the ocean mixed layer: The effects of wave breaking and Langmuir circulation, *J. Phys. Oceanogr.*, 34, 720–735.

Nunes, R., and J. Simpson (1985): Axial convergence in a well-mixed estuary. *Estuary & Coast Shelf Sci.* 20:637-649

Obukhov, A.M. (1971): Turbulence in an atmosphere with a nonuniform temperature. *Bound.-Layer Meteor.*, 2, 7–29.

Olea, R., and V. Pawlowksy (1996): Compensating for estimation smoothing in kriging, *Math. Geo*, 28, 4, 407-417

Oost, W.A. (1998): The KNMI HEXMAX stress data: a reanalysis, *Bound.-Layer Meteor.*, 86, 447–468.

Oost, W.A., G.J. Komen, C.M.J. Jacobs, and C. van Oort (2002): New evidence for a relation between wind stress and wave age from measurements during ASGAMAGE. *Bound.-Layer Meteor.*, 103, 409–438.

Osborn, T., D. M. Farmer, S. Vagle, S. A. Thorpe, and M. Cure (1992): Measurements of bubble plumes and turbulence from a submarine, *Atmos. Ocean*, 30, 419-440.

Panofsky, H.A., and J.A. Dutton (1984): Atmospheric Turbulence: Models and Methods for Engineering Applications. John Wiley Intersciences, 397 pp.

Perrie, W, and B. Toulany (1990): Fetch relations for wind-generated waves as a function of wind-stress scaling. *J. Phys. Oceanogr.*, 20, 1666-1681.

Phillips, O.M. (1977): The Dynamics of the Upper Ocean, 2nd ed., 336 pp., Cambridge Univ. Press, New York.

Phillips, O.M. (1985): Spectral and statistical properties of the equilibrium range in wind-generated gravity waves, *J. Fluid Mech*., 156, 495–531.

Plueddemann, A. J., and R. A. Weller (1999): Structure and evolution of the oceanic surface boundary layer during the Surface Waves Processes Program. *J. Mar. Syst*., 21, 85–102.

Polton, J. A., and S. E. Belcher (2007): Langmuir turbulence and deeply penetrating jets in an unstratified mixed layer, *J. Geophys. Res.,*112, C09020.

Pope, N.D., J. Widdows, and M.D. Brinsley (2006): Estimation of bed shear stress using the turbulent kinetic energy approach – A comparison of annular flume and field data, *Cont. Shelf Res*., 26, 959-970.

Potter, H., C.O. Collins, W.M. Drennan, and H.C. Graber (2015): Observations of wind stress direction during Typhoon Chaba (2010), *Geophys. Res. Letters*, *42*(22), 9898-9905.

Rabe, T.J., T. Kukulka, I. Ginnis, T. Hara, B.G. Reichl, E. A. D'Asaro, R.R. Harcourt, and P.P. Sullivan (2015): Langmuir Turbulence under Hurricane Gustav (2008), *J. Phys Oceanogr.,* 2015, 45, 657-677.

Rapp, R. J., and W. K. Melville (1990): Laboratory measurements of deep-water breaking waves, Philos. *Trans. R. Soc. London, Ser*, A331, 735-800.

Rieder, K. F., J. A. Smith, and R. A. Weller (1994): Observed directional characteristics of the wind, wind stress, and surface waves on the open ocean. *J. Geophys. Res.,* 99, 22 589–22 596.

Rodi, W. (1980): Turbulence Models and Their Application in Hydraulics. *Int. Assoc. Hydraul. Res. Delft*, 35 pp.

Rodi, W. (1987): Examples of calculation methods for flow and mixing in stratified fluids, *J. Geophys. Res*., 92, 5305-5328.

Sanay, R., and A. Valle-Levinson (2005): Wind-induced circulation in semi-enclosed homogeneous rotating basins. *J. Phys Oceanogr.* 35:2520-2531.

Sanford, L. P., and W. C. Boicourt (1990): Wind-forced salt intrusion into a tributary estuary. *J. Geophys. Res.*, *95*(C8), 13357-13371.

Sanford, L.P. (1994): Wave forced resuspension of upper Chesapeake muds. *Estuaries*, 17, 148–165.

Sanford, L.P., K.G. Sellner, and D.L. Breitburg (1990): Covariabiltiy of dissolved-oxygen with physical processes in the summertime Chesapeake Bay. *Estuaries & Coasts* 33: 1164-1175

Schotanus, P., F.T.M. Nieuwstadt, and H.A.R. de Bruin (1983): Temperature measurement with a sonic anemometer and its application to heat and moisture fluxes, *Bound-Layer Meteor*., 26, 81-93.

Schwendeman, M., J. Thomson, and J.R. Gemmrich (2015): Wave Breaking Dissipation in a Young Wind Sea, *J. Phys. Oceanogr.*, 44, 104-127.

Scully, M.E. (2010a): Wind modulation of dissolved oxygen in Chesapeake Bay. *Estuaries & Coasts.* 33:1164-1175

Scully, M.E. (2010b): The importance of climate variability to wind-driven modulatin of hypoxia in Chesapeake Bay. *J. Phys. Oceanogr.* 40:1435-1440

Scully, M.E. (2013): Physical controls on hypoxia in Chesapeake Bay: a numerical modeling study. *J. Geophys. Res.* 118:1239-1256.

Scully, M. E., A. W. Fisher, S. E. Suttles, L. P. Sanford, and W. C. Boicourt (2015): Characterization and modulation of Langmuir circulation in Chesapeake Bay. *J. Phys. Oceanogr*., 45, 2621-2639.

Scully, M.E., C.T. Friedrichs, and J. Brubaker (2005): Control of the estuarine stratification and mixing by wind-induced Straining of the estuarine density field. *Estuaries & Coasts.* 28:321-326

Scully, M.E., J.H. Trowbridge, and A.W. Fisher (2016): Observations of the Transfer of Energy and Momentum to the Oceanic Surface Layer Beneath Breaking Waves. *J. Phys. Oceanogr*., 48,1823-1837.

Scully, M.E., W.R. Geyer, and J.A. Lerczak (2009): The influence of lateral advection on the residual estuarine circulation: A numerical modeling study of the Hudson River estuary. *J Phys. Oceanogr.* 40:1473-1487

Scully, M.E., W.R. Geyer, and J.H. Trowbridge (2011): The Influence of Stratification and Nonlocal Turbulent Production on Estuarine Turbulence: An Assessment of Turbulence Closure with Field Observations, *J. Phys. Oceanogr*., 41, 166-185.

Shih, L. H., J. R. Koseff, G. N. Ivey, and J. H. Ferziger (2005): Parameterization of turbulent fluxes and scales using homogeneous sheared stably stratified turbulence simulations, J. Fluid Mech., 525, 193.

Skyllingstad, E. D., and D. W. Denbo (1995): An ocean large-eddy simulation of Langmuir circulations and convection in the surface mixed layer. J. Geophys. Res., 100, 8501–8522.

Smith, S.D., R.J. Anderson, W.A. Oost, C. Kraan, N. Maat, J. DeCosmo, K.B. Katasaros, K.L. Davidson, K. Bumke, L. Hasse, and H.M. Chadwick (1992): Sea surface wind stress and drag coefficients: The HEXOS results, *Bound-Layer Meteor*., 60, 109–142.

Smith, SD, (1988): Coefficients for sea surface wind stress, heat flux, and wind profiles as a function of wind speed and temperature. *J. Geophys. Res.* 93:C12 2156-2202

Soloviev, A., and R. Lukas (2003): Observation of wave-enhanced turbulence in the near-surface layer of the ocean during TOGA COARE, *Deep Sea Res*., Part I, 50, 371-395.

Stacey, M. T., S. G. Monismith, and J. R. Burau (1999): Observations of turbulence in a partially stratified estuary. *J. Phys. Oceanogr*., 29, 1950–1970.

Stips, A., H. Burchard, K. Bolding, H. Prandke, A. Simon, and A. Wuest (2005), Measurement and simulation of viscous dissipation in the wave affected surface layer, *Deep Sea Res*., Part II, 52, 1133-1155.

Sullivan, P. P., J. C. McWilliams, and W. K. Melville (2007): Surface gravity wave effects in the oceanic boundary layer: Large-eddy simulation with vortex force and stochastic breakers. *J. Fluid Mech.*, 593, 405-452..

Sullivan, P. P., L. Romero, J. C. McWilliams, and W. K. Melville (2012): Transient evolution of Langmuir turbulence in ocean boundary layers driven by hurricane winds and waves. *J. Phys. Oceanogr*., 42, 1959–1980.

Tennekes, H., and J. L. Lumley (1972): A First Course in Turbulence. The Massachusetts Institute of Technology, 300 pp.

Terray, E. A., M. A. Donelan, Y. C. Agrawal, W. M. Drennan, K. K. Kahma, A. J. Williams, P. A. Hwang, and S. A. Kitaigorodskii (1996): Estimates of kinetic energy

dissipation under breaking waves, *J. Phys. Oceanogr*., 26, 792-807.

Terray, E. A., W. M. Drennan, and M. A. Donelan (1999): The vertical structure of shear and dissipation in the ocean surface layer, paper presented at Symposium on the Wind-Driven Air-Sea Interface: Electromagnetic and Acoustic Sensing, Wave-Dynamics and Turbulent Fluxes, Univ. of N. S. W., Sydney, N. S. W., Australia.

Thomson, J., A. Jessup, and J. Gemmrich (2009): Energy dissipation and the spectral distribution of whitecaps, *Geophys. Res. Lett*., 36, L11601.

Thomson, J., E.A. D' Asaro, M.F. Cronin, W.E. Rogers, R.R. Harcourt, and A. Shcherbina (2013): Waves and the equilibrium range at Ocean Weather Station P, *J. Geophys. Res.* 118, 5951-5962.

Trayskovski, P., W.R. Geyer, and C. Sommerfield C. (2004): Rapid sediment deposition and fine-scale formation in the Hudson estuary. *J. Geophys. Res.* 109:F02004

Tseng, R.S., and E. D'Asaro (2004): Measurements of turbulent vertical kinetic energy in the ocean mixed layer from Lagrangian floats. *J. Phys. Oceanogr.* 34:1984-1990

Umlauf, L., and H. Burchard (2003): A generic length-scale equation for geophysical turbulence models, J. Mar. Res., 61, 235-265.

Umlauf, L., and H. Burchard (2005): Second-order turbulence closure models for geophysical boundary layers: A review of recent work, *Cont. Shelf Res*., 25, 795-827.

USEPA (U.S. Environmental Protection Agency) (2010): Chesapeake Bay Total Maximum Daily Load for Nitrogen, Phosphorus and Sediment. U.S. Environmental Protection Agency Chesapeake Bay Program Office, Annapolis, Maryland.

Valle-Levinson, A. (2008): Density-driven exchange flow in terms of Kelvin and Ekman numbers. *J. Geophys Res.* 113:C04001

Van Roekel, L. P., B. Fox-Kemper, P. P. Sullivan, P. E. Hamlington, and S. R. Haney (2012): The form and orientation of Langmuir cells for misaligned winds and waves, *J. Geophys. Res.*, 117, C05001.

Vickers, D., and L. Mahrt (1997): Fetch limited drag coefficients. *Bound.-Layer Meteor.*, 85, 53–79.

Wallace J.M., and P.V. Hobbs (1977): Atmospheric Science: An Introductory Survey, Academic Press, 350pp.

Wang, D.P. (1979): Wind-driven circulation in Chesapeake Bay, winter 1975, *J. Phys Oceanogr* 9:564-572

Warner, J. C., W. R. Geyer, and J. A. Lerczak (2005): Numerical modeling of an estuary: A comprehensive skill assessment. *J. Geophys. Res.*, 110, C05001

Warner, J.C., B. Armstrong, R. He, and J.B. Zambon (2010): Development of a coupled ocean–atmosphere–wave–sediment transport (COAWST) modeling system. *Ocean modelling*, *35*(3), pp.230-244.

Wilcox, D. C. (1988): Reassessment of the scale-determining equation for advanced turbulence models, *AIAA J.*, 26, 1299-1310.

Wilczak, J., S. Oncley, and S. Stage (2001): Sonic anemometer tilt correction algorithms. *Bound.-Layer Meteor.,* 99, 127-150.

Wu, J., (1980): Wind-stress coefficients over sea surface near neutral conditions—A Revisit. *J. Phys. Oceanogr.*, 10, 727–740.

Young, I. R., M. L. Banner, M. A. Donelan, A. V. Babanin, W. K. Melville, F. Veron, and C. McCormick (2005): An integrated system for the study of wind-wave source terms in finite-depth water, *J. Atmos. Oceanic Technol.*, 22, 814-831.

Zhou, Y., D. Scavia, and A.M. Michalak (2014): Nutrient Loading and meteorological conditions explain interannual variability of hypoxia in Chesapeake Bay. *Limnol. Oceanogr.*, 59(2), 373-384.